# Analysis of Quantum Semiconductor Heterostructures by Ballistic Electron Emission Spectroscopy

A THESIS
Presented to
The Academic Faculty
By
Daniel K. Guthrie

in Partial Fulfillment
of the Requirements for the Degree
Doctor of Philosophy in Electrical Engineering

Georgia Institute of Technology
December 1998

# Analysis of Quantum Semiconductor Heterostructures by Ballistic Electron Emission Spectroscopy

Approved:

Dr. Thomas K. Gaylord, Co-Chair

Dr. Elias N. Glytsis, Co-Chair

Dr. Phillip N. First, Co-Chair

Dr. Gary S. May

Dr. April S. Brown

Date Approved: Nov. 19, 1998

# Acknowledgments

Most things in life are accomplished with the help of other people. A thesis is no different. In the past five years I have relied on so many people on so many occasions that it would obviously be impossible to thank them all. In addition, I just completed the oral defense and the deadline for submission is only hours away. I apologize in advance to anyone who fails to penetrate the haze in which i am currently writing.

I would like to first thank my wife Christi. She has supported me one-hundred percent. Without her love and support, the completion of this thesis, and everyday life itself, would not be as full and complete. She is cool. I will always love her dearly.

Next I would like to thank all three of my advisors: Dr. Thomas 'the rock' Gaylord, Dr. Phillip 'the philter' First, and Dr. Elias 'super simulator' Glytsis. Their guidance and support has been unrelenting. Thank you for teaching me how to be a better researcher. Thank you for showing me how to be a better person.

I would also like to thank several other key people within the School of Electrical and Computer Engineering. Special thanx to me reading committee members Dr. April Brown and Dr. Gary May who i am sure did not suffer from insomnia after receiving my thesis for review. Thanx to Dr. Ed Conrad from the school of Physics and Dr. Kevin Brennan from ECE for their help. A special shout out to Diana Fouts, our graphics designer, whose friendship and help (not to mention the candy) has been very special to me. She is truly one of a kind. A big thank you goes to Harry 'Dan Guffry' Sullivan whose has always made me laugh. See ya at Freaknik Harry. I would like to thank Dr. James 'DSP' McClellan for being such a great teacher and for trying to show me how to think. In addition to the folks in the ECE department, several of the Microelectronics Research Center crowd have provided assistance, guidance, and friendship. These include Scott 'i need a smoke' Fowler, Bob 'do a different experiment' Rose, Gerry Hill, and Janna 'lookout' Chambers. Special Thanx to Dr. Ron Leibenguth for growing the all of the amazing $\mathrm{Ga}_{1-x}\mathrm{Al}_x\mathrm{As}$ samples in this thesis.

I also would like to thank of my friends that harrassed me endlessly about when am i going to graduate. December 12, 1998. Period. Seriously, I am very lucky to have so many good friends that I have know for so long. During my sentence here at Tech, I have gotten to know some really great people. Two people in particular with which I shared countless luches, laughs, rages, and conversations were Dave 'surfer' Brundrett, who was my office mate for many years, and Lee 'physics militia boy' Harrell, who was my lab mate. It was fun. I would like to thank David 'minivan' Walker for wooping my butt at racquet ball endlessly and for conversations in the hall. Thanx to 'Battlin' Bill 'he who knows all' Cullen for listening to me gripe and answering at least a million questions. Thanx to Ryan 'work day' McCormick for just simply putting up with my bad disposition and for being such a good friend. A special thanx goes to Greg 'boy genius' Henderson for being such a cool guy. Thanx James Moralez and Mike 'mountain' Howard for all of their help on various occasions. Thanx to Steve Schultz, Jon Bendickson, Carole Montarou and all of the other great people in our research group past and present. Thanx to Terry 'caver' Bigioni for all the great times. Thanx to Jacky Chen and Neena Iman for putting with me during the final crunch.

Thanx to Scott 'skippy' and Michelle 'munchkin' Munn, Kirk 'super freak' Duchow, and David 'just dave' Cannon for all of the great time we have spend together kayaking, rafting, and just screwing around. Along those lines, thanx to my long time buds Casey 'camaro' and Susan Brown, Richard 'Dick' and Becky Thomas, Josh 'ram rod' and Sylvia 'mississippi' Tennenbaum, Regan 'terminator' and Susan 'climber' Burmeister, Paul 'free-ball' and Kris McSwain, Chris 'wiz' and Trina Hamlin, and Denise and Peter Craymer. I apologize for any misspelled last names. Thanx to The hour is growing near. Thanx to

Jimmi Snyder for inventing Y2K compliant amphibionics and to Eric Lindbergh for helping me learn how to use them. Thanx to the river gods for keeping me safe in light of my frequent stupidity.

I would also like to thank Christi's parents Carol and Dale Barnwell, as well as my mothers husband Harvey Hudlow for the great times and for their support. A special thanx to my parents Jim Guthrie and Phyllis Hudlow and all of my relatives who have supported me for so many years. I finally did it.

Rock on...power to the people...billy jean...centerfold...put another dime in the juke box baby.

DANIEL K. GUTHRIE

*Georgia Institute of Technology*

*December 1998*

# Table of Contents

**Acknowledgments** iii

**Table of Contents** vi

**List of Tables** ix

**List of Figures** x

**Summary** xii

**Chapter 1 Introduction** 1

- 1.1 Research Objectives . . . 2
- 1.2 Background and Related Previous Work . . . 4
  - 1.2.1 Measurement Techniques . . . 4
  - 1.2.2 BEES Measurements of Single Interface Structures . . . 12
  - 1.2.3 BEES Measurements of Semiconductor Heterostructures . . . 14
- 1.3 Thesis Overview . . . 16

**Chapter 2 Extended Semiclassical BEES Model** 19

- 2.1 Background . . . 19
- 2.2 Inclusion of the Quantum Mechanical Transmittance for Non-Zone-Centered Band Minima . . . 23
- 2.3 Electron Momentum Distribution . . . 28
  - 2.3.1 Background . . . 28
  - 2.3.2 Inclusion of Elastic Scattering . . . 29

2.4 The Model . . . . . 30
2.5 Discussion . . . . . 32

**Chapter 3 Single-Interface Measurements** **34**
3.1 Background . . . . . 34
3.2 Experimental Apparatus and Sample Preparation . . . . . 36
3.3 Elastic Scattering . . . . . 37
3.4 Quantum Transmittance . . . . . 43
3.5 Model Stability and Range of Validity . . . . . 47
3.6 Discussion . . . . . 52

**Chapter 4 Multiple-Interface Measurements** **54**
4.1 Modeling of the Single-Barrier Structure . . . . . 54
4.2 Determination of the Conduction Band Offset . . . . . 57
4.3 Determination of the Phase Lag *d* . . . . . 59
4.4 Electron-Wave Interference Effects . . . . . 62
4.5 Discussion . . . . . 66

**Chapter 5 Resonant Device Measurements** **67**
5.1 Background . . . . . 68
5.2 Resonant Device Design . . . . . 71
5.3 Low-Temperature Measurements . . . . . 74
5.4 Room-Temperature Measurements . . . . . 80
5.5 Discussion . . . . . 82

**Chapter 6 Detection of single monolayer fluctuations in the thickness of a buried quantum well** **84**
6.1 Experimental Configuration . . . . . 85
6.2 Experimental Measurements . . . . . 87

6.3 Discussion . . . . . . . . . . . . . . . . . . . . . . . . . . . . . . . . . . . 91

**Chapter 7 Conclusions** **93**

7.1 Summary of Results . . . . . . . . . . . . . . . . . . . . . . . . . . . . . 93

7.1.1 Semiclassical BEES Model . . . . . . . . . . . . . . . . . . . . . . . 94

7.1.2 Single-Interface Measurements . . . . . . . . . . . . . . . . . . . . 94

7.1.3 Multiple-Interface Measurements . . . . . . . . . . . . . . . . . . . 96

7.1.4 Resonant Device Measurements . . . . . . . . . . . . . . . . . . . . 96

7.1.5 Application to Materials Diagnostics . . . . . . . . . . . . . . . . . 97

7.2 Future Research . . . . . . . . . . . . . . . . . . . . . . . . . . . . . . 98

**Bibliography** **102**

**Vita** **109**

# List of Tables

3.1 Experimental results of fitting simulations with various values of $s$ to Au/Si(111), Au/Si(100), and Au/GaAs(100) spectra. . . . . . . . . . . . . . . . . . . . . . 41

# List of Figures

1.1 A schematic representation of the systematic approach used in this research for studying carrier transport in heterostructures. . . . . . . . . . . . . . . . 3
1.2 Schematic diagrams for optical and transport measurement techniques. . . . 5
1.3 A schematic and band diagram of a scanning tunneling microscope. . . . . . 9
1.4 A schematic and band diagram of the BEES technique. . . . . . . . . . . . 10

2.1 The semiclassical BEES model and the four distinct physical phenomena that dominate its behavior. . . . . . . . . . . . . . . . . . . . . . . . . . . . 20
2.2 An ellipsoidal constant energy surface in momentum space. . . . . . . . . . 26
2.3 The electron distribution incident upon the base-semiconductor interface corresponding to various values of the scattering parameter $s$. . . . . . . . . . . 31

3.1 Constant energy ellipsoids and corresponding allowed set of interface wavevectors for Si(100). . . . . . . . . . . . . . . . . . . . . . . . . . . . . . 39
3.2 Constant energy ellipsoids and corresponding allowed set of interface wavevectors for Si(111) . . . . . . . . . . . . . . . . . . . . . . . . . . . . . 39
3.3 Simulation of BEES current for an Au/Si(111) diode for various amounts of elastic scattering. . . . . . . . . . . . . . . . . . . . . . . . . . . . . . 40
3.4 Analogy between the electron-wave transmission past an ideal potential step and the BEES experimental configuration. . . . . . . . . . . . . . . . . . . 44
3.5 An experimental Au/Si(100) spectrum fit to both the $T(E)$ and $T = 1$ models. Although both models appear to fit, the inset shows the threshold region where the $T(E)$ model provides a better description than the $T = 1$ model. 46
3.6 An experimental Au/GaAs(100) spectrum fit to both the $T(E)$ and $T = 1$ models. Although both models appear to fit, the inset shows the threshold region where the $T(E)$ model clearly provides a better description than the $T = 1$ model. . . . . . . . . . . . . . . . . . . . . . . . . . . . . . . 47
3.7 The mean squared error between the experimental spectrum and the simulations is plotted as a function of the upper fit voltage, $V_{fit}$ . . . . . . . . . 49
3.8 The effect of an energy-dependent effective-mass was investigated by fitting the data with simulations calculated using different combinations of non-parabolicity factors. . . . . . . . . . . . . . . . . . . . . . . . . . . . 51

4.1 A schematic of the MBE grown $Ga_{0.8}Al_{0.2}As$ single-barrier heterostructure. 55
4.2 Band diagrams for the two models used to describe electron transport in the single-barrier heterostructure. . . . . . . . . . . . . . . . . . . . . . . . 56
4.3 Comparison of models to raw experimental BEES data ($T = 77$ K, $I_t = 10$ nA) in the threshold region of spectra taken on the Au/Single-Barrier structure. 58

4.4 The mean-squared-error between the experimental spectrum and each model as a function of the model input region thickness $d$ in monolayers (ML). Inset shows the ideal band diagram for the heterostructure. . . . . . . . . . . . . . 60
4.5 A histogram of the values of the phase lag for 84 spectra taken on a typical single-barrier device. . . . . . . . . . . . . . . . . . . . . . . . . . . . . . . . 62
4.6 second-derivatives of the experimental and model BEES spectra from Fig. 4.3 ($T = 77$ K). . . . . . . . . . . . . . . . . . . . . . . . . . . . . . . . . . . . . 63
4.7 Experimental second-derivative spectrum acquired at 7 K compared with both the simple and the complete BEES models. . . . . . . . . . . . . . . . . 64

5.1 BEES measurement of the normal-incidence electron transmittance. . . . . 70
5.2 Schematic diagram, band diagram, and plots of the ideal and thermally broadened transmittance functions for the designed quantum interference filters. . . . . . . . . . . . . . . . . . . . . . . . . . . . . . . . . . . . . . . . 72
5.3 Band diagram, electron transmittance, and experimental second derivative spectrum with model fits for the half-electron-wavelength Fabry-Perot quantum interference filter . . . . . . . . . . . . . . . . . . . . . . . . . . . . . 75
5.4 Band diagram, electron transmittance, and experimental second derivative spectrum with model fits for the quarter-electron-wavelength Fabry-Perot quantum interference filter . . . . . . . . . . . . . . . . . . . . . . . . . . . 77
5.5 Experimental second-derivative spectrum with model fits for the quarter-electron-wavelength Fabry-Perot quantum interference filter taken at $T = 7$ K. 79
5.6 Second-derivatives of the experimental and modeled BEES spectra for (a) the half-electron-wavelength and (b) the quarter-electron-wavelength devices for data acquired at $T = 300$ K. . . . . . . . . . . . . . . . . . . . . . . . 81

6.1 A schematic representation of the semiconductor half-electron-wavelength filter measured. . . . . . . . . . . . . . . . . . . . . . . . . . . . . . . . . . . 87
6.2 Effect of ±1 ML thickness fluctuation of buried GaAs quantum well on the corresponding normal-incidence electron transmittance function. . . . . . . 89
6.3 Effect of ±1 ML thickness fluctuation of buried GaAs quantum well on the experimental BEES second-derivative spectrum. . . . . . . . . . . . . . . . . 90

# Summary

The microelectronics industry is diligently working to achieve the goal of gigascale integration (GSI) by early in the 21st century. For the past twenty-five years, progress toward this goal has been made by continually scaling down device technology. Unfortunately, this trend cannot continue to the point of producing arbitrarily small device sizes. One possible solution to this problem that is currently under intensive study is the relatively new area of quantum devices. Quantum devices represent a new class of microelectronic devices that operate by utilizing the wave-like nature (reflection, refraction, and confinement) of electrons together with the laws of quantum mechanics to construct useful devices. One difficulty associated with these structures is the absence of measurement techniques that can fully characterize carrier transport in such devices.

This thesis addresses this need by focusing on the study of carrier transport in quantum semiconductor heterostructures using a relatively new and versatile measurement technique known as ballistic electron emission spectroscopy (BEES). To achieve this goal, a systematic approach that encompasses a set of progressively more complex structures is utilized. First, the simplest BEES structure possible, the metal/semiconductor interface, is thoroughly investigated in order to provide a foundation for measurements on more the complex structures. By modifying the semiclassical model commonly used to describe the experimental BEES spectrum, a very complete and accurate description of the basic structure has been achieved. Next, a very simple semiconductor heterostructure, a $\mathrm{Ga}_{1-x}\mathrm{Al}_x\mathrm{As}$ single-barrier structure, was measured and analyzed. Low-temperature measurements on this structure were used to investigate the band structure and electron-wave interference effects in the $\mathrm{Ga}_{1-x}\mathrm{Al}_x\mathrm{As}$ single barrier structure. These measurements are extended to a simple quantum device by designing, measuring, and analyzing a set of complementary electron-wave Fabry-Perot quantum interference filters which included both a half- and a quarter-electron-wavelength resonant device. High-resolution, low noise, BEES spectra obtained on these devices at low-temperature were used to measure the zero-bias electron transmittance as a function of injected energy for these resonant devices. Finally, by analyzing BEES spectra taken at various spatial locations, one monolayer variations in the thickness of a buried quantum well have been detected.

# Chapter 1

# Introduction

For the past twenty-five years the paradigm of the microelectronics industry has been to produce devices that are smaller, faster, and cheaper. This increased productivity and reduced cost has been accomplished by continually scaling down current device technology. This miniaturization (described by Moore's law) has produced an astounding exponential increase in the number of transistors per unit area and has increased device speed by several orders of magnitude [1]. To achieve such miraculous results several "limitations" that were predicted to be unsurpassable have been pushed aside by hard work, ingenious thinking, and perseverance. Unfortunately, this trend is fundamentally restricted by the laws of quantum mechanics, thermodynamics, and the speed of light in a vacuum, and cannot continue to the point of producing arbitrarily small device sizes and unlimited clock speeds.

Fortunately, very intensive research is currently being conducted on a number of promising solutions. One area in particular that has received a lot of attention recently is that of quantum devices [2]. These represent a new class of microelectronic devices, which operate by utilizing the wave-like nature of electrons together with the laws of quantum mechanics. In these devices, electron waves are reflected, refracted, and diffracted in a manner that is analogous to the propagation of electromagnetic eral dielectrics [3]. One major difference between electron-waves and electromagnetic waves is the magnitude of the wavelength $\lambda$. Given that the wavelength of the electron ($\lambda_e$) in a typical semiconductor is on the order of nanometers, it is obvious that these devices are more difficult to produce than analogous electromagnetic devices. Suitable quantum device structures typically rely heavily on the ability to produce structures in which the thickness of the individual layers can be controlled with atomic precision. The realization of quantum device technology has thus been made possible by advances in growth techniques such as molecular beam epitaxy (MBE) and by new nanolithography techniques such as electron-beam and x-ray lithography.

Complementary to device production is device testing. Developing the new technology needed for quantum devices requires numerous new experimental measurement techniques. These measurements need to encompass an entire suite of techniques that are capable of determining quantities ranging from terminal characteristics down to the quantum states on which the devices are based. For measuring electron-wave effects, numerous optical and transport techniques have been used with a significant amount of success. A sampling of these include Fourier transform infrared spectroscopy (FTIR), photoluminescence (PL), photoreflection (PR), current-voltage spectroscopy (I-V), and capacitance-voltage (C-V) spectroscopy, for example. One of the major goals of these measurements is to determine the energy position and energy width of bound and quasibound electron (and hole) resonances. The properties of these resonances play a vital role in device operation and need to be well understood. Unfortunately, many of the conventional optical and transport measurements used to measure quantum devices suffer from limitations that can make their findings difficult to interpret.

## 1.1 Research Objectives

The objective of the proposed research is to achieve a better understanding of ballistic carrier transport in quantum semiconductor devices and, in turn, determine the limitations of BEES as an experimental tool for investigating such quantities. This goal is realized by utilizing a systematic approach that encompasses a set of progressively more complex structures. A schematic of this approach is shown in Fig. 1.1. The research initially fo-

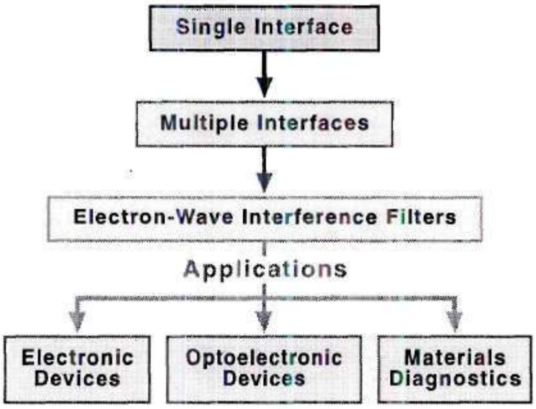

Figure 1.1: A schematic representation of the systematic approach used in this research for studying carrier transport in heterostructures. By utilizing a systematic approach that encompasses a set of progressively more complex structures, a very complete understanding of ballistic carrier transport in heterostructures becomes possible. The knowledge of these basic structures will form the basis for future measurements on progressively more complex devices.

cuses on the simplest test structure, a single interface device, which consists of only a metal/semiconductor (M/S) boundary. This simple structure is used to develop and test the accuracy and flexibility of the model developed for describing the electron transport through single and multiple interface devices. This very basic and simple device must be understood in great detail since these measurements form the foundations on which the remaining research is based. These measurements are then extended to multiple interfaces by analyzing a single-barrier structure (namely GaAs/$Ga_{1-x}Al_xAs$/GaAs). This device represents the simplest practical heterostructure and is the next logical step in complexity. Using the excellent description of this simple heterostructure that was achieved, measurements on much more complex heterostructures were performed. Finally, using the extensive base of knowledge gained from these fundamental structures, a materials diagnostics application was explored. By utilizing this systematic approach, a very complete understanding and an accurate description of these becomes possible.

## 1.2 Background and Related Previous Work

### 1.2.1 Measurement Techniques

Techniques for measuring electron-wave interference effects in quantum semiconductor structures typically fall into two very general categories: optical and transport. The goal of these measurements is to characterize accurately the perpendicular carrier transport in electron-wave devices. One of the most powerful and useful quantities for characterizing such transport is the electron transmittance through the structure as a function of the injected energy, $T(E)$. Unfortunately, conventional optical and transport measurements suffer from limitations that make measuring $T(E)$ directly very difficult.

Schematic diagrams for both optical and transport measurements are shown in Fig. 1.2. For optical measurements, most of the difficulties arise from the indirect nature of the technique. In this context, indirect means that the absorption/transmission characteristics measured can only detect the transitions between resonant levels ($\Delta E_{01}$ and $\Delta E_{02}$ in Fig. 1.2a). In other words, the energy location and width in energy of an individual state cannot be determined. Additionally, the symmetry of some device types places limitations on the allowable transitions. These limitations are due to dipole matrix element selection rules which relate the absorption probability for a particular transition $E_1 \rightarrow E_2$ to the overlap of the corresponding wavefunctions $\psi_1$ and $\psi_2$. This is illustrated in Fig. 1.2a where the transition $\Delta E_{02}$ may be rendered unobservable because of the symmetry of the corresponding wavefunctions. The situation is further complicated by optical polarization constraints. Even if a given transition is quantum mechanically favorable, specific polarizations may be needed to excite the transition due to the free electron like behavior in non-confined directions. These polarization limitations also depend upon the device symmetry and the type of carrier confinement utilized. Finally, an unavoidable aspect of these techniques is their macroscopic nature. This can be a major disadvantage if the device under consideration is very sensitive to small or local imperfections in the structure.

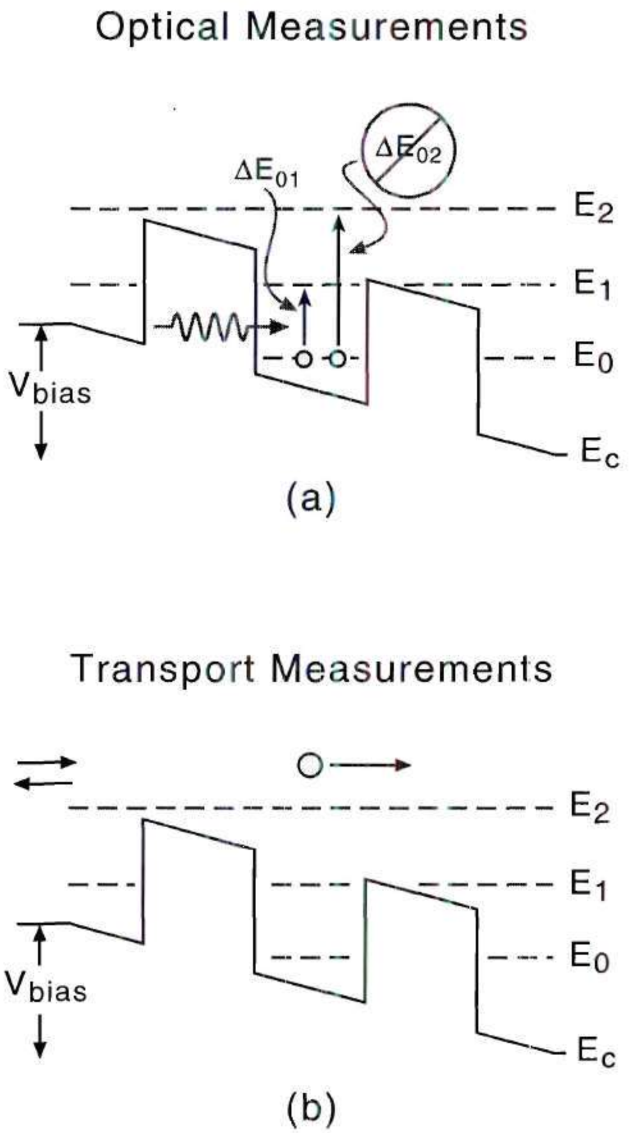

Figure 1.2: Schematic diagrams for both optical and transport measurement techniques. (a) Optical methods indirectly probe resonant states and can only detect transitions between (certain) energy levels. (b) Transport measurements provide a direct measurement of resonant states but suffer from problems due to band bending, doping induced scattering, and poor injection collimation.

Transport measurements, which provide a nice complement to optical techniques, can detect *individual* quasibound states. These measurements can be performed in both a two- and a three-terminal configuration and have the advantage of being relatively easy to perform [4–10]. The three-terminal configuration is the most useful due to its ability to tune the resonances without changing the distribution of injected electrons [7, 9]. A schematic diagram of a two-terminal transport measurement is shown in Fig. 1.2b where the quasibound states in question are detected as features in the current-voltage (I-V) spectrum. Unfortunately, most transport measurements suffer from limitations which inhibit their ability to measure electron wave interference effects [11]. First, the emitter is typically degenerately doped to support operation at low temperatures. This degenerate doping becomes the source of both impurity and electron-electron scattering, and produces a large built-in potential. This potential induces a significant amount of band bending which alters the shape of the band profile (and thus the interference effects) under consideration. Second, in the three-terminal configuration, the base contact also must be degenerately doped and, because it is buried in the device, cannot be accessed easily. The degenerate doping also leads to even more scattering and the contact accessibility can make fabrication difficult. Third, the energy of the injected electrons is typically adjusted using an applied bias across the device. To change the injected energy the emitter must be redesigned to inject electrons at a different energy. The potential-induced acceleration produces results that are difficult to interpret (and model) because of the coupling between the applied voltage and the device bias. Finally, as in the optical measurements, only a macroscopic average of the measured quantities can be acquired which severely limits the scope of the technique.

One possible measurement technique that can be used to overcome the limitations described in the previous section is a relatively new and versatile technique known as ballistic electron emission spectroscopy (BEES) [12, 13]. This is a scanning tunneling microscope (STM) based three-terminal transport measurement that was introduced by Bell and Kaiser [12, 14] for studying carrier transport properties at a M/S interface. It was originally used to measure the value and uniformity of the Schottky barrier height (SBH) $V_b$ with very high energy and spatial resolution. In the decade since, the technique has been extended dramatically and is currently used to measure a wide variety of transport characteristics [13]. The three-terminal configuration coupled with the nanometer-scale STM injector makes BEES well-suited for studying carrier (electron or hole) transport through semiconductor heterostructures. Its versatility provides the following advantages over other measurement techniques:

- very high spatial resolution ($\sim$ nm)
- very high energy resolution at low temperature
- the energy of the injected carriers is controlled by the bias on the STM tip and is *independent* of the bias applied across the device
- scattering and band-bending from degenerately doped emitter is eliminated because the carriers are provided by the STM tip
- injected current can be adjusted *independently* of injected energy
- base contact is easily accessible.

These characteristics make BEES a very attractive choice for measuring effects from carrier scattering in metals to electron-wave interference-effects in quantum devices. A recent review of the accomplishments of BEES (and its microscopic analog BEEM) is given in Ref. [13].

To gain an insight into how BEES works, a basic understanding of the STM is needed. STM is a scanned probe microscopy with sub-nanometer resolution that was introduced in 1981 by G. Binnig and H. Rohrer [15]. The microscope utilizes a vacuum tunneling probe and piezoelectric transducers to measure the topography (and density of states) of conducting surfaces. The vacuum probe consists of a very sharp (preferably atomically sharp) conducting electrode that is called the tip. The tip is attached to a piezoelectric transducer and is brought within close proximity to the sample surface for operation. The distance between the tip and sample is called the tunneling gap and is typically on the order of 1 nm. A schematic diagram of the STM is given in Fig. 1.3a. For such small tip-sample separations, the wavefunctions of the electrons in the tip overlap the wavefunctions of the electrons in the sample as shown in Fig. 1.3b. When a small voltage $V_T$ is applied to the tip (choosing the sample to be ground), electrons can tunnel through the vacuum barrier formed by the tunneling gap and form a tunneling current. The magnitude of the tunneling current is extremely sensitive to variations in the tip-sample separation because of the exponential decay of the electron wavefunctions into the vacuum barrier. In fact, a 0.1 nm change in the separation will increase the tunneling current by an order of magnitude.

To image the surface, the piezoelectric transducer is used to scan the tip in fine lateral steps. As the surface topography changes, the tip-sample separation, and thus the tunneling current, will change correspondingly. In practice, a feedback loop is used to keep the tunneling current constant by controling the tip-sample separation. Then, as the tip is scanned across the surface, the error signal $\Delta Z$ is used to drive the piezoelectric transducer that controls the tip-sample separation in order to keep the tunneling current constant. The surface can then be imaged by recording $\Delta Z$ as a function of position. Additionally, the STM can be used to perform scanning tunneling spectroscopy (STS) on the underlying sample. In this case, the tip-sample separation and position are held fixed (the feedback loop is disabled) while $V_T$ is changed. By monitoring the tunneling current as a function of $V_T$, information about the local electronic structure such as the density of states can be obtained.

To perform BEES, the the conducting substrate used in a normal STM is made very thin ($< 10$ nm) and is deposited onto the surface of a semiconductor. A schematic of the BEES configuration along with a band diagram is shown in Fig. 1.4. In this configuration, the STM tip forms the emitter, the metal film acts as the base, and the semiconductor is

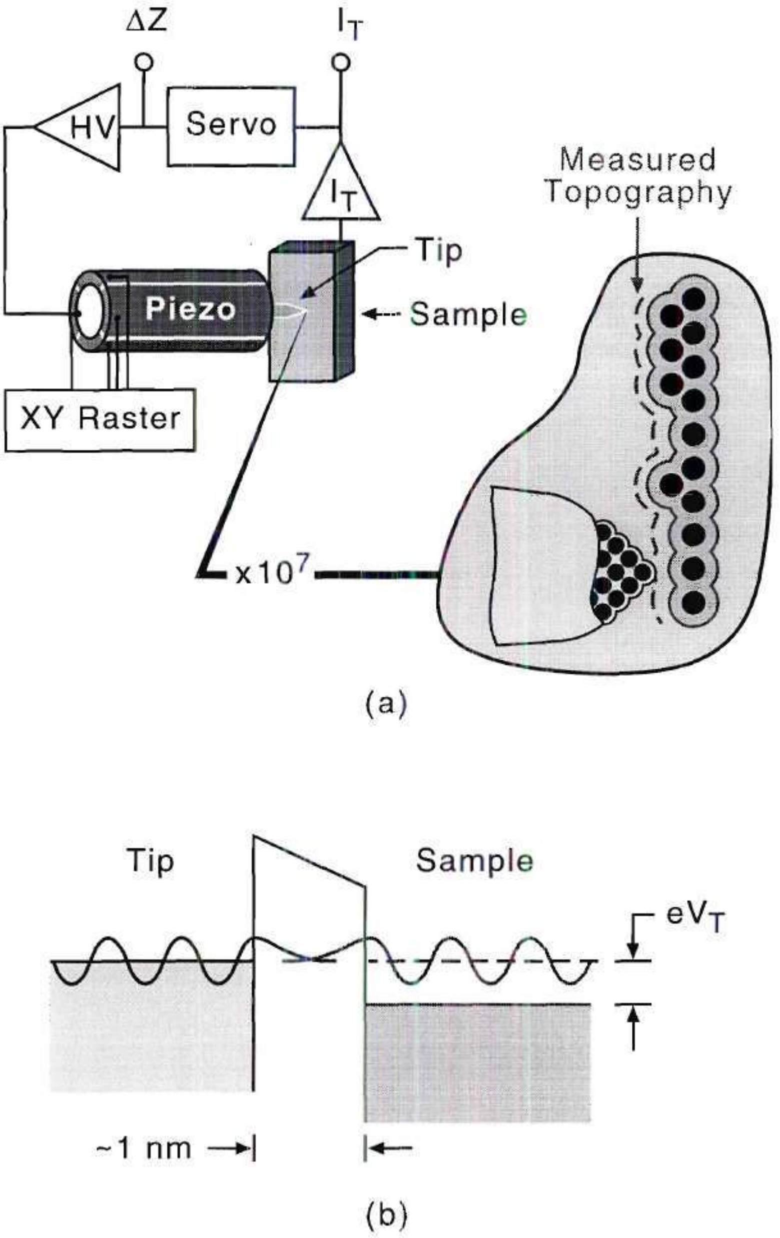

Figure 1.3: (a) A schematic diagram of a scanning tunneling microscope. An atomically sharp tip is brought within a nanometer of a conducting sample. The electron wavefunctions in the tip overlap the wavefunctions in the sample. (b) Band diagram of the tip and sample with an applied bias $V_T$. Due to the bias, and to the wavefunction overlap, some of the electrons will tunnel from the tip to the sample forming a tunneling current.

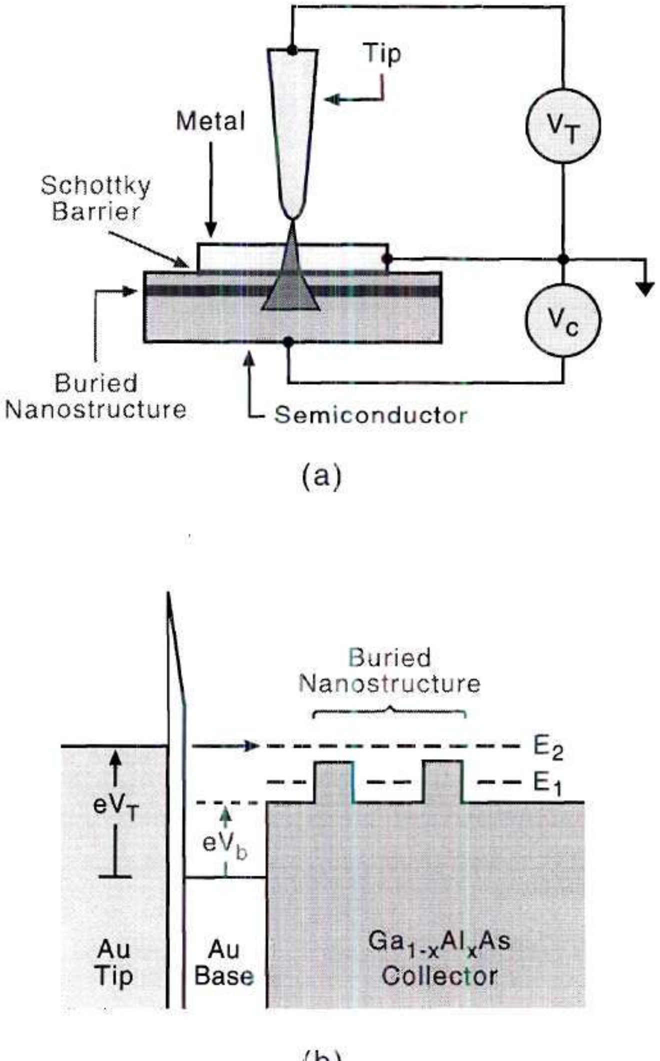

Figure 1.4: (a) A schematic diagram of BEES. The tip of an STM is used to inject carriers into a thin metal film where they travel ballistically and probe the transport properties of the buried interface. (b) The band diagram for BEES showing that only electrons with an energy greater than the Schottky barrier are transmitted.

the collector of the structure. To perform the spectroscopy, ballistic electrons are injected into the base with a precise energy distribution that is controlled by the STM tip bias. Since the base contact is thin, a fraction of the injected carriers propagate ballistically through the metal film and reach the M/S interface with their original energy distribution. BEES is performed by monitoring the number of electrons transmitted into the collector as a function of the applied tip bias. The technique is similar to STS with the exceptions that the tunneling current, not tunneling gap, is held constant and that the carriers are collected by the semiconductor, not metal. In this manner, ballistic transport characteristics of the metal (or metals if a multilayer film is used), the M/S interface, and/or the buried semiconductor can be measured.

BEES was first used to determine both the value and spatial uniformity of the Schottky barrier $V_b$ formed at the M/S interface [12, 13]. A detailed understanding of this simple single-interface structure is necessary because of the integral role that the Schottky barrier has in determining the threshold of the BEES $I$-$V$ spectrum. This threshold occurs because only carriers that arrive at the M/S interface with an energy greater than $V_b$ can be transmitted into the semiconductor collector. Thus, when $V_T < V_b$ , the carriers have insufficient energy to overcome the Schottky barrier and there is no collector current. As the bias is increased above $V_b$, some of the injected electrons will have sufficient energy to overcome the barrier and are transmitted into the semiconductor. These carriers produce a non-zero collector current that is called the BEES current. Therefore, by measuring the collector current as a function of tip bias, BEES can be used to determine directly the *local* Schottky barrier height for a given spatial location. The spatial uniformity of the barrier height can be determined by scanning the tip laterally and taking BEES spectra at various locations (typically on a grid) within the scanned image [16–20]. Additionally, the shape and magnitude of the current above threshold can be used to derive information about the carrier transport in both the metal and the semiconductor.

### 1.2.2 BEES Measurements of Single Interface Structures

Most of the BEES measurements to date have been on single-interface (M/S) structures. The majority of these measurements have focused on determining the SBH. The SBH for a given material system can be determined for both n-type and p-type contacts by choosing the appropriate substrate doping. For material systems where the Fermi level is pinned at the M/S interface, the sum of the two barrier heights can provide an estimate of the semiconductor band gap. Most of the measurements to date have been made on n-type material systems because the reduced SBH on p-type materials produces a larger leakage current, thus requiring low-temperature measurements to reduce noise current due to thermal leakage of carriers over the barrier. The first ballistic electron experiments were performed by Bell and Kaiser [12, 14] who measured the SBH of Au/Si(100) and Au/GaAs(100). The first ballistic hole spectroscopies were performed by Hecht *et al.* [21] on Au/Si(100) and Au/GaAs(100). Later, O'Shea *et al.* [22] performed hole spectroscopy on Au/$Ga_{1-x}Al_xAs$(100) and determined the valence band offset as a function of the aluminum composition $x$. Ludeke *et al.* [23–29] have measured the SBH on several material systems including (Au, Ag, Bi, Mg, Cu, Ni)/GaP(100), Pd/Si(100), Pd/Si(111), $NiSi_2$/n-Si(111) 7*7, Cr/GaP(110), and have investigated Si-based MOS structures. Working with Pt/Si(100), Niedermann *et al.* [30, 31] observed that the SBH changes as the thickness of the Pt layer is varied. Some additional work on III-V compounds was carried out by Tsau *et al.* [32] who looked at CoGa/GaAs(100). The measurements failed to provide the SBH as measured by conventional techniques because the magnitude of the current transmitted into the $\Gamma$ minimum was smaller than the noise currents. Investigations of II-VI compounds such as ZnSe have been performed by Coratger *et al.* [33] in which variations in the value of the SBH with position were attributed to microclusters of different ZnSe phases at the interface. Recently, Ke *et al.* [34] have used BEES to investigate the SBH and band structure of porous silicon, a promising new material for optoelectronic applications in silicon [35].

Finally the three-terminal configuration of BEES has been explored by Davies *et al.* [36] and O'Shea *et al.* [22] who have applied a reverse bias to Au/Si(100) and Au/$Ga_{1-x}Al_xAs$, respectively. Both groups' results show that the decrease in the SBH, due to the applied potential, is in good agreement with a model that takes into account image potential lowering of the barrier [37].

BEES is also capable of detecting band minima other than the lowest energy minimum which forms the SBH. In GaAs, for example, there are two additional band minima within 0.5 eV of the Schottky barrier (which is formed by the $\Gamma$-minimum located at the center of the first Brillouin zone). These minima are the 8 $L$-minima (0.28 eV above $\Gamma$), located along the (111) axes, and the 6 $X$-minima (0.5 eV above $\Gamma$), located along the (100) axes. Once the energy of the incident electrons is large enough to reach these higher valleys, additional regions of phase space are accessible for transmission. With the addition of these minima, the BEES current becomes a summation over all of the accessible states and thus exhibits multiple thresholds (one for each set of symmetry-related minima). The locations of these minima can be determined in a nearly model-independent manner by locating linear kinks in the first derivative of the spectrum $dI_c/dV$. The energy position of each kink represents the location of the appropriate minimum. Values for the higher lying $L$ and $X$ minima in GaAs have been investigated using BEES spectra obtained on n-type GaAs [14]. These results yielded a $\Gamma$–$L$ splitting of 0.28 eV and a $\Gamma$–$X$ splitting of 0.48 eV, both in good agreement with accepted values [38]. For spectra obtained on p-type GaAs, Hecht *et al.* [21] were able to determine the value of the valence band splitting, but they were not able to determine the splitting for the spin-orbit band.

All of the previously noted measurements have confirmed results and quantities that are already known by other measurement techniques. The ability of BEES to reveal information about new and less understood material systems has recently been exploited. BEES measurements on the promising new III-V compound GaN have revealed information on the uniformity and purity of the film [39]. Pelz *et al.* [40] have investigated the location of the band minima in different polytypes of SiC, and have reported the first direct evidence of a second conduction band minimum in 4H-SiC that is approximately 0.14 eV above the Schottky barrier.

All of these results exhibit the power and versatility of BEES for investigating the transport properties of both materials that are well understood, and new materials that are not well understood. The single-interface M/S structure is fundamental to the technique and is present in all BEES measurements. Thus, an extremely accurate description of these simple structures facilitates the understanding of more complicated structures.

### 1.2.3 BEES Measurements of Semiconductor Heterostructures

To study the carrier transport of semiconductor heterostructures with BEES, the bulk semiconductor collector is replaced with a buried heterostructure as illustrated in Fig. 1.4. The transmittance can be measured for any given device bias, including zero. BEES is sensitive to the electron transmittance because $T(E_x, E_t)$ plays an integral role in the model. To extract the normal incidence electron transmittance from the BEES spectra, Henderson *et al.* [11] showed numerically that the second derivative of the BEES current ($d^2I_c/dV^2$ where $V$ is the applied tip bias) is needed. Later, Smith and Kogan [41] showed that, for the effective mass model commonly used to describe the BEES current, $d^2I_c/dV^2$ is proportional to the normal incidence transmittance multiplied by a slowly varying function. Given the energy resolution of BEES, the transmittance can thus be determined with an energy resolution that is on the order of 3.5 $k_BT$. A complete characterization of the device should thus be possible by applying a series of base-collector voltages, and measuring the transmittance for each bias.

A large portion of the BEES measurements on heterostructures have not involved the use of the $d^2I_c/dV^2$ spectrum because of the difficulty involved in differentiating twice the small signals (typically $\sim$ pA) obtained. Instead they have concentrated on using the features in the spectrum to determine properties of the buried layers such as band offsets.

For example, the group at the University of California at Santa Barbara have used BEES to investigate transport through thin InAs layers [42], band offsets in GaInP/GaAs heterostructures [43], tunneling in 0-D quasibound states in InAs quantum dots [44], the band offset of GaSb quantum dots [45], and band offsets and inter-valley scattering in $\mathrm{Ga}_{1-x}\mathrm{Al}_x\mathrm{As}$ [22]. Ke *et al.* [46] have used BEES to study the band offset and electron tunneling in AlAs barriers of various thicknesses and found that to model the spectra accurately, the square-law approximation must be modified for the smaller thicknesses to account for electron tunneling through the AlAs barrier. Similarly, they performed measurements on laterally patterned superlattices grown on vicinal substrates which revealed the expected periodicity in the BEEM image, but not in the STM image of the topography [47]. Eder *et al.* [48, 49] designed and implemented a low-dimensional electron gas (in place of a degenerately-doped bulk substrate) as a novel collector for performing measurements at liquid helium temperatures. They used the new collector configuration to investigate buried quantum-wires at 4.2 K. These measurement show that BEES can provide a variety of useful information about transport in heterostructures, but, due to the extremely large signal-to-noise ratio needed, do not utilize the relationship between the electron transmittance and the second-derivative spectrum.

The first experimental verification of the similarity of the electron transmittance to the $d^2I_c/dV^2$ spectrum was provided by Sajoto *et al.* [50] who performed BEES on a $\mathrm{Ga}_{1-x}\mathrm{Al}_x\mathrm{As}$ double-barrier resonant-tunneling diode (DBRTD) structure at temperatures ranging from $T = 77$ to 300 K. The peaks in the second-derivative spectra were found to be in good agreement with the calculated values of the quasibound states in the structure and with the location of the band minima ($\Gamma$, $L$, and $X$) in GaAs and $\mathrm{Ga}_{1-x}\mathrm{Al}_x\mathrm{As}$. The temperature dependence of the band gaps associated with each band minimum was determined and these agreed well with accepted values [38]. A reference sample in which the DBRTD was replaced with a thick barrier was used to determine a conduction band offset of $\Delta E_c = 0.35$ eV for $x = 0.42$, the composition used in the DBRTD, which also agrees well with the accepted value. Later, the model derived by Smith and Kogan [41] was compared to the second-derivative spectra on the DBRTD and was found to provide a relatively poor description of the data. These measurements confirmed the utility of the method, but did not provide a stringent test of the accuracy of BEES in determining the electron transmittance *function*. It is important to be able to model and reproduce features other than just peak positions. Features such as peak width and peak-to-valley ratio contain important information such as the carrier lifetimes of both tunneling and above-barrier quasibound states. Thus, to date, a verification of the direct proportionality of the second-derivative spectrum to the electron transmittance has not been performed. Without such a measurement, the true potential of BEES as an analysis tool will not be fully realized.

## 1.3 Thesis Overview

The semiclassical model developed by Bell and Kaiser has received widespread exceptance as a simple and straightforward model for describing the experimental BEES spectra. However, this model does not correctly describe the magnitude of the measured current for materials such as Si(111) which do not have any states available for transmission at near-normal incidence. In Chap. 2, to account for the observed magnitudes, the scope of this model is extended by including the effect of elastic scattering in the metal overlayer. The elastic scattering is included via a scattering parameter $s$ which allows the momentum distribution incident upon the metal/semiconductor interface to be varied from planar tunneling (forward peaked) to isotropic (completely randomized). In addition, the effect of the quantum transmission past the metal/semiconductor interface is determined for transmission between two arbitrary materials and is included in the model. In this analysis, the model correctly developed includes all available phase space for each of the relevant band minima.

To optimize the extended model developed, high-resolution low-temperature BEES spectra on Au/Si(100), Au/Si(111), and Au/GaAs(100) are obtained and compared to the model in Chap. 3. By utilizing the near-threshold region of the spectra, the electron momentum distribution is shown to be nearly isotropic in angle. The effect of the single-interface quantum transmittance is conclusively shown to change the shape of the BEES spectrum. By including the transmittance in the model, an accurate description of the data for all three interface systems is achieved and presented. The stability of the various commonly used models was investigated, and it is explicitly demonstrated that the model which includes the quantum transmittance provides the most accurate description of the data over the largest voltage range.

In Chap. 4, high resolution BEES spectra are reported for a $GaAs/Ga_{1-x}Al_xAs/$ GaAs single-barrier heterostructure at 7 K and 77 K. Second-derivative spectra computed from $I$–$V$ data obtained on this structure exhibit features that are due to electron-wave interference effects that are caused by finite thickness of the input region (the distance between the metal/semiconductor interface and the $Ga_{1-x}Al_xAs$ potential barrier). These features have been detected even though this structure has not been designed nor optimized to show such effects. It is shown that these spectra can be described within the framework of the model if the transmission/reflection from all the relevant interfaces are included and if the thickness of the input region is optimized for each spectra. In Chap. 5 these measurements are extended to include two complementary resonant devices (a half- and a quarter-electron-wavelength Fabry-Perot filter) that are designed and optimized to show constructive and destructive interference effects. Using high-resolution spectra obtained on these structures at 7 K, 77 K, and 300 K, the similarity between the normal-incidence electron transmission function and the BEES second-derivative spectrum is explicitly demonstrated. These measurements achieve the the temperature-limited resolution of the technique and represent the first experimental demonstration of this relationship.

To provide a practical application of the results and techniques established in this work, Chapter 6 illustrates the ability to perform extremely local materials diagnostics using BEES. By utilizing the measurements obtained on the half-electron-wavelength filter, the detection of single-monolayer fluctuations in the thickness of a buried quantum well has been accomplished. These small thickness variations have been detected by measuring the change in the energy separation between two resonant peaks (which depend on the thickness of the well region) in the quantum transmittance. Finally, in Chap. 7, the results of the thesis are summarized and discussed, and possible directions for future research are presented.

# Chapter 2

# Extended Semiclassical BEES Model

## 2.1 Background

Using measurements taken on Au/Si(100) and Au/GaAs(100), Bell and Kaiser [12, 14] developed a kinematic model to describe the carrier transport in simple M/S structures using a planar tunneling model to describe the electron tunneling between the tip and base [51] and by requiring conservation of energy and momentum across the M/S interface. This model, known as the Bell-Kaiser model, gives the ratio of the collector current to the tip current as

$$\frac{I_c}{I_t} = R\frac{\int_0^\infty D(E_x)\int_0^{E_{max}} f(E)T(E_x, E_t)\, dE_t dE_x}{\int_0^\infty D(E_x)\int_0^\infty [f(E) - f(E + eV_T)]\, dE_t dE_x} \tag{2.1}$$

where $E = E_x + E_t$ is the electron energy in the tip, $E_x$ the energy associated with the component of the momentum normal to the interface, $E_t$ the energy associated with the component of the momentum parallel to the interface, $f(E)$ is the Fermi-Dirac distribution, $D(E_x)$ is the tunneling probability [51], $R$ is a scale factor (assumed to be energy independent) that accounts for scattering, $E_{max}$ is the maximum energy (for a given $E_x$) that can be transmitted to the collector accounting for total internal reflection, and $T(E_x, E_t)$ is the quantum mechanical transmission coefficient for transmission over the Schottky barrier. The ratio of the collector to tip current is calculated to account for the variation in the tunneling gap as a function of applied bias that occurs in the experimental data acquisition.

As shown in Fig. 2.1, this model is dominated by four distinct physical phenomena: The Fermi statistics in the metal tip and base, the ratio of the allowable momentum space

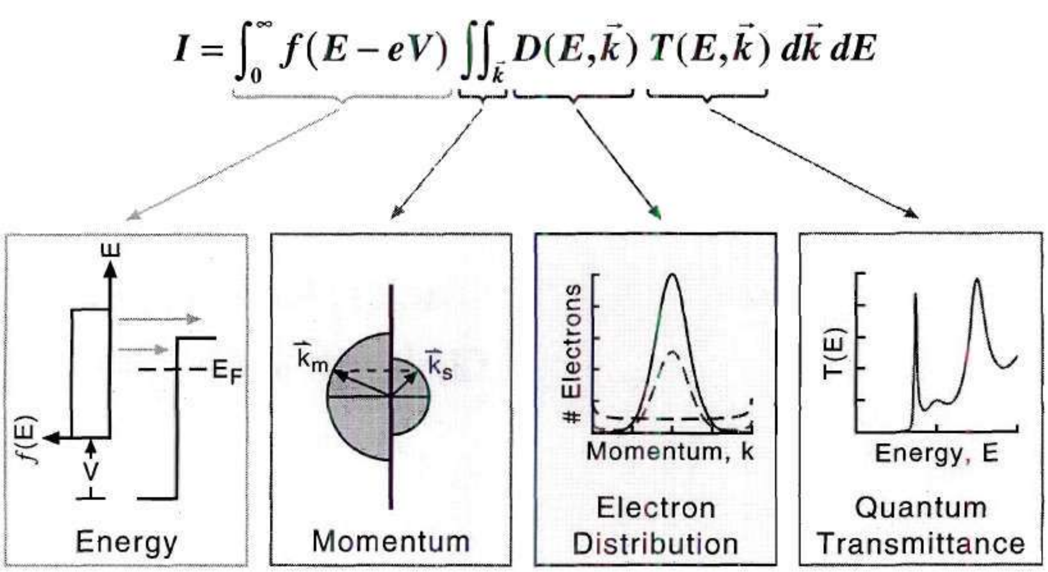

Figure 2.1: The semiclassical BEES model and the four distinct physical phenomena that dominate its behavior. In this formalism, the energy resolution is set by the Fermi statistics and the shape is dominated by the conservation of parallel momentum. The electron transmittance and the momentum distribution influence the fine structure of the spectrum which can be obtained through differentiation.

areas of the metal and semiconductor, the distribution of electron momenta at the interface $D(E_x)$, and the electron transmittance $T(E_x, E_t)$. In this model, the energy resolution is derived from the Fermi statistics (which, due the the width of the derivative of $f(E)$, is $\sim 3.5\ k_BT$) and the shape is mainly determined by phase matching condition between the metal base and the semiconductor collector. The electron transmittance and the momentum distribution influence the fine structure of the spectrum and can be obtained through differentiation. Due to the subtle nature of these effects, the electron transmittance and the momentum distribution are the least understood aspects of the model and have drawn the most attention.

To obtain high-resolution measurements or to view transport in materials with a small band gap (SBH $<$ 0.8 eV), BEES must be performed at low-temperature. At low temperature, several assumptions can be made that greatly simplify the model. First, the

Fermi function can be assumed to be a step function in energy, allowing the complicated expression to be absorbed into the limits of integration over energy. Second, the momentum distribution within the critical angle of transmission into the semiconductor can be assumed to be constant. With these assumptions, Eq. 2.1 can be evaluated in closed form. Thus, at cryogenic temperatures and for voltages near threshold the model can be approximated by a power law given by

$$I_c(V) = R'(V - V_b)^n \tag{2.2}$$

where $R'$ is again a scale factor (assumed to be energy independent), and the value of the the power $n$ depends on whether or not the electron transmittance is included or assumed to be unity for carriers with an energy greater than the SBH. If the transmittance is neglected, the model reduces to quadratic in applied voltage ($n = 2$) [52]. However, if it is included and assumed to be proportional to $E^{1/2}$, the exponent is $5/2$ [53]. Both of these power laws have been used repeatedly to determine the value of the local SBH because of their simplicity and computational efficiency, even though they are only valid over a small range of $(V - V_b)$.[1] This range of validity is evaluated experimentally in Chap. 3 using high-resolution BEES spectra obtained at both 7 K and 77 K on Au/Si and Au/GaAs structures.

Due to the difficulty in detecting such a subtle effect, the inclusion of $T(E_x, E_t)$ in Eq. 2.1 has been the source of considerable debate since the model was first proposed. In practice, the effect of $T(E_x, E_t)$ could conceivably be rendered unobservable for several reasons: 1) The BEES current results from electron transmission summed over all incident angles and all injected energies. Thus phase space (kinematical) restrictions on these sums determine a large part of the spectral shape, which can mask the less obvious influence of quantum transmittance. 2) The transmittance function may approach unity within an energy range smaller than the experimental resolution, or conversely its intrinsic energy

---

[1] The complete model, though more accurate, can produce small fluctuations in $V_b$ depending on implementation. The power law approximation provides a simple standard for determining $V_b$, but is not used to analyze more complex phenomena.

dependence may be too weak to be observable. 3) Scattering events may redistribute the incident electron flux into other angles (elastic or inelastic scattering) or other energies (inelastic scattering). Either could impart a substantial energy dependence to the spectrum that swamps the effect of the quantum transmittance. Given these complications, the effect of the transmission coefficient was initially considered to be negligible and $T(E_x, E_t)$ was approximated by a step function given by

$$T(E) = T(E_x, E_t) = \begin{cases} 0 & E \leq eV_b \\ 1 & E > eV_b \end{cases} \tag{2.3}$$

which takes into account the minimum energy that can be transmitted due to the potential step formed by the Schottky barrier. Under this approximation, all of the carriers incident on the interface within the allowed regions of phase space are transmitted. Alternatively, if the effect of the quantum mechanical wave transmission/reflection at the potential step is included (assuming an abrupt interface), the transmission coefficient is given by

$$T(E) = T(E_x, E_t) = \begin{cases} 0 & E \leq eV_b \\ \frac{2n_l \cos\theta_l}{n_l \cos\theta_l + n_r \cos\theta_r} & E > eV_b \end{cases} \tag{2.4}$$

where $n_i = \sqrt{E_i/m_i^*}$ is the amplitude refractive index for each side of the interface ($i = l, r$), $\theta_i$ is the incident angle, and $\theta_t$ is the transmitted angle [3]. Lee and Schowalter [54] suggested that the effect of phonon scattering nearly cancels the effect of the quantum transmittance rendering it unobservable. Others [55] have suggested that strict parallel momentum conservation is not necessary because of scattering in the metal and at the M/S interface. Regardless, Ludeke *et al.* [25] showed that a reasonably good agreement with experimental data is obtained as long as the correct ratio of allowable momentum space for the metal and the semiconductor is used. Up to the present, the effect of the single-interface quantum transmittance had not yet been conclusively confirmed or disproved.

Before proceeding, the validity of using such a simplistic effective mass approach to treat the non-epitaxial M/S interface should be discussed. Semiclassical models that rely upon the effective mass approximation have proven to be so useful and intuitive in semiconductor physics that they are often applied to cases where the approximations of the model are not strictly valid. Nonetheless, model predictions in these instances are often quantitatively confirmed by experiment [56]. For ballistic transmission through a metal/semiconductor interface, some of the assumptions are indeed violated, yet it is worthwhile examining a semiclassical model for the quantum transmittance because a) it is tractable, and b) it is easily integrated into a calculation of the total transmittance through a collector composed of a semiconductor heterostructure device. In this work we have implemented a semiclassical model that includes the effects of quantum transmittance into *all* kinematically allowed states of the semiconductor. Previous studies have recognized the importance of "off-axis" band minima [25, 57, 58], but have not included the effects of angle and energy dependent transmittance into these states.

## 2.2 Inclusion of the Quantum Mechanical Transmittance for Non-Zone-Centered Band Minima

To obtain a complete description of the low-voltage BEES spectrum, a model that incorporates the amplitude effects in the near threshold region, in addition to phase constraints, has been developed. The amplitude effects are embodied in the quantum transmittance and in elastic scattering events, which change the incident electron trajectories. The phase effects determine the electron states that are available for transmission. Previously, only a small portion of the allowable phase space (those states which project onto the zone center of the interface plane) has been included in Eq. 2.1. The model developed as a part of this thesis is an extension of the model given by Eq. 2.1 in which all of the relevant band minima have been included. In addition, the electron transmittance between arbitrary materials has been derived and included in the model. This section first discusses the limitations and utility of the model, and then pursues the details. Finally, general expressions for the electron transmission are shown to reduce to the simple zone-centered expression found in introductory quantum mechanics textbooks.

The model presented below relies upon a single-band effective mass theory and the envelope wavefunction approximation [59] to calculate the quantum transmittance through a metal/semiconductor interface. The interface is assumed to be abrupt, and the metal is taken to be nearly free-electron, as has been the case for most other models of the BEES current [14, 25]. The boundary conditions that rely on matching envelope wavefunctions are valid only if the central cell portions of the total wavefunctions are identical. This is not the case for different materials. Furthermore, the interfaces considered here are typically not as abrupt as epitaxial semiconductor/semiconductor interfaces, where these approximations have been quite successful. Interdiffusion, possible passivation or contamination layers, and image charge effects all affect the width of the transition region between bulk metallic states and bulk semiconductor states. Finally, although there are clear similarities above the Fermi level $E_F$, the band structure and wavefunctions of Au deviate markedly from free-electron behavior. This is most apparent near the $\langle 111 \rangle$ directions, where there are regions with no propagating states.

Having listed the approximations, it is worthwhile to examine where the model is valid. First, the model employs the correct phase space for the semiconductor, and nearly so for the metal. It is the number of states available for transmission that plays the primary role in determining the BEES spectral shape. Second, and of most interest here, the calculated quantum transmittance has the correct form in both the low-energy and high-energy limits. Provided the energy of the incident electron is sufficiently far from a band extremum in the metal (so that the incident electron flux density may be considered constant over a small energy range), the transmittance near threshold will be proportional to the normal component of the group velocity in the collector, which itself varies as $E^{1/2}$ (i.e. $[V - V_b]^{1/2}$) at a band extremum. At high energies the transmittance must saturate to a constant value for a parabolic band. For real materials saturation may not be reached before the bands become non-parabolic, but even so, the energy dependence of the transmittance becomes substantially weaker at higher energies. These conclusions will not be dramatically affected by details of the metal/semiconductor transition region such as image potential lowering, so long as inelastic effects are negligible and the relative change in kinetic energy is large (for Au/Si this difference is on the order of 6.5 eV). Therefore, it is expected that an effective mass model will produce an accurate model for the transmittance through a simple metal/semiconductor interface. The validity of these assumptions will be evaluated using high-resolution experimental spectra in Chap. 3.

Using the assumptions stated above, the quantum transmittance can be calculated by assuming that the Schottky barrier forms a step potential with differing effective masses on either side. Under the single-band, time-independent effective mass approximation, the quantum transmittance of an abrupt potential barrier can be determined in closed form. Many textbooks derive this result for the zone-centered case [59], but omit non-zone-centered minima. The quantum transmittance with non-zone-centered band minima is needed to treat technologically important indirect band gap materials like silicon (as well as higher lying minima in gallium arsenide). In this work, the quantum mechanical transmittance and reflectance for an interface between two arbitrary material systems is developed and included in the semiclassical BEES model. The resulting expression applies to both zone-centered and non-zone-centered minima.

To derive the expression for transmittance, consider an electron in the base material incident upon an interface with the collector material. The incident electron wavevector in the base can be expressed as the sum of a "local" wavevector, $\mathbf{k}_i^\ell$, and $\mathbf{k}_B^0$, the wavevector which locates that band minimum in momentum space. The wavevectors of both the reflected and transmitted wavefunctions can be written similarly, although the band offset in the collector, $\mathbf{k}_C^0$, will generally be different than that in the base. To satisfy conservation

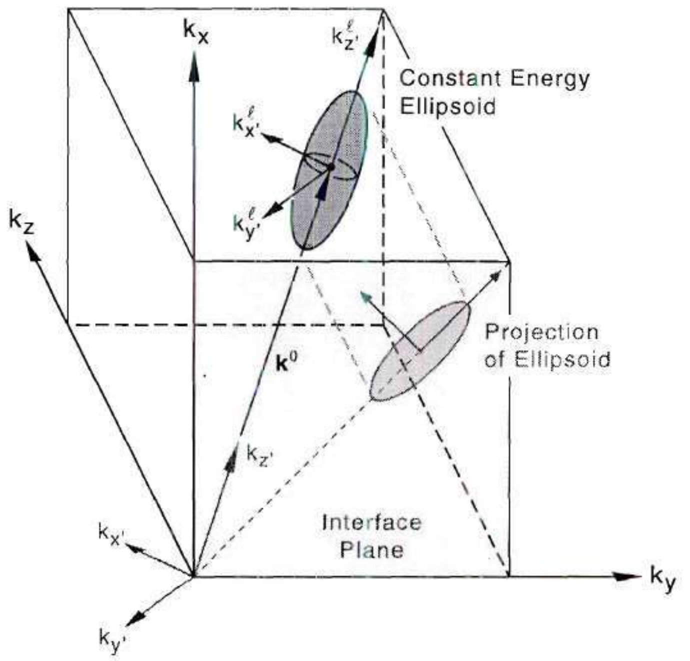

Figure 2.2: An ellipsoidal constant energy surface in momentum space. The ellipsoid has been rotated from the principal coordinate system $(k_{x'}, k_{y'}, k_{z'})$ into an interface coordinate system $(k_x, k_y, k_z)$ and projected onto the interface plane. The projection represents the allowable momentum states into which an electron can be transmitted.

of energy, only those wavevectors lying on ellipsoidal constant energy surfaces

$$E(\mathbf{k}^{\ell}) = E^0 + \frac{\hbar^2}{2}(\mathbf{k}^{\ell})\mathbf{M}^{-1}(\mathbf{k}^{\ell})^T \tag{2.5}$$

can be considered. Here $\mathbf{M}^{-1}$ is the inverse effective mass tensor for the material, T denotes vector transpose, and $E^0$ the energy of the relevant band minimum.

Conservation of momentum parallel to the interface plane ("phase matching") determines the set of wavevectors for which the electron can possibly be transmitted. As shown in Fig. 2.2, the projection of a constant energy surface $(k_{x'}, k_{y'}, k_{z'})$ onto the interface plane $(k_x, k_y, 0)$ determines all of the parallel wavevectors that are energetically allowed. The overlap of projections from the base and collector constant energy surfaces then gives the set of wavevectors that obey both conservation of energy and conservation of parallel momentum. To find the required projections and overlap, Eq. (2.5) (for both base and collector) is evaluated in the "interface coordinate system" defined by the interface normal, $\hat{\mathbf{z}}$, and a convenient choice of orthogonal $\hat{\mathbf{x}}$ and $\hat{\mathbf{y}}$ in the interface plane. The inverse effective mass tensor in the interface coordinate system is expressed in the principal axis system via a unitary transformation as

$$\mathbf{M}^{-1} = \mathbf{\Theta}\mathbf{M}_D^{-1}\mathbf{\Theta}^{\mathrm{T}}, \tag{2.6}$$

where $\mathbf{M}_D^{-1}$ is the principal axis (diagonal) representation of the tensor, and $\mathbf{\Theta}$ is the rotation matrix that transforms from principal axis coordinates to the interface coordinate system. For the usual case, the set of projected wavevectors in the base encompasses all of those in the collector, so that the overlap is simply determined by the projections of the collector constant energy surfaces.

Given the states for which electron transmission is allowed, the quantum transmittance may be calculated by applying the appropriate boundary conditions. However, modifications for the case of non-zone-centered band minima are necessary. For nondegenerate conduction band minima we define the envelope wavefunctions on the base ($B$) and collector ($C$) sides of the interface are defined as [60]

$$\begin{aligned} \psi_B &= \psi_B^{\ell}\psi_B^{0} = \left(e^{i\mathbf{k}_i^{\ell}\cdot\mathbf{r}} + re^{i\mathbf{k}_r^{\ell}\cdot\mathbf{r}}\right)\left(e^{i\mathbf{k}_B^{0}\cdot\mathbf{r}}\right), & (2.7) \\ \psi_C &= \psi_C^{\ell}\psi_C^{0} = \left(te^{i\mathbf{k}_t^{\ell}\cdot\mathbf{r}}\right)\left(e^{i\mathbf{k}_C^{0}\cdot\mathbf{r}}\right). & (2.8) \end{aligned}$$

The first boundary condition, continuity of the wavefunction amplitude at the interface, yields the phase matching conditions already applied and the relation $t = 1 + r$. For a zone-centered minimum, the second boundary condition commonly used is the continuity of $(1/m_z^*)\hat{\mathbf{z}}\cdot\nabla\psi$. For a non-zone-centered minimum it can be shown from $\mathbf{k}\cdot\mathbf{p}$ perturbation theory that the second boundary condition must be calculated using the wavevector relative to the band minimum, $\mathbf{k}^{\ell}$, since the group velocity is determined by $\mathbf{k}^{\ell}$ [61]. The second boundary condition may then be written for an arbitrary interface at $z = 0$ as

$$\hat{\mathbf{z}}\cdot\left(\mathbf{M}_B^{-1}\nabla\psi_B^{\ell}\right)\Big|_{z=0} = \hat{\mathbf{z}}\cdot\left(\mathbf{M}_C^{-1}\nabla\psi_C^{\ell}\right)\Big|_{z=0}, \tag{2.9}$$

where $\hat{\mathbf{z}}$ represents the unit vector normal to the interface. It is easily shown that this condition implies continuity of the average current. Defining $\alpha = \hat{\mathbf{z}} \cdot (\mathbf{M}_B^{-1}\mathbf{k}_i^{\ell})$ and $\gamma = \hat{\mathbf{z}} \cdot (\mathbf{M}_C^{-1}\mathbf{k}_t^{\ell})$, the complex reflection and transmission amplitude coefficients $r$ and $t$ are given by

$$\begin{aligned} r &= \frac{\alpha - \gamma}{\alpha + \gamma}, && (2.10) \\ t &= \frac{2\alpha}{\alpha + \gamma}. && (2.11) \end{aligned}$$

The transmittance and reflectance are the fractions of transmitted and reflected current,

$$\begin{aligned} T &= \frac{J_t}{J_i} = \frac{\gamma}{\alpha}|t|^2, && (2.12) \\ R &= -\frac{J_r}{J_i} = |r|^2. && (2.13) \end{aligned}$$

## 2.3 Electron Momentum Distribution

### 2.3.1 Background

Since the first experimental measurements on Si(111) were performed, the electron momentum distribution has also been the focus of considerable work and interest. Inspired by the ability of the model to reproduce accurately the shape of the experimental Au/Si(100) and Au/GaAs(100) spectra, the electrons collected by the semiconductor were originally believed to have travelled in a completely ballistic manner, meaning that both the carrier energy and momentum had retained their initial values. However, measurements made by Schowalter and Lee [58] on Au/Si(100) and Au/Si(111) provided the first evidence that the momentum distribution at the M/S interface is not forward peaked as had been assumed. In their measurements, the magnitudes of the experimental spectra, which should be significantly different, were comparable. To address this discrepancy between the theory and the measurement, elastic scattering was included in a Monte Carlo simulation of the BEES current. These simulations were used to determine that the magnitude of the current for

Au/Si(111) could be reproduced if a large amount of elastic scattering in the metal film was included. Garcia *et al.* [62] have also performed simulations of the electron transport in the metal using beam propagation methods and found that the band structure of the as-deposited Au(111) (which has disallowed momentum states along the (111) axes) may account for the observed magnitudes. Although these results have provided numerical insight into the evolution of the electron momentum distribution, the effect of elastic scattering in the base has not yet been incorporated into the more widely utilized semiclassical model given by Eq. (2.1).

### 2.3.2 Inclusion of Elastic Scattering

To complete the model, the effect of elastic scattering is included within the framework of the commonly used semiclassical model. For the near-threshold region, most inelastic scattering events will reduce the electron energy to a value below the Schottky barrier (preventing it from contributing to the collector current). Consequently, only the effect of elastic scattering on the distribution will be included here. This elastic scattering, which occurs in the metal base and at the M/S interface, affects the shape of electron momentum distribution incident on the M/S interface. The initial distribution, which is injected by the STM tip, is approximated by a forward peaked planar tunneling distribution. For this type of distribution, most of the incident carriers have a small component of momentum parallel to the interface plane (i.e. small angle of incidence). As the carriers travel through the film and arrive at the non-epitaxial interface, elastic scattering events randomize the carriers trajectories and redistribute the carriers into all available angles. The shape of this distribution alters the resulting BEES spectrum due to the constraint of conservation of parallel momentum across the interface. The scattering can result in either an increase or a decrease in the magnitude of the spectrum depending upon the details of the constant energy surface and details of the allowed wave vectors for transmission.

In the extended BEES model developed here, the elastic scattering is modeled by considering a fraction $s$ of the incident electrons to be scattered isotropically (in angle). The distribution incident on the interface is then a summation of a planar tunneling and an isotropic distribution that is given by

$$D_C(E, k_\parallel) = (1 - s)D_T(E - eV, k_\parallel) + sD_s(E, k_\parallel) \tag{2.14}$$

where $k_\parallel^2 = k_x^2 + k_y^2$ is the component of the incident wavevector parallel to the interface plane, $D_T(E, k_\parallel)$ is the planar tunneling distribution, $V$ is the magnitude of the tip-base potential difference, $-e$ is the electron charge, and $D_s(E, k_\parallel)$ is an isotropic distribution with an equal number of electrons at all angles of incidence $\theta_i$ where $\tan\theta_i = k_\parallel / k_z$. The isotropic distribution $D_s(E, k_\parallel)$ is determined by the requirement that the number of electrons is conserved in the scattering. This can be achieved by normalizing the volume of the distribution to that of the planar tunneling distribution as given by

$$D_s(E, k_\parallel) = \frac{2\pi}{|\mathbf{k}_i|^2 \sqrt{1 - k_\parallel^2 / |\mathbf{k}_i|^2}} \left( \int_0^{|\mathbf{k}_i|} k_\parallel D_T(E - eV, k_\parallel) dk_\parallel \right) \tag{2.15}$$

where $\mathbf{k}_i$ is the incident wavevector. Figure 2.3 shows the distribution for various values of $s$ ranging from planar tunneling ($s = 0$) to isotropic ($s = 1$). This paramaterization allows the distribution to be continuously varied from the forward-peaked planar tunneling distribution to one that has been completely randomized. This randomization, assumed to occur in the metal film and at the M/S interface, provides carriers with sufficient parallel momentum to phase match into non-zone-centered minima. Note that the parallel component of crystal momentum is still conserved at the interface. In this model, the electron scattering occurs *before* wavefunction matching.

## 2.4 The Model

A BEES model can now be formulated that includes elastic scattering and the quantum transmittance for zone-centered as well as non-zone-centered minima. For a single band

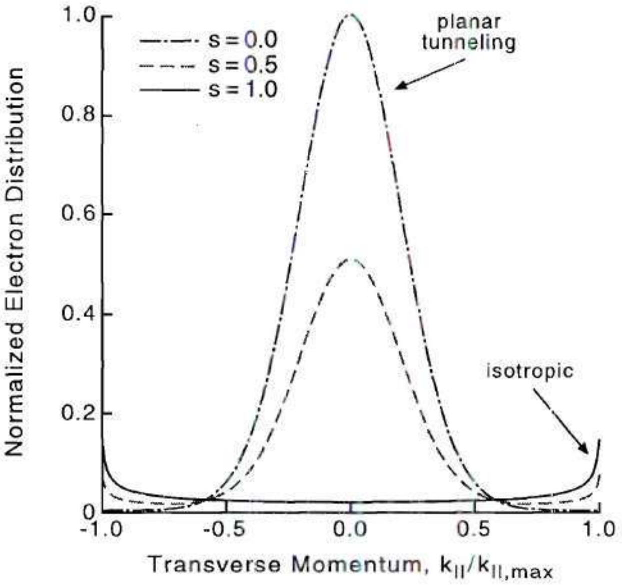

Figure 2.3: The electron distribution incident upon the base-semiconductor interface corresponding to various values of the scattering parameter $s$. The distribution was varied from a planar tunneling distribution, $s = 0.0$, to an isotropic distribution, $s = 1.0$, to account for elastic scattering in the base and at the interface.

minimum, the ratio of the collector current $I_C$ to tunnel current $I_T$ is given by

$$\left(\frac{I_C}{I_T}\right)_i = \mathcal{R}\,\frac{\int_{E_f+eV_b}^{\infty} f(E-eV)\int\int D_C(E,k_x,k_y)\,T(E,k_x,k_y)\,dk_y dk_x dE}{\int_{eV}^{\infty}[f(E-eV)-f(E)]\int\int D_T(E-eV,k_x,k_y)\,dk_y dk_x dE} \tag{2.16}$$

where $E$ is measured from the bottom of the conduction band in the base. $D_T$ is the planar tunneling distribution and $D_C$ the electron distribution incident on the collector. The quantum transmittance is denoted by $T$, $f(E)$ is the Fermi function, $V_b$ is the Schottky barrier, and $\mathcal{R}$ is an energy-independent scale factor accounting for attenuation in the base. The subscript $i$ labels the particular band minimum under consideration. To be correct, all of the relevant band minima must be calculated and summed. The limits of integration in $k_x, k_y$ are determined by the projections of the constant energy ellipsoids onto the interface plane as shown in Fig 2.2. In practice the injected tunneling current is held fixed by adjusting the tunneling gap. For computational simplicity, the ratio of the collector current to the tunnel current is calculated (as opposed to only $I_C$) to account for this variation in the tunnel gap as function of the applied bias.

The model defined by Eq. 2.16 will be referred to as the $T(E)$ model for brevity, even though the $k_x$, $k_y$ dependence of the quantum transmittance has been included in the calculations. In Chap. 3 the $T(E)$ model will be compared with a simplified model obtained by setting the transmittance to unity in Eq. 2.16, for all energies (above the Schottky barrier) and all angles (within the critical angle). This model, referred to as the $T = 1$ model, is different from the Bell-Kaiser model given in Eq. 2.1 because all of the band minima, not just the zone-centered minima, are included.

## 2.5 Discussion

The work presented in this chapter extends the scope the commonly used semiclassical Bell-Kaiser model by incorporating two of the important dynamical effects in the transmission process. These are elastic scattering in the base and at the M/S interface, and the quantum transmittance arising from the impedance mismatch for electron waves crossing the M/S interface. The required form of the quantum transmittance was determined for electron transmission through nondegenerate conduction-band states between arbitrary materials. The model was also extended to include all of the relevant band minima (allowed phase space) in the semiconductor collector. Previously, only the minima that project onto the zone center of the interface plane were included in the model. The approximations used to derive the model and the resulting limitations were discussed. The validity of these approximations and the regime where the model is expected to be accurate were assessed. The extended BEES model developed is referred to as simply the $T(E)$ model even though the angular dependence of the quantum transmittance has been included in the calculation.

The extensions to the model will allow a more detailed description of the BEES spectrum in the near-threshold region. By including both non-zone-centered as well zone-centered band minima, technologically important materials like silicon (and higher lying valleys in gallium arsenide) can be treated accurately. Inclusion of elastic scattering in the base via a scattering parameter $s$ allows for the modeling of the non-zone-centered minima which, given a forward-peaked planar tunneling momentum distribution, would not significantly contribute to the collected current. Achieving an accurate description of this low-energy regime is desirable because it allows for the investigation of very subtle effects such as phonon scattering that are not presently included in the model. The model developed is capable of providing a more complete description of the electron transport in BEES. To refine further the model, the practical effect of the added components must be evaluated via comparison with high-resolution experimental data.

# Chapter 3

# Single-Interface Measurements

## 3.1 Background

The limits of BEES as an analytical tool cannot be reached without a thorough understanding of the range of applicability of various models, and the relative magnitudes of elastic and inelastic scattering processes. The single-interface M/S structure forms the core of the BEES measurement technique and needs to be well understood and modeled if more complex structures, such as quantum devices, are to be successfully investigated and described. All other types of test structures are extensions of this in which either the metal or the semiconductor are altered to produce a more complex device. For example, to investigate carrier transport in magnetic multilayers [63–65], the single layer metal base is replaced with multiple layers of alternating magnetic/non-magnetic layers such as Au/Fe/Au/Fe/Au. To investigate carrier transport in semiconductor heterostructures (as in Chap. 4 and Chap. 5) the bulk semiconductor collector is replaced by multiple layers of a compound semiconductor such as a $Ga_{1-x}Al_xAs$ heterostructure [11, 50]. To understand measurements made on these structures, the simple M/S single-interface must be understood completely, especially in the near-threshold region. Accurate modeling of this low-energy regime should be the most feasible because of the absence of high-energy scattering events. In addition, for the purpose of characterizing quantum devices, it is the low-energy regime (generally much less than 0.5 $eV$ above threshold) that is of primary interest. Therefore, the approach taken in this thesis has been to implement first a ballistic model (see Chap. 2), and then to determine the energy range over which the model accurately describes the experimental spectra. The goal is to obtain a complete understanding of the near-threshold region of the basic M/S structure that will serve as a basis for analyzing more complex quantum semiconductor heterostructures. An accurate and consistent description of data taken on various material systems must be realized if small deviations (caused by subtle effects such as electron-wave interference) are to be detected.

To do this, extremely low-noise, high-resolution experimental data must be acquired and compared to the $T(E)$ model to determine its validity and limitations. Parameters of the extended model such as the elastic scattering factor $s$ need to be determined by comparing the model with these high-resolution spectra. Furthermore, the uncertainty over the inclusion of the quantum transmittance past the M/S interface must be resolved conclusively. Since the non-epitaxial nature of the interface is expected to obscure this effect, this controversy can only be resolved by obtaining very low-noise measurements at low-temperature.

To obtain such high precision measurements, BEES must be performed at low temperature for several reasons. First, noise fluctuations in the diode, caused by thermal excitations, are reduced. Since the BEES current (which is typically pA's) flows between the base and collector, this reduces the noise in the measured signal. Reducing the temperature also increases the energy resolution of the injected electrons due to the sharpening of the Fermi-Dirac distributions in the tip and base. The energy resolution is proportional to the width of the derivative of $f(E)$ which is $\sim 3.5\ k_B T$, where $k_B$ is Boltzmann's constant and $T$ is the absolute temperature. Thus an energy resolution of 23 meV (2.1 meV) can be achieved by performing the measurements at 77 K (7 K). Also at low temperature, extensive signal averaging can be incorporated into the measurement because the lateral drift of the STM tip is reduced significantly. At higher temperatures, the tip drifts across the sample surface and the spectrum becomes inhomogeneously broadened by any changes in the interface characteristics. If the tip drifts a large distance, the resulting spectrum will represent the *average*, rather than the *local* properties of the interface. Lastly, better signal-to-noise ratio performance is possible because the mean-free-path $\lambda_{\rm mfp}$ of the electron is increased due to a reduction in processes such as electron-electron, electron-ion, and electron-phonon scattering. This increase in $\lambda_{\rm mfp}$ increases the number of carriers that reach the collector which in turn increases the magnitude of the BEES current.

## 3.2 Experimental Apparatus and Sample Preparation

To meet thee requirements of low-temperature, high-resolution, low-noise, and small lateral tip drift, a BEES apparatus was constructed for operation down to temperatures as low as 6-7 K [66]. The inherent BEES energy resolution is expected to be 2.1 meV at 7 K, 23 meV at 77 K, 91 meV at 300 K, and the RMS noise level in some of the measurements presented here was as low as 1-2 fA. Also, because of the low lateral drift rate inherent in the STM design, the tip remained at the same position to within a few Å during acquisition of a spectrum. This is an important aspect of the measurements, since small shifts in the threshold voltage from one spatial position to another would otherwise degrade the resolution. Au/Si(100) and Au/Si(111) diodes were phosphorus doped 1x$10^{15}$ cm$^{-3}$ and 1x$10^{16}$ cm$^{-3}$, respectively, and were prepared for evaporation by cleaning in trichloroethylene, acetone, and dehydrated ethanol followed by etching in a 10:1 ethanol:HF solution for 90 sec. GaAs samples consisted of a 1 $\mu m$ thick layer of $n$-type (Si-doped, $1 \times 10^{15}$ cm$^{-3}$) grown by MBE on a degenerate $n$-GaAs substrate. Wafers were capped with arsenic before removal from the growth chamber. Before diode preparation, the arsenic cap was removed by electron-beam heating to 400° C in vacuum. The sample was cooled and removed from the vacuum, then passivated in $NH_4(OH)$ for 30 sec [67] followed by a 30 sec rinse in DI water. Finally, the wafers were blown dry using nitrogen gas. A 7 nm thick gold base layer was deposited at room temperature by electron-beam evaporation for the Si devices and by thermal evaporation for the GaAs devices. For both cases, the background pressure was $\approx 5 \times 10^{-7}$ *torr*. All Si experimental data were taken at $T = 77$ K in order to avoid spectral distortions caused by the large bulk resistivity at lower temperatures [68]. The 77 K spectra were smoothed using a 10-point Gaussian with a FWHM of 7.5 meV to reduce digital noise. All GaAs experimental data were taken at 7 K. In this case the spectra were not smoothed, since the energy resolution at this temperature is smaller than the voltage step used (2.5 mV) for data acquisition. Spectra were acquired at a number of locations on each of several diodes for each interface system.

## 3.3 Elastic Scattering

Without the inclusion of some form of scattering, ballistic models cannot accurately predict the observed magnitude of the Au/Si(111) BEES spectrum. In the present work, the effect of elastic scattering in the base and at the M/S interface is modeled by altering the distribution incident upon the base-semiconductor interface, as given by Eq. (2.14) and shown in Fig. 2.3. Due to the scattering, this distribution is different from the injected distribution and is represented by the sum of a planar tunneling and an isotropic (in angle) momentum distribution. In what follows, the effect of elastic scattering on the predicted spectra in light of the available states in the semiconductor is discussed first. Subsequently the model is compared to experimental data in order to determine the value of the scattering parameter $s$ in Eq. (2.14).

As discussed in Chap. 2, the overall shape of the BEES spectrum for a simple Schottky interface is largely determined by the number of states available for transmission into the semiconductor. If the component of the electron momentum parallel to the interface, denoted $k_{\|}$, is assumed to be constant in the transport process (phase matching), then the states available for transmission can be represented by projecting the constant energy surfaces in momentum space onto the plane corresponding to the orientation of the semiconductor collector. The constant energy surfaces are derived from

$$E = \hbar^2 k_t^2/2m_t^* + \hbar^2 k_{\|}^2/2m_{\|}^* \tag{3.1}$$

where $k_t$ is the component of the momentum perpendicular to the interface, and for parabolic bands are ellipsoidal due to the anisotropy of the effective mass. For ellipsoids that project onto the origin of the interface plane (zone-centered), these projections represent a critical angle beyond which carriers cannot be transmitted. For ellipsoids that do not project onto the origin of the interface plane (non-zone-centered), these projections represent a critical annulus outside of which carriers cannot be transmitted. Due to the sensitivity of the spectrum to changes in the allowed interface wavevectors (projected states), different crystallographic orientations, which correspond to different interface planes and projected areas, should result in experimentally measurable differences in the magnitude and shape of the BEES current.

This effect was first investigated by Schowalter *et al.* [25, 57, 58] who reported a discrepancy between the magnitude of the measured and the predicted BEES current on Au/Si(111). Silicon is an indirect band gap material in which the band minima lie in the $X$-direction approximately 80% of the way to the edge of the first Brillouin zone. The constant energy ellipsoids and corresponding allowed set of interface wavevectors for Si(100) and Si(111) are drawn in Fig. 3.1 and Fig. 3.2, respectively. For transmission into Si(100), carriers with both small and large $k_{\|}$ (incident angle) can phase match into states in the semiconductor. However, for transmission into Si(111), only carriers with a large $k_{\|}$ are transmitted. Thus, the measured collector current in Si(111) devices should be much smaller than the measured current in Si(100) devices because the planar tunneling distribution used to describe transport between the tip and base is forward peaked in momentum (small $k_{\|}$). Simulations of the BEES current for an Au/Si(111) device, the most sensitive orientation, for various amounts of scattering are shown in Fig. 3.3. As the momentum distribution is varied from planar tunneling ($s = 0.0$) to isotropic ($s = 1.0$), the magnitude of the current

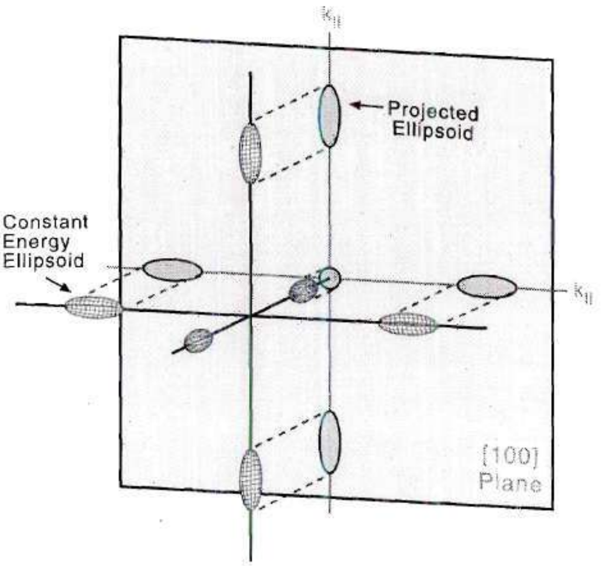

Figure 3.1: Constant energy ellipsoids and corresponding allowed set of interface wavevectors for Si(100) calculated by projecting the constant energy surface onto the (100) interface plane. For Si(100), electrons with both large and small transverse momenta $k_{\|}$ are transmitted.

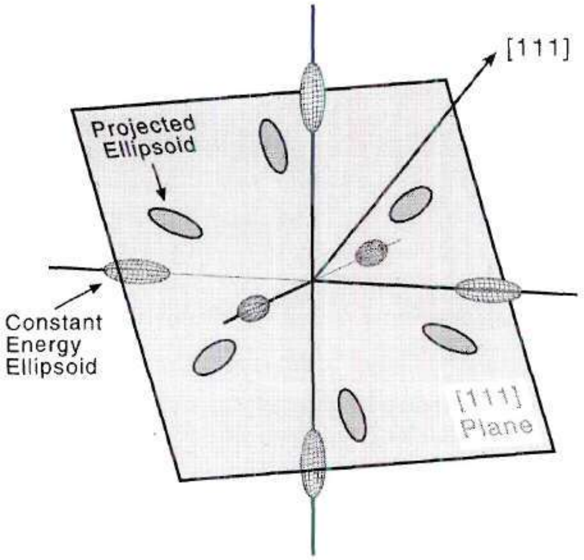

Figure 3.2: Constant energy ellipsoids and corresponding allowed set of interface wavevectors for Si(111) calculated by projecting the constant energy surface onto the (100) interface plane. For Si(111), an electron must have a large transverse momentum $k_{\|}$ to phase match, implying a large angle of incidence.

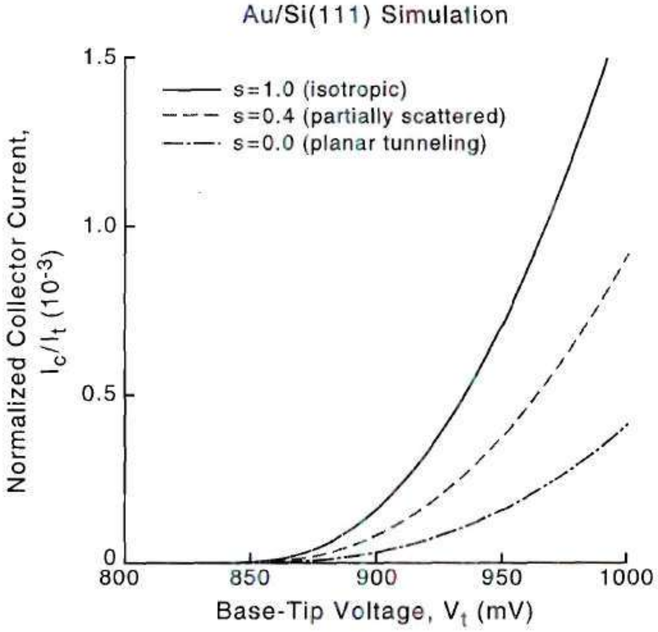

Figure 3.3: Simulation of BEES current for an Au/Si(111) diode for various amounts of elastic scattering. As the scattering increases, more electrons can phase match and the magnitude increases.

changes by a factor of 10. For the planar tunneling distribution, relatively few of the injected carriers have sufficient $k_\parallel$ to phase match and be transmitted into the Si(111) collector. As the distribution is broadened by scattering events, carriers with sufficient $k_\parallel$ are generated and the magnitude of the current quickly increases.

In addition to the difference in magnitude of the spectrum, the inclusion of elastic scattering will also affect the shape spectrum. Simulations calculated for Si(100), Si(111), and GaAs(100) (which has allowed wavevectors for small $k_\parallel$ *only*) show that this variation is small compared to the changes in magnitude, but are the most significant for Si(111). The majority of the change in shape of the Si(111) spectrum occurs when only a small amount of scattering is included ($s = 0.3$). This perturbation quickly drives the shape toward that of isotropic scattering.

Experimentally, the effect of varying the incident distribution can be seen in the

| | $s$ | 0.0 | 0.2 | 0.4 | 0.6 | 0.8 | 1.0 |
|---|---|---|---|---|---|---|---|
| Si(111) | $\mathcal{R}$ | 7.871 | 4.836 | 3.481 | 2.717 | 2.227 | 1.887 |
| | $\sigma^2$ | 3.723 | 1.927 | 1.521 | 1.383 | 1.327 | 1.302 |
| Si(100) | $\mathcal{R}$ | 0.533 | 0.586 | 0.651 | 0.733 | 0.835 | 0.972 |
| | $\sigma^2$ | 8.776 | 7.170 | 5.855 | 4.203 | 3.479 | 3.518 |
| GaAs(100) | $\mathcal{R}$ | 0.028 | 0.036 | 0.047 | 0.070 | 0.135 | 1.806 |
| | $\sigma^2$ | 0.659 | 0.659 | 0.658 | 0.659 | 0.658 | 0.652 |

Table 3.1: Experimental results of fitting simulations with various values of $s$ to Au/Si(111), Au/Si(100), and Au/GaAs(100) spectra. The mean-squared-error, $\sigma^2(\text{x}10^{-5}\text{pA}^2)$, indicates the quality of the fit with respect to the shape, and $\mathcal{R}$ an energy independent scale factor, indicates the magnitude of the simulation with respect to the experimental spectra. $\mathcal{R} > 1$ is non-physical.

quality of the model fits to experimental data as determined by the mean-squared-error, $\sigma^2$, and to a lesser extent the value of the scale factor, $\mathcal{R}$. A value of $\mathcal{R} > 1$ indicates that the experimental spectrum has a greater magnitude than the simulation. Table 3.1 summarizes the results of fitting the experimental spectra to simulations employing various values of $s$ that correspond to varying the distribution from planar tunneling to completely isotropic.

For Au/Si(111), Table 3.1 shows that as more elastic scattering is introduced, the goodness of the fits to the simulations improves ($\sigma^2$ decreases). This indicates that a substantial amount of scattering is required to obtain the correct spectral shape. From the behavior of $\sigma^2$ it appears that $s \geq 0.5$. Note that the value of $\mathcal{R}$ remains greater than 1 for all $s$. This would seem to be non-physical since inelastic scattering should always reduce the current. Recent measurements of a 100 nm inelastic mean free path in Au [69] may provide an explanation, however. For the 7 nm thick films employed in this work, one would expect to get multiple reflections from the metal/vacuum interface, thus each electron may have several opportunities to be transmitted. This phenomenon has been investigated in detail by Bell [70] who found that as the thickness of the Au base was increased, the shape of the Si(111) spectrum changed whereas the shape of the Si(100) shape remained relatively constant. These measurements also showed that the rates of change in the magnitude of the current (as the thickness of the Au was increased) were different. These results revealed that the effect of multiple reflections is important, especially when the base thickness is less than 10 nm, as it is in all of the spectra taken in this thesis.

Another possible explanation is related to the assumption that the Au base is free-electron like. The band structure of Au has "necks" of non-propagating states in the $\langle 111 \rangle$ directions, which are also the preferred growth directions in the absence of any epitaxial relationship (due to close-packing). This would imply that the initial distribution is not forward peaked as assumed for the ordinary planar tunneling case. Instead, the incident distribution may have no electrons at normal incidence (in the $\langle 111 \rangle$ direction), thus more of the weight of the distribution would be at large angles, where Si(111) has allowed wavevector states [55]. As a result, the collector current would be somewhat higher than for tunneling into a free-electron metal. Although this scenario seems unlikely to account for the full discrepancy in $\mathcal{R}$, Andres *et al.* [62] have performed beam propagation calculations that show this explanation may not be completely implausible. However, multiple reflections appear to be the most likely explanation, although interband coupling would also contribute to larger $\mathcal{R}$ values.

For Au/Si(100), Table 3.1 shows that a nearly isotropic distribution minimizes the error and provides the correct shape. For this case as for Au/Si(111), the values of $\sigma^2$ appear to stabilize for $s \geq 0.5$. The magnitude of $\mathcal{R}$ is again quite large for large $s$ (where the spectral shape is best reproduced) and we once more speculate that multiple reflections from the metal/vacuum interface may be the reason.

For Au/GaAs(100), $\mathcal{R}$ becomes extremely small for simulations with a planar tunneling distribution, and begins to obtain more realistic values for $s > 0.8$. The error in the fit remains constant as $s$ is increased, indicating again that the Au/GaAs(100) simulation shape is unaffected by the amount of scattering. Because the shape does not change with $s$, it is difficult to determine much about the level of elastic scattering for this system. In this case it should also be pointed out that the passivation layer may reduce the value of $\mathcal{R}$.

## 3.4 Quantum Transmittance

The calculation of the transmittance/reflectance of an electron-wave past a potential step is one of the simplest and most fundamental examples of the laws of quantum mechanics and of the wave-like nature of electrons. The calculation is straightforward and leads to an elegant result that is exactly analogous to the Fresnel equations that govern transmission/reflection of light in general dielectrics [3]. Measuring this effect for a single-interface as shown in Fig. 3.4a is significantly more difficult to achieve. The transmittance as a function of the injected energy for this structure is shown in Fig. 3.4b. Conceptually, the collection of electrons in BEES performs this experiment exactly. In this configuration, the electrons are injected by the tip, travel through the thin metal film, and arrive at the interface between metal and the semiconductor. If this interface is assumed to be abrupt and the conduction band in the semiconductor is assume to be flat, the BEES configuration exactly matches that of the ideal schematic as shown in Fig. 3.4c. Realistically, the band is not flat (due to depletion and image potential lowering), the interface is not abrupt, and finally the maximum of the barrier is shifted inside the semiconductor. Shown in Fig. 3.4 are the actual and step approximation for the conduction band edge of the semiconductor in an Au/GaAs(100) Schottky diode at $T = 77$ K. Fortunately, as illustrated Fig. 3.4d, because the potential difference between the metal and semiconductor is large ($\sim 6.5$ eV) and because the shape of the band varies slowly near the potential maximum (which prevents carriers from tunneling through the barrier), the structure can be approximated reasonably well by a step potential thus allowing a measurement of the transmittance for this structure.

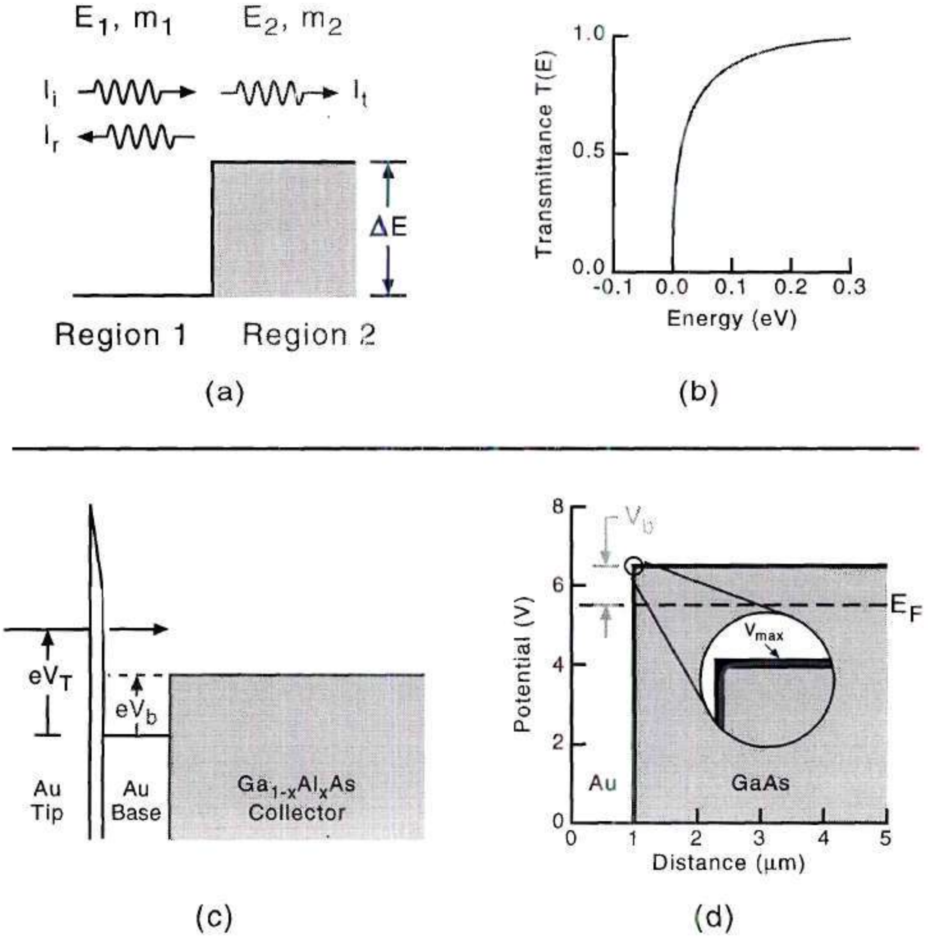

Figure 3.4: Analogy between the electron-wave transmission past an ideal potential step and the BEES experimental configuration. (a) A schematic diagram of an electron-wave incident upon an ideal potential step. (b) The transmittance as a function of the incident energy for this structure. (c) An band diagram of the BEES experimental configuration. (d) The actual and step approximation for the conduction band edge of the semiconductor in a M/S device.

Even given these similarities, using BEES to measure the transmittance of this structure is difficult because the BEES current resulting from electron transmission over the Schottky barrier is summed over all incident angles and all injected energies. Thus, the additional influence of the energy-dependent quantum transmittance of a single-interface on the shape of the spectrum is quite subtle. The second derivative of the spectrum cannot be used to provide directly the shape of $T(E)$ because of the lack of features inherent in the transmittance function for this fundamental structure. Therefore, in order to reveal the effect, two models [$T = 1$ and $T(E)$; see Chap. 2] were fit to the experimental data using a nonlinear-least-square fitting procedure. By determining which model best describes the data, the effect of the transmission process should be either confirmed or denied conclusively. For completeness, the analysis will be carried out on several materials systems including Au/Si(100), Au/Si(111), and Au/GaAs(100).

Previously, a model including quantum transmittance and a planar tunneling distribution for the zone-centered band minima of Si(100) was shown to provide a better description of measured spectra than the original BEES model [68], which also assumed unity transmittance. The following analysis uses simulations calculated with all relevant band minima and an *isotropic* ($s = 1.0$) distribution for both the $T = 1$ and $T(E)$ models. An isotropic distribution has been used because it more accurately reproduces the experimental data as determined in the previous section. For fitting to a single threshold spectrum, the nonlinear-least-square fits require two free parameters, the barrier height $V_b$ and the energy-independent scale factor $\mathcal{R}$. The fit is performed over a portion of the acquired spectrum that begins well below threshold and extends to an upper fit voltage $V_{fit}$.

Shown in Fig. 3.5 and Fig. 3.6 are typical experimental spectra for Au/Si(100) ($T = 77$ K) and Au/GaAs(100) ($T = 7$ K), respectively. The spectra are the result of signal averaging for a total of approximately 30 min. Averaging is performed for each applied voltage (4000 samples/voltage) and over the entire spectrum (15 spectra averaged/resulting

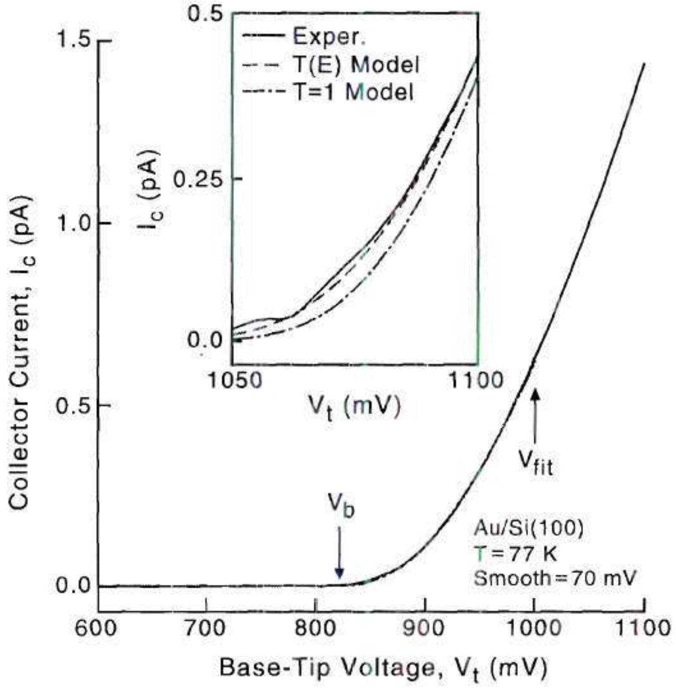

Figure 3.5: An experimental Au/Si(100) spectrum fit to both the $T(E)$ and $T = 1$ models. Although both models appear to fit, the inset shows the threshold region where the $T(E)$ model provides a better description than the $T = 1$ model.

spectra). The data taken on the Si(100) substrate were smoothed using a 10-point Gaussian with a FWHM of 7.5 meV to reduce digital noise. The spectra taken on GaAs are raw data and were not smoothed because the energy resolution at this temperature is smaller than the voltage step used (2.5 mV) for data acquisition. The root-mean-square noise levels in these measurements are on the order of a few fA's.

For each material system, the spectra have been fit to both the $T(E)$ and the $T = 1$ model up to an upper fit voltage $V_{fit}$. These plots show that for large voltage ranges, both models appear to provide a good description of the data. However, these models behave differently in the threshold region where a ballistic model is most valid. In addition, the threshold region is also where the energy dependence of the transmittance, which saturates at higher voltages, should be the most prominent. To illuminate the differences in the

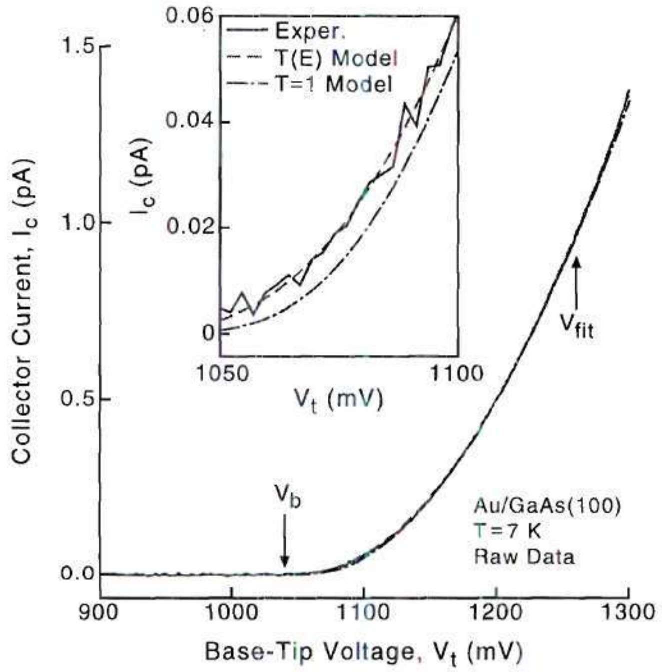

Figure 3.6: An experimental Au/GaAs(100) spectrum fit to both the $T(E)$ and $T = 1$ models. Although both models appear to fit, the inset shows the threshold region where the $T(E)$ model clearly provides a better description than the $T = 1$ model.

ability of the models to describe the date, 50 $mV$ regions just above threshold are shown in the insets of Fig. 3.5 and Fig. 3.6. In this region $T(E)$ model provides a noticeably better fit than the $T = 1$ model. This behavior is consistent for both the Au/Si(100) and Au/GaAs(100) spectra shown, as well as for the Au/Si(111) spectra not shown. The result was reproduced at several spatial locations on multiple samples from each material system confirming conclusively that the effect of the single-interface $T(E)$ is detectable using BEES and the appropriate modeling.

## 3.5 Model Stability and Range of Validity

The results of the previous section show that the $T(E)$ model provides a better description of the data for the fit range (choice of upper fit voltage $V_fit$) shown in Fig. 3.5 and Fig. 3.6.

However, anytime fitting parameters are used to draw conclusions about experimental data, the sensitivity of these results to changes in the fit parameters must be thoroughly investigated and understood. The possibility exists that the conclusions only hold for a small range of values which can be accessed by passing the correct initial conditions to the fitting algorithm. To address this, all of the parameter space that is relative to a particular problem must be considered. Once the entire space has been explored, the range of validity for the model being used to describe the data (and its assumptions) can be assessed.

In fitting various models to the experimental BEES spectra, the main point of contention is the fit range over which the model is fit. The resulting value of both fitting parameters, the barrier height $V_b$ and the scale factor $\mathcal{R}$, will depend on what portion of the data is used to fit to the model. Obviously the data range used to perform the fit must include enough of the data to obtain an accurate fit, but should not be so large that it violates any assumptions made in deriving the model. The quality of the fit for different fit ranges can, as described earlier, be assessed quantitatively by computing the mean-square-error $\chi^2$ between data and the resulting simulation. The fitting ranges over which $\chi^2$ is small and stable represents the voltage range over which the model (and its assumptions) provide a valid description of the data. In conjunction, the behavior of the fitting parameters should also remain stable over same fit ranges. However, if $\chi^2$ remains small and the fit parameters fluctuate radically, it is unlikely that the model is accurate and conclusions based on the fit are questionable.

To illustrate that the $T(E)$ model provides a correct description of the of the spectral shape and to evaluate its range of validity, a plot of the error of the fit versus fit range was calculated. This is determined by evaluating the mean-squared-error between the data and the simulation for many different fitting ranges. The lower voltage is fixed well below the threshold, and the upper fit voltage $V_{fit}$ is varied. For each fitting range, the two fit parameters $V_b$ and $\mathcal{R}$ were also recorded. The error vs. fit range and barrier height vs. fit range plots for Au/GaAs(100) is shown in Fig. 3.7. The plot shows that, over the threshold

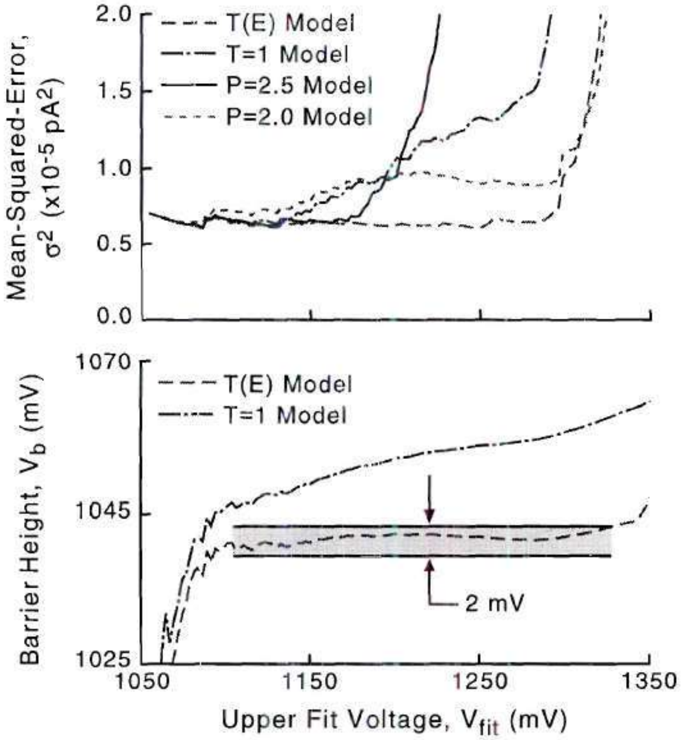

Figure 3.7: (a) The mean squared error between the experimental spectrum and the simulations is plotted as a function of the upper fit voltage, $V_{fit}$. The $T(E)$ model provides an accurate description of the data over a range of $\approx 250$ mV above threshold whereas the $T = 1$ model becomes inaccurate $\approx 100$ mV above threshold. Shown for comparison are the $P = 2.0$ and $P = 2.5$ thermally broadened power laws. (b) The barrier height as a function of upper fit voltage. The barrier height for the $T(E)$ model varies by less than 2 mV and the $T = 1$ model varies by more than 10 mV over the threshold region.

region, the $T(E)$ model accurately (small $\chi^2$) and stably (small fluctuations in $\chi^2$) describes the data over a large voltage range. The plots also show that the $T = 1$ model, which neglects the energy dependence of the transmittance, does not accurately describe the data, and fits more poorly ($\chi^2$ increases) as the fit range is increased. The range of validity for Au/GaAs(100) can be determined from this plot. For this material system, the $T(E)$ model is accurate up to approximately 250 $mV$ above threshold. This covers almost the entire energy range up to the next band minima at the L points. At the higher voltages, the current begins to increase quickly due to new transport channels that open as carriers begin to be transmitted into the L states. Since the model only contains a single minima, (Γ), the model is not valid past this point. Similar plots were also made for the spectra taken on Au/Si(100) and Au/Si(111) [71]. For both material systems, the results were the same as those on Au/GaAs(100). The range of validity of the model for Au/Si(100) and Au/Si(111) were 150 mV and 100 mV, respectively. Interestingly, the spectra taken on GaAs(100), which has the simplest band structure, were well described by the $T(E)$ model over the largest range of voltages whereas the spectra taken on Si(111), which has the most most complicated band structure, were well described over the small range of voltages.

To evaluate the power law approximations that are valid at cryogenic temperatures (sec Chap. 2), Figure 3.7 also shows the error vs. fit range for thermally broadened $P = 2$ square law and $P = 5/2$ power law. The power laws are thermally broadened to account for the effect of the finite temperature on the Fermi statistics in the tip and base. Both power laws accurately describe the data just above threshold as predicted, but the 5/2 power law fits better over a larger range than the square law. This indicates that the approximation of the quantum transmittance by a $\sqrt{E}$ dependence (for low energy electrons) is valid over the range indicated by Fig. 3.7. Still, the more complete the $T(E)$ model – which goes beyond the simple $\sqrt{E}$ approximation to the transmission function and includes transmittance at all angles – always produces the best fit. The stability of the $T(E)$ (and the 5/2 power law) model fits clearly demonstrate that the energy dependence of the electron transmission is well described by this semiclassical model over a substantial range of tip voltages (injected energies).

Finally, the effect of an energy-dependent mass was incorporated into the $T(E)$ model. The energy-dependent mass was assumed to follow the relation

$$m^*(E) = m_0^*(1 + \alpha E) \tag{3.2}$$

where $m_0^*$ is the value of the effective mass at the conduction band minimum and $\alpha = 0.5$ $eV^{-1}$ is the mass non-parabolicity factor [72]. The value of $\alpha$ typically used is an average

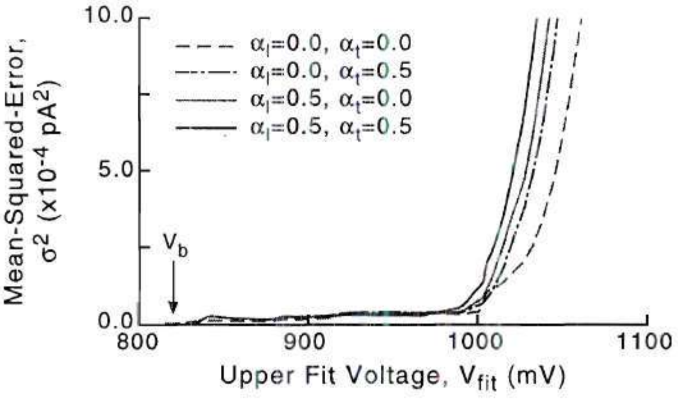

Figure 3.8: The effect of an energy-dependent effective-mass was investigated by fitting the data with simulations calculated using different combinations of non-parabolicity factors, $\alpha_\ell$ and $\alpha_t$. All of the simulations provide a similar description of the data over approximately the same range indicating that the effect of an energy-dependent mass within the threshold region is very small.

density of states value and does not directly describe the energy dependence for ballistic carriers. To account for this and to provide a bound on the magnitude of the effect on the simulation, all permutations of the longitudinal and transverse non-parabolicity factors, $\alpha_\ell$ and $\alpha_t$, with values 0.0 and 0.5 were investigated. The results are presented in Fig. 3.8 where the error vs. fit range for each combination of parameters is plotted. All of the simulations were calculated using the $T(E)$ model, an isotropic electron distribution ($s = 1.0$), and were fit to the BEES spectra taken on Au/Si(100) at 77 K. It is clear from Fig. 3.8 that the effect of an energy-dependent mass within the threshold region is very small. All of the simulations provide a good description of the data over approximately the same range. From this it is concluded that the eventual failure of the model at higher energies is not due exclusively to the non-parabolicity of the conduction band.

## 3.6 Discussion

The work presented in this chapter takes the first step toward obtaining an accurate description of electron transport in quantum semiconductor structures. High-resolution low-noise experimental spectra were obtained on Au/Si(100), Au/Si(111), and Au/GaAs(100) devices at 77 K and 7 K. These spectra were compared to the model developed in Chap. 2 to determine the elastic scattering parameter $s$, the necessity of including an energy-dependent quantum transmittance, and the range of validity of the $T(E)$ model, the $T = 1$ model, and approximate (valid at cryogenic temperatures) power law models. The scattering parameter was determined by utilizing the differences in the projected band structure onto the interface plane of Si(100) and Si(111). In order to reproduce both the shape and magnitude of the Si(111) spectrum, a nearly isotropic (in angle) momentum distribution is required. The necessity of including an energy-dependent transmittance was determined by fitting spectra from all three material systems with both the $T(E)$ and $T = 1$ models. While both models appear to provide similar descriptions of the data over a large voltage range, detailed analysis of the near-threshold region showed conclusively that the $T(E)$ provides a better description of the data. Furthermore, by exploring the parameter space of the fitting routine, the stability of all of the models was evaluated.

The results have refined the model developed and have shown its ability to completely describes the near-threshold region of the experimental spectrum of several different material systems. The results provide a baseline by which other effects can be investigated. Since all BEES test structures contain a M/S interface, the detailed description of this simple structure provides a standard by which more complicated structures can and should be compared. The results show that a complete description of this low energy regime is obtainable. In the following chapter, the experimental measurements will be expanded to include a basic heterostructure that consists of a single $\mathrm{Ga}_{1-x}\mathrm{Al}_x\mathrm{As}$ barrier. The model will be expanded to include the quantum transmittance through the entire structure and will be compared to high resolution spectra in an attempt to further optimize the model. Hopefully this incremental approach will provide a detailed description of this more complicated device that equals the description achieved on the M/S structure.

# Chapter 4

# Multiple-Interface Measurements

With an accurate description of the threshold region of the basic M/S interface, measurements on much more complicated and interesting devices can be attempted. To make the transition from studying the M/S interfaces to studying $Ga_{1-x}Al_xAs$ heterostructures, the simplest heterostructure possible, a single-barrier device, has been investigated. This device represents the next logical step in complexity and builds on the measurements obtained and modeled for the Au/GaAs(100) interface. As noted in Chap. 3, of the three interface systems studied, GaAs has the simplest band structure (a single zone-centered minimum, $\Gamma$) and was described by the semiclassical model up to the next higher lying minima (L). Although the single-barrier structure is still quite simple compared to actual quantum devices, a complete and thorough understanding of the electron transport in this structure is still needed. The understanding gained by analyzing this more simple structure will be key in understanding the transport in the electron-wave Fabry-Perot filters discussed later in Chap. 5.

## 4.1 Modeling of the Single-Barrier Structure

To study the carrier transport of semiconductor heterostructures with BEES, the bulk semiconductor collector is replaced with a buried nanostructure as illustrated in Fig. 1.4. For the single-barrier structure investigated in this chapter, this buried nanostructure is simply a 20 nm thick layer of $Ga_{0.8}Al_{0.2}As$. A schematic of the molecular beam epitaxy (MBE)

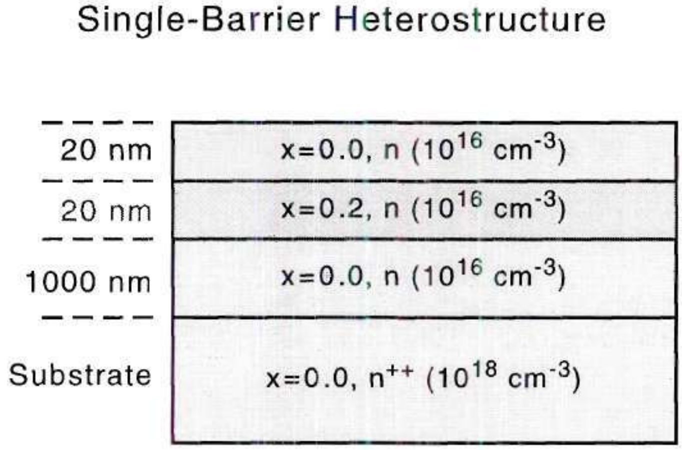

Figure 4.1: A schematic of the MBE grown $Ga_{0.8}Al_{0.2}As$ single-barrier heterostructure. The thickness of the $Ga_{0.8}Al_{0.2}As$ barrier region was designed to be large enough to prevent electrons from tunneling so that the shift in the threshold of the BEES spectra corresponds to the band offset of the material. Reduced n-type doping of the device reduces the band bending near the semicoundctor surface and eliminates tunneling through the top of the Schottky barrier.

grown $Ga_{0.8}Al_{0.2}As$ single-barrier heterostructure is shown in Fig. 4.1. The thickness of the $Ga_{0.8}Al_{0.2}As$ layer (20 nm) was designed to be large enough to prevent electrons with an energy below the conduction band minimum of the $Ga_{0.8}Al_{0.2}As$ from tunneling through the barrier region and contributing to the collector current. In this configuration, the threshold in energy of the BEES current to the location of the conduction band minimum of the barrier. Thus, the conduction band offset of the layer can be determined with high precision by measuring the shift in the BEES threshold between a reference Au/GaAs structure and the single barrier structure. In addition, to reduce the band bending near the semiconductor surface and eliminate tunneling through the top of the Schottky barrier, the doping of the device is n-type Si with a concentration between $10^{15}$ $cm^{-1}$ and $10^{16}$ $cm^{-1}$. The low-doped layers are grown on a conducting substrate with a doping of $10^{18}$ $cm^{-1}$. To remove the injected carriers from the substrate, an ohmic contact is formed using indium solder.

Due to the thick nature of the $Ga_{0.8}Al_{0.2}As$ barrier, previous measurements on sim-

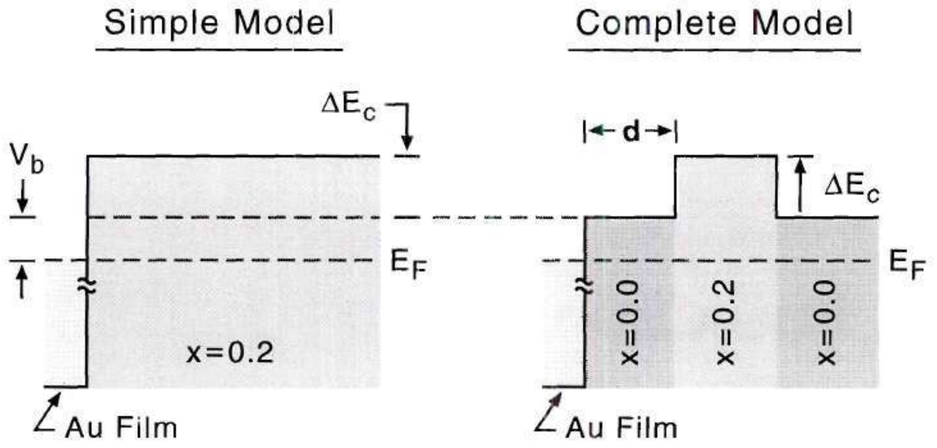

Figure 4.2: Band diagrams for the two models used to describe electron transport in the single-barrier heterostructure. The simple model approximates the structure as a simple single-interface of Au/$Ga_{0.8}Al_{0.2}As$ because only electrons with an energy above the barrier are transmitted. To be more correct, the complete model takes into account the transmission/reflection of all of the buried interfaces.

ilar structures [22] have ignored the reflection/transmission of the individual layers and approximated the structure as a simple Au/$Ga_{1-x}Al_xAs$ single-interface device. The band diagram for this simple model is shown in Fig. 4.2a. Alternatively, a more complete description of the structure must take into account the effect of the buried interfaces on the transmission probability [45]. The band diagram for the complete model is shown in Fig. 4.2b. In this model, a new unknown quantity, the thickness of the input region $d$ is introduced. The exact value of $d$ is not known because the surface passivation etches away an unknown amount of the GaAs input region, the conduction band is not completely flat and the interfaces are not ideally abrupt. Thus, to be more precise, $d$ represents the phase lag incurred by the electron-wave rather than the physical distance traveled.

With the addition of these buried layers in the complete model, electrons that arrive at the M/S interface with sufficient energy to pass over the Schottky barrier (formed by the Au/GaAs interface) are subject to the transmission probability of the *entire* structure (M/S interface + heterostructure). To account for this effect in the BEES model [see

Eq. (2.16)], the transmittance of the multilayer structure is calculated using a chain matrix approach [4]. In order to utilize this approach, several approximations have been made. First, the conduction band edge near the M/S interface is assumed to be flat because the thickness of the structures under consideration is small ($\sim$ nm's) compared to the thickness of the depletion width ($\sim$ $\mu$m's) and because the device is placed within a few nm's of the semiconductor surface. Similarly, the interfaces between adjacent $\mathrm{Ga}_{1-x}\mathrm{Al}_x\mathrm{As}$ layers are assumed to be abrupt and ideal. Second, the input region (typically gold) and the output region (typically GaAs) are assumed to be infinite in extent. For the output region, this approximation is valid because the thickness of the substrate is on the order of 500 $\mu$m's. However, the thickness of the input region is on the order of 5 nm's, a thickness which can support electron-wave resonances. Fortunately, since the effective mass of the electrons in the metal layer is close to unity, the magnitude of these resonances are greatly reduced at energies relevant to these measurements. Finally, as in the simple M/S structure, the image potential lowering is neglected due to its relatively small magnitude compared to the change in potential energy between the metal and the semiconductor as shown in Fig. 3.4. These simplifications make the treatment of the structures within the framework of the semiclassical model straightforward and allow for the inclusion of the transmittance/reflection past all of the relevant interfaces.

## 4.2 Determination of the Conduction Band Offset

The first step in analyzing the single-barrier structure is to determine experimentally the conduction band offset $\Delta E_c$ of the $\mathrm{Ga}_{0.8}\mathrm{Al}_{0.2}\mathrm{As}$ layer used to form the barrier. Since the threshold of the spectra taken on this structure should be shifted by exactly $\Delta E_c$, the offset can be determined by measuring the difference between the average barrier height on a separate Au/GaAs sample and the average barrier height on the Au/GaAs/$\mathrm{Ga}_{0.8}\mathrm{Al}_{0.2}\mathrm{As}$/GaAs structure. For simplicity and comparison with previous results, the average barrier height

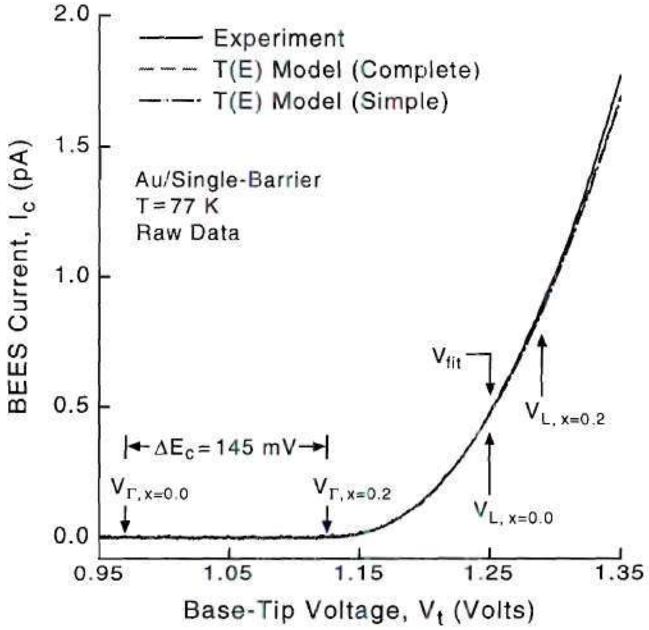

Figure 4.3: Comparison of models to raw experimental BEES data ($T = 77$ K, $I_t = 10$ nA) in the threshold region. The Au/Heterostructure model includes all interfaces while the Au/$Ga_{0.8}Al_{0.2}As$ model treats the semiconductor as homogeneous $Ga_{0.8}Al_{0.2}As$ (a common approximation). $V_{\Gamma,x=0.0}$ and $V_{\Gamma,x=0.2}$ label the experimentally-determined Schottky barrier heights for the Au/GaAs and Au/$Ga_{0.8}Al_{0.2}As$ interfaces, respectively. $V_{L,x=0.0}$ and $V_{L,x=0.2}$ were calculated from data in Ref. [38].

on the single-barrier structure will be determined using the simple model since any variation in $V_b$ between the two models should be very small [73].

To illustrate this experimental technique for determining the band offset for a given material, the threshold region of a typical spectrum taken on a barrier structure at $T = 77$ K is shown in Fig. 4.3 for a tunneling current $I_t = 10$ nA. Both the simple model, which treats the structure as a single Au/$Ga_{0.8}Al_{0.2}As$ interface (dash-dot line), and the complete model, which treats the structure as a Au/Heterostructure (dashed line), have been fit to the data. The schematic of the heterostructure used (prior to passivation and metal deposition) in the complete model is depicted in Fig. 4.1. The complete model has a barrier height that is determined by the Au/GaAs interface ($V_{\Gamma,x=0.0}$), and the simple model has a barrier height that is determined by an Au/$Ga_{0.8}Al_{0.2}As$ interface ($V_{\Gamma,x=0.2}$). For both models, Γ conduction band offsets were determined using $\Delta E_{c,x} = Q_c \times [E_g^\Gamma(x) - E_g^\Gamma(x = 0.0)]$ with $Q_c = 0.62$ [38]. The models were fit up to a maximum voltage $V_{fit} = 1.25$ V with two variable parameters, the Schottky barrier height and an energy-independent scale factor. The experimental conduction band offset $\Delta E_{c,x=0.2}$ was determined by taking the difference between the average barrier height on a separate Au/GaAs sample and the average barrier height on the GaAs/$Ga_{0.8}Al_{0.2}As$/GaAs structure (determined by the single-interface model for simplicity) as described previously. Using this method, we have measured $\Delta E_{c,x=0.2} =$ 145 meV or $Q_c = \Delta E_c/\Delta E_g = 0.58$, which agrees well with the accepted value of 154 meV or $Q_c = 0.62$ [38]. This is in contrast to the value of 200 meV that has been reported on a similar structure [73].

## 4.3 Determination of the Phase Lag $d$

In Fig. 4.3, both models were fit in energy up to the onset of the L minima in GaAs ($V_{L,x=0.0}$) and appear to provide equally accurate descriptions of the data up to the onset of the L minima in $Ga_{0.8}Al_{0.2}As$, ($V_{L,x=0.2}$). At this energy, the experimental data exceed the simulations because the L minima represents new channels (additional states) that the electrons can be transmitted into that are not included in the single-minimum models. In the low energy regime, although both models appear to describe the data equally well, the low noise in the measured spectra ($<$ 3 fA rms) enables the detection of very subtle features that cannot be reproduced by the simple Au/$Ga_{0.8}Al_{0.2}As$ single-interface model and are only apparent in the first and second-derivatives. The extra features can be accurately described by the complete Au/Heterostructure model, provided the phase-lag $d$ introduced by interference in the GaAs input region is correct. The optimum phase-lag (value of $d$) can be determined by adjusting the value of input thickness $d$ to achieve the minimum mean squared-error between the experimental spectrum and the simulation. Figure 4.4 shows the

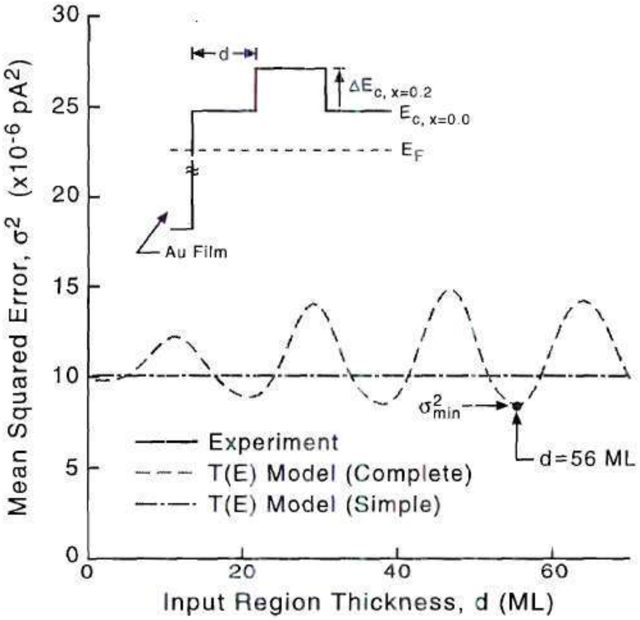

Figure 4.4: The mean-squared-error between the experimental spectrum and each model as a function of the model input region thickness $d$ in monolayers (ML). The minimum mean-squared error occurs for the value of $d$ that best reproduces the phase lag of the electron-wave incurred while traveling through the input region. Inset shows the ideal band diagram for the heterostructure.

result of fitting the spectrum with various values of $d$ ranging from 0 ML (no input region) to 70 ML (the design thickness of the structure). Due to the passivation process, the true value should lie somewhere between these two extremes. For this spectrum, the minimum error $\sigma^2_{min}$ occurs for an input-region thickness of $d = 56$ monolayers (ML), which is very reasonable considering the growth thickness (70 ML) and the amount of material removed by the passivation process [74]. Note that the optimum $d$ is not necessarily the same as the true width of the input region because of the assumptions made in deriving the model (e.g. flat bands). Even given these differences, the excellent agreement between model and experiment (see also Figs. 4.6 and 4.7) shows that the underlying physics is correct. Thus, the optimum thickness determined should at least be somewhat similar to the true thickness.

In order to investigate how accurately the optimum phase lag approximates the actual thickness of the input region and to determine how precisely it can be measured using this technique, additional types of BEES experiments must be performed. To address the question of whether or not controlled changes in the thickness of the input region produce corresponding changes in the value of $d$, the surface passivation has been performed repeatedly on a single sample before metal deposition. Since the passivation removes the surface oxide and regrows an oxide that is approximately 1 nm thick [74], by performing the etch an integer multiple of times the thickness of the input region can be systematically reduced by a small amount without introducing the surface to any new chemical process that may alter the spectra. The results of these experiments showed that each repetition of the surface preparation, which should remove 5-10 ML of the input region, reduced the value of $d$ by approximately 15 ML/etch. The measurements were performed on samples that had been etched 1 to 4 times. Although they do not conclusively establish the relationship between the two quantities, these results do confirm the correspondence between the actual thickness and $d$ by showing a reasonably systematic and simultaneous decrease in both quantities. In addition, the amount of the reduction, 15 ML/etch, agrees roughly with estimations based on the findings of Talin *et al.* [74]

To determine how accurately the phase lag can be determined, or equivalently how much $d$ varies across a given sample, a large number of spectra must be acquired and analyzed. A histogram of the $d$ values obtained on a typical sample (etched once) is displayed in Fig. 4.5. To produce this plot, 84 spectra were obtained using automated data acquisition. The spectra were obtained while imaging the sample surface and were acquired in several different macroscopic spatial locations. For this sample, the average value of $d$ is 55 ML and the full width at half maximum (FWHM) is approximately 2-3 ML. Similar results were obtained on samples prepared in the same manner and measured at 7 K. Unfortunately, due to the damaging nature of the sample transfer procedure, a single sample cannot be measured at both 7 K and 77 K.

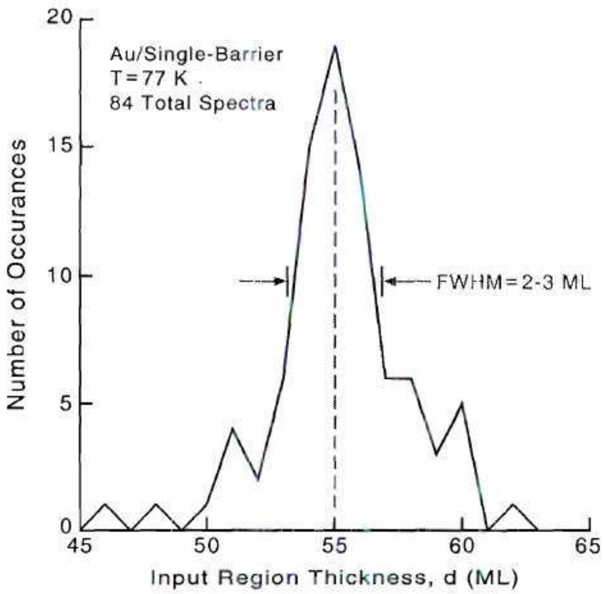

Figure 4.5: A histogram of the values of the phase lag for 84 spectra taken on a typical single-barrier device. The FWHM for the histogram represents the resolution of the measurement and is on the order 2-3 ML.

## 4.4 Electron-Wave Interference Effects

The single-barrier device was designed to provide a reference sample for measurements on quarter- and half-electron-wavelength Fabry-Perot interference filters. These resonant devices are designed specifically to exhibit destructive and constructive interference of the incident electron waves. However, even though the single-barrier structure was not designed nor optimized to exhibit interference effects, the thickness of the input region and the value of the electron energy (wavelength) in the input material are such that interference effects can occur. In addition, there are also interference effects due to the finite thickness of the barrier region, but these do not contribute significantly at energies relevant to the BEES spectrum (below the threshold of the L-minima in $Ga_{0.8}Al_{0.2}As$). The interference due to the small, finite thickness of the input region produces small features (resonant peaks) in the electron transmittance function. To illuminate the effect of these very subtle features on

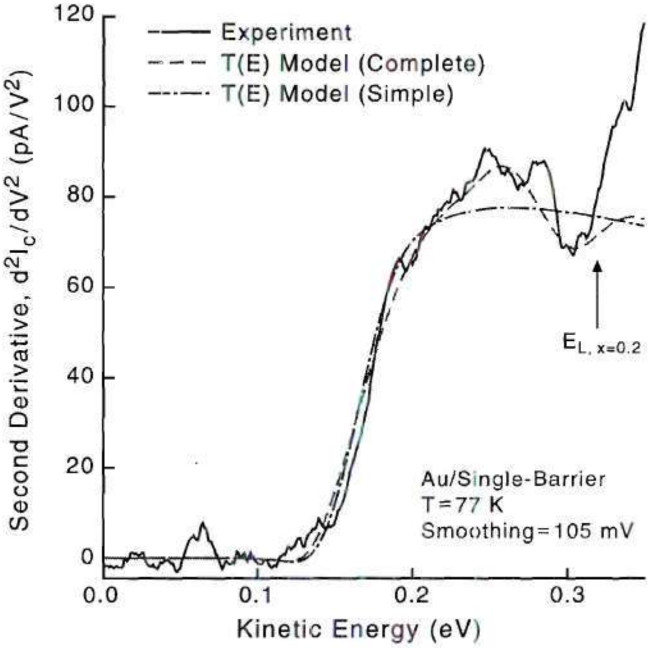

Figure 4.6: second-derivatives of the experimental and model BEES spectra from Fig. 4.3 ($T = 77$ K). Kinetic energy refers to GaAs regions. Features due to electron-wave interference are apparent in the experimental spectrum and are well-described by the complete multiple-interface Au/heterostructure model. Resolution of these features relies on low measurement noise ($< 3$ fA rms) and small positional drift ($< 0.2$ nm).

the BEES spectrum, the second-derivative of the experimental spectrum and models must be utilized.

To calculate the second-derivative of the experimental data, a combination of smoothing and numerical differentiation is necessary. The extremely small signals inherent to the BEES technique ($\sim$ pA's) make differentiation especially difficult. Thus to perform the differentiation, a fourth-order Savitsky-Golay filter [75] over a 105 mV window (filter parameters $ld = 2$, $m = 4$) has been used. To ensure optimum performance, the width of the window has been chosen to coincide with the approximate width of the resonant features in $T(E_x, E_t)$ as suggested in Ref. [75].

To reveal the effect of the electron-wave interference in the input region, the BEES second-derivative spectra, $d^2I_c/dV^2$ vs. $V$, are shown in Fig. 4.6 for the data and models

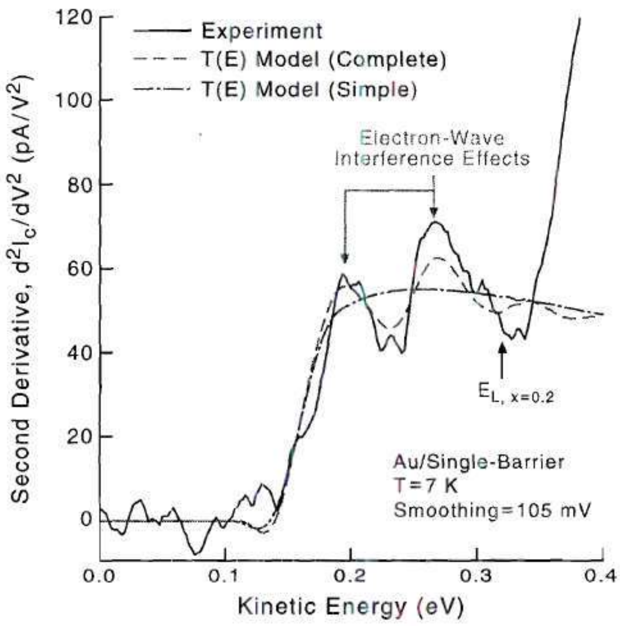

Figure 4.7: Experimental second-derivative spectrum acquired at 7 K compared with both the simple and the complete BEES models. All primary features are reproduced well by the complete Au/heterostructure model, while the simple Au/$Ga_{0.8}Al_{0.2}As$ model (single-interface approximation) fits only the mean value of the second-derivative spectrum.

from Fig. 4.3. The complete Au/heterostructure model provides a remarkably accurate description of the experimental data up to the onset of $E_{L,x=0.2}$ at 320 meV [38] where the single minimum model is no longer valid. The simple single-interface model fits the initial slope of the data, but does not reproduce the peaks and valleys that arise from electron interference between the Au/GaAs, GaAs/$Ga_{0.8}Al_{0.2}As$, and $Ga_{0.8}Al_{0.2}As$/GaAs interfaces.

By reducing the temperature from 77 K to 7 K, the energy resolution of BEES increases by an order of magnitude making the features in the second-derivative more pronounced. To illustrate the sharpening of the resonant features, the second-derivative spectra for typical data and model fits are shown in Fig. 4.7. The spectra show that the same conclusions hold for BEES spectra acquired at the lower temperatures. As predicted, the resonant features, which can now be clearly identified as peaks (and valleys) in the spectrum, are more distinct. As for the sample measured at 77 K, the band offset and phase lag have been determined at 7 K. For this sample we find $\Delta E_{c,x=0.2} = 150$ meV or $Q_c = 0.60$, and a best-fit $d = 64$ ML. At both temperatures, the widths and energy positions of all features are well-described by the complete Au/heterostructure model up to $E_{L,x=0.2}$ and are only described on average by the simple single-interface model.

Due to the highly subtle nature of the results presented, and the extremely accurate description achieved by the model, the reproducibility and number of spectra analyzed should be discussed. The results presented in Figs. 4.6 and 4.7 are typical of those found for all samples. Each high-resolution spectrum is an average over 40 voltage sweeps (400 points at 2 mV increments), and took nominally 40 minutes to acquire. With a drift rate at 77 K (7 K) of approximately 0.3 nm/hr (0.05 nm/hr), it is clear that the features observed are not distorted by positional drift of the tip across the surface. Several samples were tested at each temperature and a large number of spectra were acquired on each, at differing locations ($\sim$ 100 spectra at each temperature). Approximately 75% of the spectra were accurately described by the model, while the other 25% contained features of larger amplitude than could be reproduced in the simulation. As shown in Fig. 4.5, for a given sample, a histogram of $d$-values from the set of accurately-fit spectra shows a peak centered at 50-70 ML (depending on the sample preparation), with a full-width-at-half-maximum of typically 4 ML. Distinguishable changes in the shapes of the experimental spectra correspond to $\sim$ 2 ML changes of $d$ in the model. It is important to note that the sensitivity to thickness fluctuations will depend on the particular structure under study. Structures with more pronounced features in the transmittance (due perhaps to a larger effective mass such as in the valence band of a p-type device) will be difficult to fit if $d$ is incorrect thus leading to increased sensitivity. Therefore, most of the spread in $d$-values measured is likely due to actual positional variations of the input-region thickness.

## 4.5 Discussion

In this chapter, high-resolution BEES spectra have been acquired that show distinct features arising from electron interference in single-barrier semiconductor heterostructures under zero-bias conditions. The inclusion of the correct phase-lag due to the electron traveling through the input region of the device was shown to be essential to obtaining an accurate description of the experimental second-derivative spectra. The results demonstrate that reflection from all interfaces in the heterostructure must be included in a realistic model, even if there is no apparent confinement. The simple single-interface model that is widely used to measure band offsets in these heterostructures was shown to model only the average shape of the BEES second-derivative spectrum, while a multiple-interface model accurately reproduced the distinct oscillatory features caused by electron resonance in the input region of the device. These effects have been resolved at both 77 K and 7 K. As predicted by the energy-dependent resolution of BEES, the resonant features sharpened and became more distinct as the temperature was reduced. In addition to the interference effects, the band offset of the $Ga_{0.8}Al_{0.2}As$ has been measured at both 77 K and 7 K using BEES.

It is important that such subtle features due to interference be identified in order to facilitate the correct interpretation of spectra from more complex heterostructures. Using this approach of gradually increasing the complexity of the device and extending the model accordingly, a better understanding of ballistic transport in quantum devices is possible and the limitations of BEES is realized. The understanding gained about this simple reference sample is key to describing the BEES spectra acquired on the resonant devices in the following chapter. In particular, if the correct phase lag is not included, a complete description of the devices can not be achieved.

# Chapter 5

## Resonant Device Measurements

Pushed by the electronics industry, semiconductor devices have steadily increased in speed and functionality and decreased in power consumption over the last forty five years. These improvements have been the direct result of decreasing device sizes over this period. At the same time, new ultrasmall structures are forming the basis of the new class of quantum devices with unique capabilities in very high frequency electronics, in very low power electronics, and in optoelectronics. Semiconductor heterostructures and superlattices represent one class of quantum devices in which resonant levels (quasibound states) have been exploited for novel functions such as quantum-well infrared photodetectors (QWIP), infrared LED's, and infrared lasers [76]. Measurement techniques capable of providing information about the energy positions, energy widths, and relative amplitudes of these resonant levels are essential for device design and realization. The transmittance of ballistic electrons across the heterostructure as a function of the injected electron energy is a useful quantity for characterizing such structures because, for fixed electric field (determined by the external voltage bias across the heterostructure), the transmittance function shows directly the energy position and width of each quasibound state [11, 41, 50]. As discussed in Chap. 1, this is in contrast to typical optical spectra that reflect transitions between states, and to conventional two-terminal current vs. voltage (I-V) spectra, for which the electric field across the heterostructure is not constant.

Building on the success achieved in describing both the single-interface (Chap. 3) and the single-barrier (Chap. 4) structures, this chapter focuses on measurements taken on one of the most fundamental quantum devices, the double-barrier resonant tunneling diode (DBRTD). This structure, originally developed and tested by Esaki and Tsu [77] in 1970, forms the foundation for a variety of quantum devices that range from transistors to a newly developed semiconductor infrared laser known as the quantum cascade laser [78, 79]. The DBRTD is a simple yet elegant device that utilizes quantum mechanical tunneling through a quasibound resonant state in a buried quantum well to achieve a negative differential resistance. Over the past 28 years, a very in-depth understanding of this structure has been used to explore and discover numerous basic and applied physical principles. This work, performed by Esaki and Tsu (and the many others that have followed), laid the groundwork that opened an entirely new area of research in which familiar concepts from quantum mechanics could be tested on a scale that was not previously accessible.

## 5.1 Background

For planar devices such as the DBRTD, the electron transmittance at normal incidence is the most relevant and most important quantity for describing carrier transport because a large portion of the transmitted current in this type of device is due to the forward traveling electrons ($E_t = 0$). Given the extent to which the carrier transport in the DBRTD is understood, it is surprising that a measurement of the zero-bias $T(E)$ has not yet been performed. This quantity is fairly simple and straightforward to compute, however, measuring such a quantity experimentally is extremely difficult. Fortunately, BEES is ideally suited for measuring the electron transmittance as a function of the injected energy for buried heterostructures such as DBRTD's [11]. The main complication associated with using BEES arises from the range of energies and momenta that are injected by the STM tip. As discussed in Chap. 2, to extract the normal-incidence electron transmittance from the BEES spectra, the second-derivative of the BEES current ($d^2I_c/dV^2$ where $V$ is the applied tip bias) is needed. More rigorously, Smith and Kogan [41] have shown that, for the effective mass model used in Eq. (2.1), the $d^2I_c/dV^2$ spectrum is proportional to the normal incidence transmittance multiplied by a slowly varying function. If the features of $T(E)$ are relatively large and distinct (compared to the slowly varying function), then the $d^2I_c/dV^2$ spectrum provides a good representation of the transmittance *function*. Thus, since BEES allows for a device bias independent of the injected carriers, a complete characterization of the device should be possible by applying a series of base-collector voltages, and measuring the transmittance for each bias.

Given the temperature dependence of the BEES energy resolution (3.5 $k_BT$), it is interesting and important to investigate theoretically to what degree the transmittance can be reproduced by the second-derivative spectrum. To evaluate a best case scenario of what can be expected experimentally, the ideal electron transmittance for a given device must be compared to the $d^2I_c/dV^2$ of simulated BEES spectra computed at various temperatures. To illustrate, an example of this type of analysis for the DBRTD measured later in this chapter is shown in Fig. 5.1. The $\mathrm{Ga}_{1-x}\mathrm{Al}_x\mathrm{As}$ DBRTD was designed using the analogies between electron-waves and electromagnetic waves [3] and has two quasibound states $E_1$ and $E_2$. The ideal electron transmittance (at normal-incidence and zero-bias) for kinetic energies below the $L$-minima contains a peak corresponding to the tunneling resonance $E_1$ and a peak corresponding to the above-all-barrier resonance $E_2$. The less pronounced peak between $E_1$ and $E_2$ results from interference effects due to the finite width input region (the distance between the M/S interface and the heterostructure) as discussed in Chap. 4 for the single-barrier structure. A plot of the simulated BEES current $I_c$ ($T = 7$ K and 77 K) as a function of the applied tip bias, calculated using the $T(E)$ model, is shown in Fig. 5.1 below the device schematic. For the simulated BEES spectra, the location of the quasibound states, indicated by the arrows, appear as broadened kinks in the monatomic $I$–$V$ spectrum. By taking the second-derivative of the spectra, the electron transmittance, and the peaks corresponding to the quasibound states, are recovered. Even at 77 K, the $d^2I_c/dV^2$ spectrum not only reproduces the position of the resonances, but, to a large

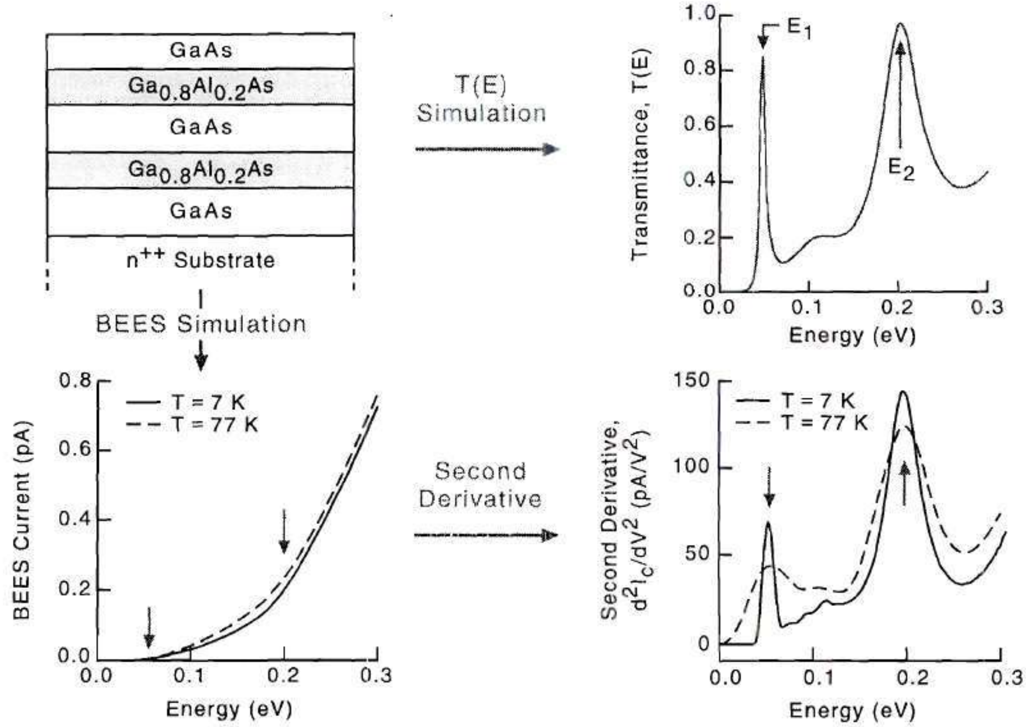

Figure 5.1: BEES measurement of the normal-incidence electron transmittance. (a) Device schematic of a $Ga_{1-x}Al_xAs$ DBRTD with two quasibound states $E_1$ and $E_2$. (b) Calculated ideal electron transmittance for the designed quantum device. (c) Simulated BEES current ($T = 7$, 77 K) for the designed device with a thin Au film deposited onto the surface. The arrows represent the location of the quasibound states $E_1$ and $E_2$. (d) The second-derivative of the simulated currents ($d^2I_c/dV^2$) showing the proportionality between transmittance and the second-derivative of $I_c$ for the two temperatures.

degree, it reproduces the shape of the entire transmittance function as well. By reducing the temperature to 7 K, the accuracy of the reproduction increases considerably as expected.

From the simulated spectra displayed in Fig. 5.1, the power, versatility, and utility of this method for measuring electron-wave interference effects in quantum semiconductor heterostructures is obvious. Using this technique, a very fundamental but difficult to measure quantity, the electron transmittance function, can be obtained. Unfortunately, actual measurements may not be able to achieve such insightful results due to experimental difficulties such as small signals, noise, and positional drift which inhibit the ability to perform numerical differentiation on the data. Due to these difficulties, a large portion of the previous BEES measurements on heterostructures have not involved the use of the $d^2I_c/dV^2$ spectrum. Thus, the relationship between $T(E)$ and $d^2I_c/dV^2$ (which has been established analytically [3, 41]), has not been proven experimentally.[1] Therefore, the measurements taken on the DBRTD structures will serve two purposes: to illustrate the ability of BEES to measure electron-wave interference effects and to determine to what degree the ideal results presented in Fig. 5.1 can be achieved.

## 5.2 Resonant Device Design

To realize the full potential of BEES as a tool for investigating electron-wave interference effects in quantum devices, the similarity between $T(E)$ second-derivative spectrum must be established conclusively. This has been attempted previously by Smith and Kogan [41] (using the experimental data from Ref. [50]) whose results proved to be less than satisfying due to poor agreement between the model and the data. To address this deficiency, a set of heterostructures specifically designed for BEES testing have been optimized

---

[1] Most of the measurements on heterostructures to date have not utilized the second-derivative spectrum because of the high signal-to-noise ratio needed. The one set of measurements by Sajoto *et al.* [50] that did utilize the second-derivative spectrum only studied the location and temperature dependence of the quasibound states, and did not provide a stringent test of the similarity.

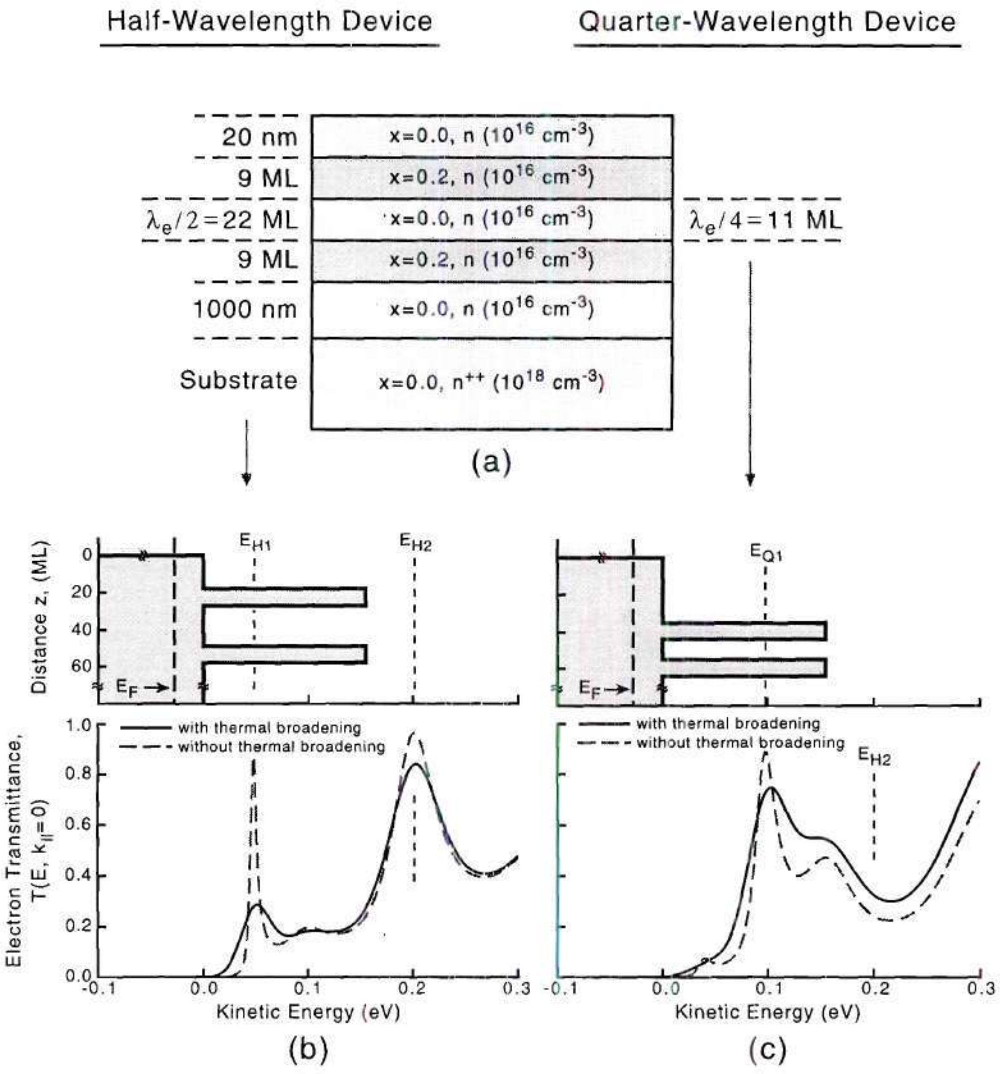

Figure 5.2: (a) A schematic diagram of the quarter- and half-electron-wavelength Fabry-Perot filters designed to test the energy resolution of BEES. The band diagram and electron transmittance function for the (b) half- and (c) quarter-electron-wavelength device. The thermally broadened transmittance represents the best description of the transmittance functions that the BEES second-derivative spectrum can provide at 77 K.

to exhibit electron-wave interference effects. A schematic representation of the devices is shown in Fig. 5.2a. These structures include both a quarter- and a half-electron-wavelength Fabry-Perot quantum interference filter (using terminology consistent with electromagnetics optics) that have been designed to produce electron transmittance functions that exhibit distinct features due to the quasibound resonances. The band diagram and normal-incidence electron transmittance function for each device is shown below in Figs. 5.2b-c. For each device, the simulation of the ideal electron transmittance at normal incidence shows the location and width in energy of the designed resonant states. These structures have been designed to behave in a complementary manner in order to achieve a complete test of the technique. The nature of this complementary behavior is illustrated in Fig. 5.2c where the dashed line labeled $E_{H2}$ indicates that the quarter-wavelength device produces destructive interference where the half-wavelength device produces constructive interference. The reproduction of these distinct, complementary features will be used to establish the degree to which the $d^2I_c/dV^2$ spectrum can provide the electron transmittance function.

To address the problems related to the temperature dependence of the energy resolution of the technique (see Fig. 5.1), a thermally broadened version of the electron transmittance is also shown in Fig. 5.2. Assuming that the second-derivative spectrum could reproduce $T(E_x, E_t = 0)$ exactly within the inherent energy resolution of the technique, the broadened version[2] represents the best description of the transmittance functions that BEES can provide at liquid nitrogen temperatures. In fact, the similarity can be readily seen by comparing the thermally broadened transmittance in Fig. 5.2b to the second-derivative spectrum calculated at 77 K in Fig. 5.1. To resolve the very narrow features such as the tunneling resonance $E_{H1}$, the measurements must be performed at liquid helium temperature which is more difficult to achieve.

---

[2] The broadened transmittance is calculated by convolving $T(E_x, E_t = 0)$ with a Gaussian of FWHM of 23 mV (the thermal resolution of BEES at 77 K).

## 5.3 Low-Temperature Measurements

In this section, the results of measuring (by BEES) the definitive set of complementary resonant devices are presented. As stated above, to be consistent with the terminology used in electromagnetic optics, these devices are referred to as "half-wavelength" and "quarter-wavelength" interference filters due to the constructive and destructive nature of the interference at the design energy. It is important to emphasize that these devices are half-wavelength and quarter-wavelength *only* at the design energy. The transmittance as a function of energy, as measured in this work, describes the response of the device over a broad range of energies. The devices constructed include a half-electron-wavelength ($\lambda_e/2$) device with an above-barrier quasibound state at the design energy, and a quarter-electron-wavelength ($\lambda_e/4$) device with destructive interference at the design energy. In addition, both devices also support one tunneling resonance below the onset of the GaAs $L$-minima. In fact, both of the devices have been intentionally designed such that all relevant features in the transmittance are within the first minima to make interpretation of the results simple and clear. All of the BEES spectra have been taken at temperatures of 7 K, 77 K, and 300 K, with zero external voltage bias across the devices. Before metal deposition, the sample surface was prepared as discussed in Chap. 3 for the Au/GaAs(100) devices.

Using detailed analogies between electron-waves and optical waves [3], the active region of the $\lambda_e/2$ device was designed to have an above-barrier quasibound state for an electron kinetic energy of 0.20 eV in the GaAs regions. The ideal band diagram for the device, showing the energy of the above-barrier state $E_{H2}$ as well as the tunneling state $E_{H1}$, is shown in Fig. 5.3a. From model fits, the thickness $d$ of the input region (which depends on sample preparation [80]) was determined to be 19 ML. A simulation of the electron transmittance at normal incidence, confirming the energies and showing the width of the resonant states, is shown in Fig. 5.3b. Also shown in Fig. 5.3b is a thermally broadened transmittance function which has been computed by convolving $T(E, \mathbf{k}_{\|} = 0)$ with a Gaus-

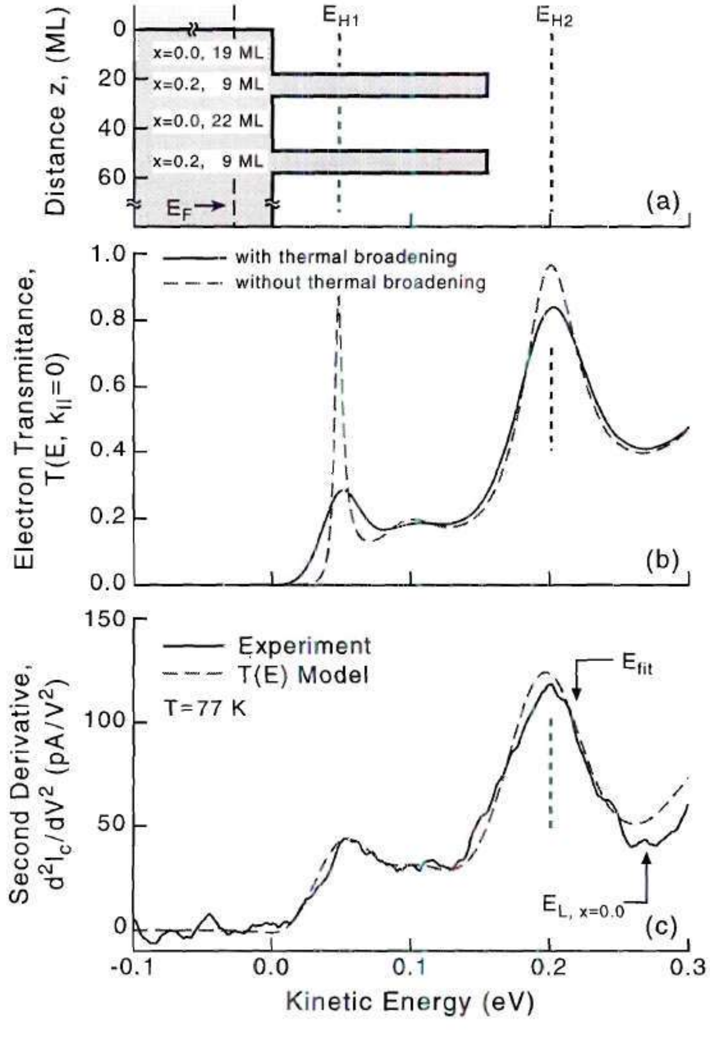

Figure 5.3: (a) The band diagram and (b) the corresponding normal-incidence electron transmittance function $T(E, \mathbf{k}_{\|} = 0)$ with and without thermal broadening for the designed *half-electron-wavelength* resonant device which has one tunneling resonance $E_{H1}$, and one above-all-barriers resonance $E_{H2}$. (c) Second-derivatives of the experimental spectrum and of the BEES $T(E)$ model spectrum for data acquired at $T = 77$ K. The spectrum accurately reproduces the shape of the thermally broadened $T(E, \mathbf{k}_{\|} = 0)$, which represents the resolution limit of BEES.

sian of full-width-at-half-maximum 23 meV, the thermal resolution of BEES at 77 K. The thermally broadened $T(E, \mathbf{k}_{\|} = 0)$ represents the best description of the $\lambda_e/2$ device transmittance that BEES can provide at 77 K. The minor peak just above the tunneling state is a result of electron interference effects in the device input region [80]. Figure 5.3c shows a typical BEES second-derivative spectrum, $d^2I_c/dV^2$ vs. kinetic energy (in GaAs), which has been calculated using BEES $I_c$–$V$ data taken at 77 K for a tunnel current of 10 nA. Also shown is the second-derivative spectrum of the full BEES $T(E)$ model [11, 71] which has been fit up to a maximum energy $E_{fit} = 0.22$ eV with three variable parameters: the Schottky barrier height (shifts the spectrum in energy), an energy-independent scale factor, and the thickness of the input region (determines position and size of minor peaks [80]). The $T(E)$ model (which incorporates the calculated $T(E_x, E_t)$ for all angles) reproduces all relevant features of the data including peak locations, peak widths, and peak-to-valley ratios up to an energy just below the onset of the L-minima in GaAs, $E_{L,x=0.0}$. At this energy, additional transport channels open and the single-minimum model used is no longer valid. Below this energy, the experimental spectrum clearly demonstrates the existence of the designed above-barrier energy resonance $E_{H2}$, and, except for a slowly-varying background [11, 41], reproduces nearly the exact shape of the thermally broadened $T(E, E_t = 0)$ (see Fig. 5.3b, solid line). This comparison shows that, for the first time, the thermal limit of the technique has been achieved at 77 K.

To confirm that the above-barrier state $E_{H2}$ is created by constructive interference in the half-electron-wavelength layer, a complementary device was fabricated in which the length of the active layer was reduced to a quarter-electron-wavelength at the design energy. This reduction of the active layer width should produce destructive interference at the design energy, $E_{H2}$. The ideal band diagram for the $\lambda_e/4$ device and the corresponding $T(E, E_t = 0)$ (ideal and thermally broadened) are shown in Figures 5.4a and 5.4b, respectively. The thickness of the input region was determined to be 35 $ML$ from model fits. The tunneling resonance $E_{Q1}$ is located between $E_{H1}$ and $E_{H2}$ providing a drastically different

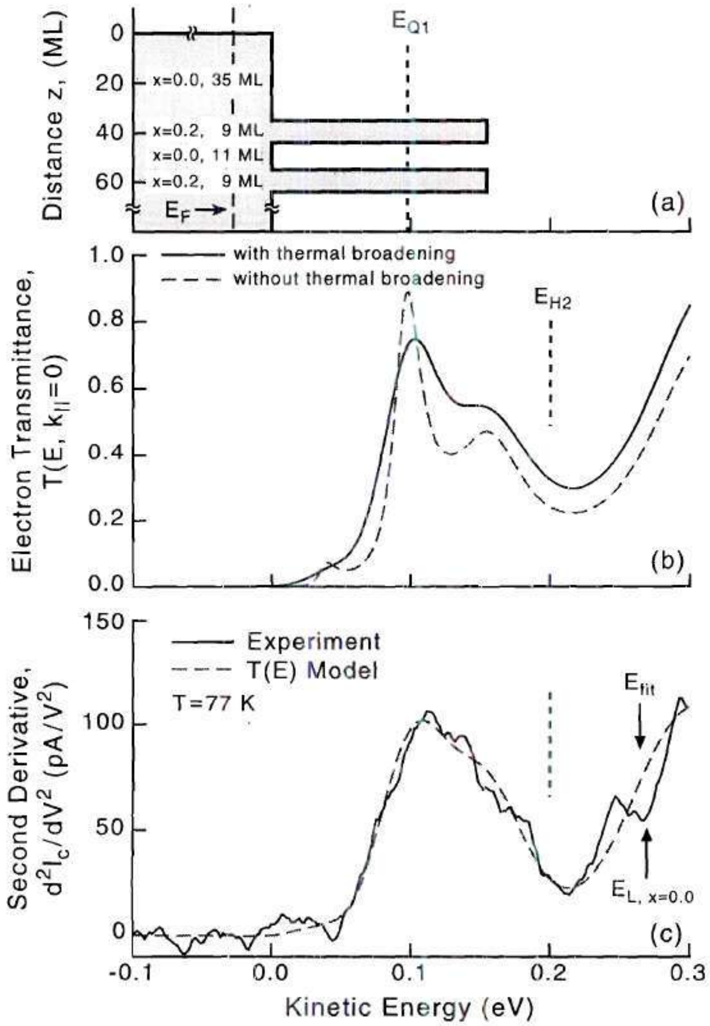

Figure 5.4: (a) The band diagram and (b) the corresponding normal-incidence electron transmittance function $T(E, \mathbf{k}_{\|} = 0)$ with and without thermal broadening for the designed *quarter-electron-wavelength* resonant device which has one tunneling resonance $E_{Q1}$. (c) Second-derivatives of the experimental spectrum and of the BEES $T(E)$ model spectrum ($T = 77$ K). These demonstrate that the constructive interference which led to the above barrier state $E_{H2}$ has been removed by changing the thickness of the active layer from half-wavelength to quarter-wavelength.

characteristic compared to the $\lambda_e/2$ resonant device. Second-derivatives of the experimental and modeled BEES spectra from the $\lambda_e/4$ device are shown in Fig. 5.4c. The $T(E)$ model was fit up to a maximum energy of $E_{fit} = 0.26$ eV and reproduces all relevant features up to at least $E_{L,x=0.0}$. The existence of the tunneling resonance and the absence of the above-barrier resonance are clearly illustrated, and, for this complementary case, the data again show good agreement with the ideal normal-incidence electron transmittance and excellent agreement with the thermally broadened transmittance.

To complete the low temperature analysis, measurements were also taken on the $\lambda_e/4$ device at liquid helium temperatures. Although this corresponds to 4.2 K, the lowest temperature at which BEES can be performed in our system is 7 K due to the small thermal losses. Obtaining the low-temperature measurements are much more difficult than their 77 K counterparts because the closed and isolated nature of the liquid helium dewar. The main chamber of the dewar forms a resonant chamber in which bursting bubbles of helium gas cause large vibrations which upset the sensitive tip-sample seperation. With extensive averaging, each high-resolution spectrum requires approximately an hour to obtain. The time required is twice as long as a similar spetrum taken at 77 K due to the increase resistance of the buffer layer which separates the device from the conducting substrate. In this time interval, the probability of experiencing a disturbance, which reduces the signal-to-noise ratio significantly, is high.

The advantage of performing the measurements at this extremely low temperature is the increased energy resolution provided by the sharpening of the Fermi distributions in the metal tip and base. At this temperature, the energy resolution is on the order of a few millivolts (an order magnitude better than at 77 K), which should provide a more exact reproduction of the electron transmittance function. However, because of noise in the data along with the small signal levels, a relatively large smoothing window ($\sim 100$ meV) must be utilized to compute a useful second-derivative spectrum from the experimental data. Thus, at 7 K, the limiting factor may shift from the broadening of the Fermi statistics to

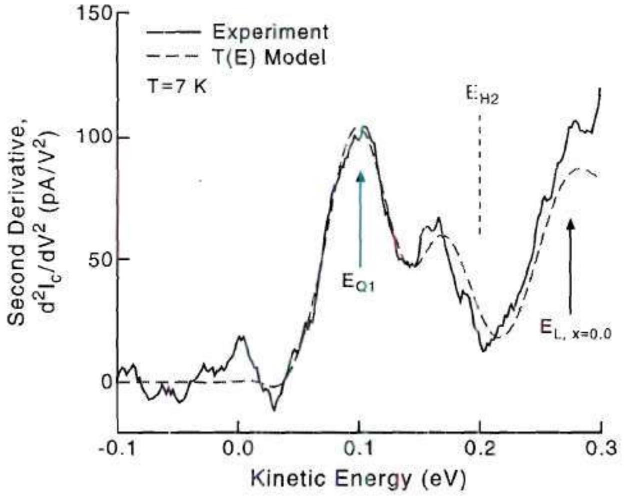

Figure 5.5: Experimental second-derivative spectrum with model fits for the quarter-electron-wavelength Fabry-Perot quantum interference filter taken at $T = 7$ K. At this low temperture, the energy resolution is sufficient to resolve the individual peaks associated with each of the quasibound states. At 77 K (see Fig. 5.4c), the individual features could not be easily recognized due to the temperature induced broadening.

the numerical differentiation of the collected data. Shown in Fig. 5.5 is a typical second-derivative spectrum computed using data taken on a $\lambda_e/4$ device at 7 K. The most obvious difference between this spectra and the data in Fig. 5.4c is the resolution of both the designed quasibound state $E_{Q1}$ and the additional feature caused by interference in the input region. At 77 K, the individual features could not be easily recognized because of the temperature induced broadening. However, at 7 K peaks corresponding to each *individual* resonance are obvious and clear. The data is again well described by the model up to the threshold associated with transmission into the L-minima of GaAs. Comparison with the ideal electron transmittance in Fig. 5.4b shows that the second-derivative spectrum in Fig. 5.5 almost reproduces the exact shape of the normal-incidence $T(E)$ for this structure.

## 5.4 Room-Temperature Measurements

Finally, given the importance of room temperature device operation, the structures were tested at 300 K to determine if the coherence length is large enough to produce the resonances, and to determine if the energy resolution of the measurement is high enough to provide a useful measurement of the normal incidence $T(E, E_t = 0)$ at higher temperatures. Measurements at room temperature are difficult because the large thermal fluctuations present induce a lateral drift of the STM tip and because thermally excited carriers can overcome the Schottky barrier greatly increasing the noise in the measured collector current. Due to inhomogeneous broadening, the tip drift limits the amount of signal averaging that can be utilized. Lastly, as the temperature increases, scattering events reduce the already small collected current.

In order to achieve the high signal-to-noise ratio needed to enable second differentiation of the experimental data, the thermal drift must be severely inhibited. At low temperature, the entire STM is submerged in a large dewar of either liquid nitrogen or liquid helium. This configuration holds the entire system at a constant temperature of 77 K or 7 K, respectively. To obtain the room temperature measurement, the liquid nitrogen in the dewar was replaced with water in order to reduce thermal fluctuations caused by changes in the ambient temperature. The modification reduced the lateral drift rates to the point where sufficient signal averaging could be performed and measurements were made on both of the resonant devices.

To illustrate the ability to perform high-resolution measurements at 300 K, Figs. 5.6a and 5.6b show second-derivatives of the experimental and model BEES spectra from the $\lambda_e/2$ and $\lambda_e/4$ devices taken at room temperature. Although most of the features that were obvious in the low-temperature spectra are broadened significantly by the temperature, all of the resonant states are still discernable in the spectra. The reproduction of these features implies $T(E_x, E_t)$ functions similar to those shown in Figures 5.3b and 5.4b, and clearly

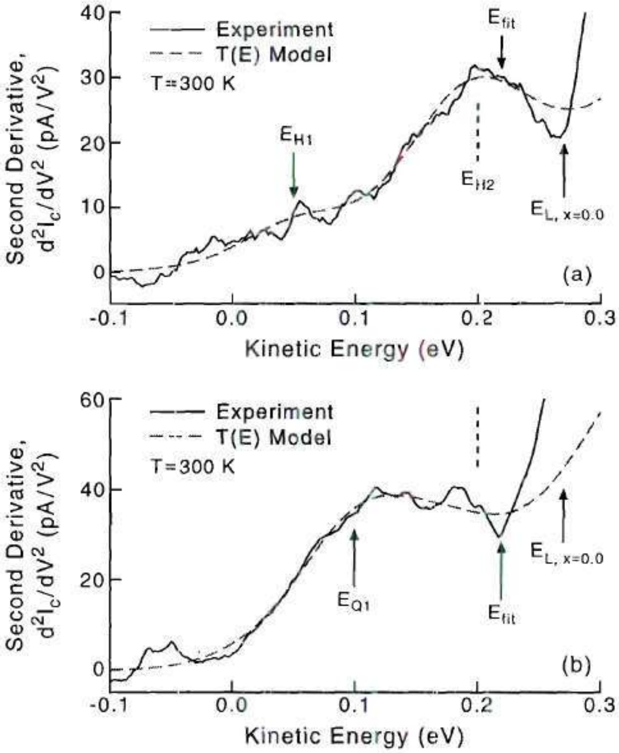

Figure 5.6: Second-derivatives of the experimental and modeled BEES spectra for (a) the half-electron-wavelength and (b) the quarter-electron-wavelength devices for data acquired at $T = 300$ K. Although thermally broadened, all resonant states ($E_{H1}$, $E_{H2}$, and $E_{Q1}$) are discernable, clearly demonstrating that the electron coherence length at room temperature is much greater than the length of the $\lambda_e/2$ device.

shows that the electron coherence length must be much greater than the length of the device in each case. However, the thermal broadening at room temperature unfortunately reduces the ability to measure $T(E, E_t = 0)$ directly.

## 5.5 Discussion

In this chapter, high resolution BEES spectra taken on a set of complementary quantum-interference filters have been used to confirm experimentally the proportionality between the BEES second-derivative spectrum and the normal-incidence electron transmittance function, for the case of zero voltage bias. Measurements were acquired on both structures at 7 K, 77 K, and 300 K. By reducing the temperature, the features in the second-derivative became sharper as predicted by the semiclassical model. Data taken on the half-electron-wavelength device demonstrate the first direct transport measurement of an above-barrier quasibound state at zero-bias. Spectra from the quarter-electron-wavelength device clearly show that the $\lambda_e/2$ resonance is generated by constructive interference in the half-wavelength-thick GaAs well. By reducing the temperature from 77 K to 7 K, features in the second-derivative spectrum became much more pronounced allowing for an almost exact reproduction of the transmittance function. In addition to the low-temperature measurements, the structures were also investigated at high temperature which is significantly more difficult due to increased thermal excitations and lateral drift of the the STM tip. Surprisingly, all of the resonant states were also evident in room-temperature spectra, which implies an electron coherence length at 300 K much greater than the $\lambda_e/2$ device length ($\sim 100$ nm).

These measurements provide direct characterization of the electron transmittance in quantum semiconductor structures, a function that is quite difficult to obtain by any other experimental technique. In the previous chapter, this ability was demonstrated for a structure that was not designed nor optimized to exhibit interference effects. With the characterization of the resonant devices in the chapter, these results have been extended to simple quantum devices in which the structure has been tailored to produce quasibound resonances. The semiclassical model developed in Chap. 2 and optimized in Chaps. 3 and 4 was shown to describe the resonant devices accurately, even in the second-derivative. It is imperative to emphasize that this excellent agreement between the data and the model would not have been possible without the analysis of the simpler structures. These results have achieved the thermally limited resolution of the technique at 7 K, 77 K, and 300 K, and have conclusively establish experimentally the proportionality between the calculated electron transmittance function and the experimental second-derivative BEES spectrum. In the next chapter, these fundamental results are applied to measure fluctuations in the thickness of a buried quantum well by monitoring the energy separation between the two quasibound states $E_{H1}$ and $E_{H2}$.

# Chapter 6

# Detection of single monolayer fluctuations in the thickness of a buried quantum well

Given that the electron-wavelength in a typical quantum device is on the order of nanometers, this new class of devices thus relies heavily on the ability to produce semiconductor structures in which the thickness (and composition) of the individual layers can be controlled with atomic precision. This constraint in turn creates a need for analysis techniques with very high spatial resolution that are also capable of detecting monolayer (ML) fluctuations in the thickness of the buried layers. Optical techniques such as photoreflection and photoluminesence can, under certain circumstances, detect the influence of 1 ML thickness changes in the electronic properties of a heterostructure device. However, these techniques lack the lateral spatial resolution needed to investigate fluctuations on the 10-100 nm length scale typical of terraces in semiconductors. Cross-sectional transmission electron microscopy provides high-resolution structural characterization, but no measurement of the corresponding effect on the electronic properties of the heterostructure. Conventional transport measurements such as current-voltage and capacitance-voltage spectroscopies provide only spatial averages of the quantities of interest, which can be dominated by small defect regions due to the nonlinear character of these measurements. Fortunately, BEES possesses both the spatial and energy resolution needed and is uniquely suited for performing this type of task.

In the previous chapters, the basis for utilizing BEES as an analysis tool for investigating electron-wave interference and confinement in quantum devices has been established.

However, the procedure to use the technique in a practical application has not been provided. In this chapter, the possibility of using BEES as a materials diagnostic tool for measuring small fluctuations ($\sim 1$ ML) in the thickness of a buried GaAs quantum well is explored. To detect these fluctuations, the energy separation between the two quasibound energy states (which depends strongly on the thickness of the well) of the DBRTD is monitored by measuring the electron transmittance function at various spatial locations. For the $\lambda_e/2$ structure (see Chap. 5), a change in the well thickness of 1 ML will correspond to approximately a 10 meV shift in the energy separation between $E_{H1}$ and $E_{H2}$. To detect such a small deviation amidst the noise in the small current signals, all of the knowledge gained in the previous work must be combined and utilized carefully and consistently.

## 6.1 Experimental Configuration

As discussed previously, the normal-incidence electron transmittance $T(E, \mathbf{k}_{\parallel} = 0)$, is an extremely important quantity for understanding the operation of electron-wave quantum devices. $T(E, \mathbf{k}_{\parallel} = 0)$ provides detailed information about the ballistic transport, and it is shown here that consequently it also gives valuable information about the quality and growth accuracy of the material used to construct the device. Henderson *et al.* [11] and Smith and Kogan [41] have shown theoretically that the BEES second-derivative spectrum $d^2I_c/dV_t^2$ provides an excellent measure of the normal-incidence electron transmittance. In the previous chapters this result was confirmed conclusively by using BEES to measure $T(E, \mathbf{k}_{\parallel} = 0)$ for half- and quarter-electron-wavelength semiconductor quantum interference filters under zero external bias [81]. Due to the resonant designs of these structures, both are extremely sensitive to the quality of the MBE growth. By utilizing the sensitivity of the transport properties to the quality of the MBE growth, these resonant structures can provide useful information about the material properties of the buried layers. In particular, the half-electron-wavelength filter will be used to study thickness fluctuations of the GaAs quantum well in the buried nanostructure. This electron-wave interference filter was designed to have two quasibound states: a tunneling resonance at $E = 50$ meV and an above-all-barriers resonance at $E = 200$ meV ($E$ is the kinetic energy in the GaAs output region of the device). In what follows, we show that the energy separation $\Delta E$ between these two quasibound states can be used to determine the thickness of the half-electron-wavelength active layer at various spatial locations. Due to spatial variations in the Schottky barrier height, it is imperative that $\Delta E$, and not simply the absolute position of the states $E$, be used. By measuring $\Delta E$ (instead of simply $E$) the spatial variation in the barrier height, which can be larger than the predicted shift in $\Delta E$, is removed from the measurement.

To illustrate how this measurement will be performed, Fig. 6.1 shows a schematic representation of the half-electron-wavelength filter used to measure the sub-surface thickness fluctuations. The potential barriers in the device are nominally 9 ML thick with an aluminium composition of $x = 0.2$. The active layer of the filter (labeled GaAs) has a nominal growth thickness $t = 22$ ML. Due to the statistical nature of MBE, the thickness of each layer may vary with position. Considering first only changes in the thickness of the active layer, three different BEES scenarios, corresponding to three different spatial locations of the STM tip, are also depicted in Fig. 6.1. From left to right, the transmittance (and thus the BEES current) at each location is determined by transport through a single active layer thickness $t = t_1$, a combination of coherent transport through two active layer thicknesses $t_1$ and $t_2$, and finally transport through a single active layer thickness $t_2 > t_1$. In each scenario depicted, the shape of the transmittance and the energy separation of the two quasibound states is altered due to the small sub-surface fluctuations. Since the BEES second-derivative spectrum provides exactly this information, these fluctuations should be detectable by performing BEES at various spatial locations and analyzing the resulting second-derivative spectra.

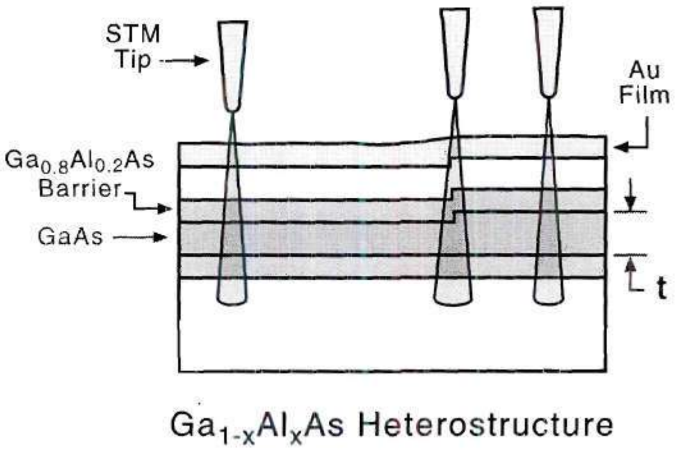

Figure 6.1: A schematic representation of the semiconductor half-electron-wavelength filter measured. Due to the resonant design of the structure, variations in the sub-surface topography (indicated by different STM tip positions) modify the shape of the BEES spectrum and allow the detection of changes in the buried layers.

## 6.2 Experimental Measurements

In Chap. 5, before attempting measurements on the resonant devices, it was important to investigate a best case scenario using simulations calculated under ideal conditions to determine whether or not the effects under consideration would be observable experimentally. For the detection of sub-surface thickness fluctuations, this type of analysis is especially important due to the extremely small magnitude of the expected changes in the transport properties. Furthermore, since the effect is caused by local variations in the buried nanostructure, lateral drift of the STM tip could render the fluctuations unobservable. If the tip were to drift across two different regions, the resulting spectra would be inhomogeneously broadened and would represent an average of the two regions. Thus it is important to investigate exactly what type and magnitude of changes in the transport properties are expected.

To determine whether or not the effect of these fluctuations will be detectable by BEES, the predicted ideal normal-incidence electron transmittance functions for various active layer thicknesses are shown in Fig. 6.2. Part (a) of the figure shows a band diagram for the device, where $\lambda_e$ is the electron-wavelength at energy $E_2$ and $E_F$ is the Fermi level. For energies below 0.28 eV (the onset of transmission into the GaAs $L$-minima), $E_1$ and $E_2$ are the only quasibound states. Shown in Fig. 6.2b are the calculated thermally-broadened transmittance functions for active layer thicknesses of $t = 21$, 22, and 23 ML (convolution with a Gaussian of width $3.5\,k_BT$ approximates the temperature-limited resolution of BEES [81]). The device was designed and nominally grown with $t = 22$ ML, thus these values represent a deviation of $\pm1$ ML which is achievable for high quality MBE growth. In this range of thicknesses, the location of $E_1$ remains nearly constant whereas $E_2$ shifts so that $\Delta E = \pm10$ meV for $\Delta t = \mp1$ ML. Given such a small $\Delta E$, and the fact that the second-derivative of a picoampere current is needed, whether or not the practical resolution of BEES is sufficient to resolve such subtle effects may seem questionable.

In order to establish that thickness variations in a buried heterostructure are measurable, BEES spectra were acquired during STM imaging by pausing the raster at regular spatial intervals ($\Delta x = 20$ nm). Shown in Fig. 6.3a is the STM image of an area in which BEES spectra were taken at each of the five labeled positions. The image is continuous and free of spatial distortions, indicating that lateral drift of the STM tip was negligible during BEES data acquisition (approximately 3 hours total). Below the image, in Fig. 6.3b, the second-derivative spectra for the high resolution data from locations 1, 4, and 5 are presented. The spectra (solid line) have been fit to the $T(E)$ model (dotted line) as described in Ref. [81]. For each spectrum, the thickness of the active layer in the model has been optimized to achieve the best fit to the data. The results show that spectra 1, 4, and 5 correspond to active layer thicknesses of $t = 21$, 22, and 23 ML, respectively. For all three spectra, the model reproduces all of the relevant features of the measurements, and the above-all-barriers quasibound state shifts in energy by $\sim 10$ meV per monolayer as predicted by the simulated electron transmittance in Fig. 6.2. Also note that the clear spectral changes from location 4 to location 5 show that the lateral spatial resolution of the

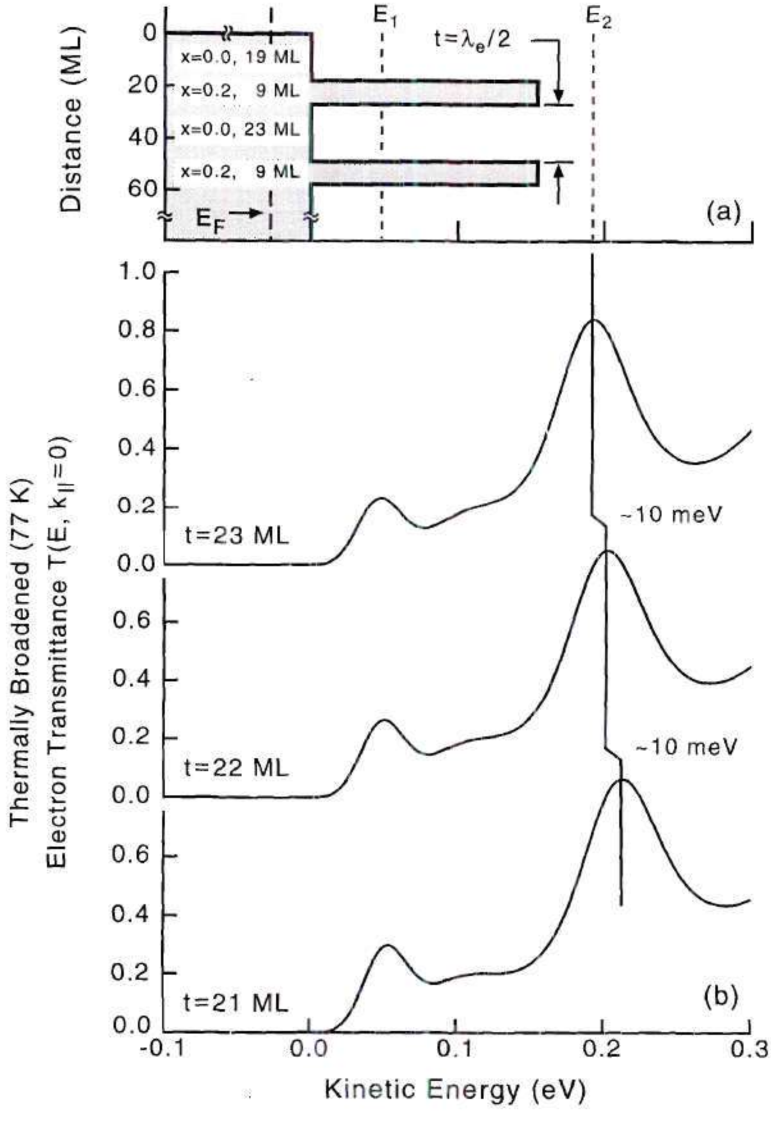

Figure 6.2: Effect of ±1 ML thickness fluctuation of buried GaAs quantum well on the corresponding normal-incidence electron transmittance function.(a) The band diagram for the half-electron-wavelength resonant device which has one tunneling resonance $E_1$, and one above-all-barriers resonance $E_2$. (b) The corresponding thermally broadened normal-incidence electron transmittance function $T(E, \mathbf{k}_{\parallel} = 0)$ calculated for three different active layer thicknesses ($t$ = 21, 22, and 23 ML). The curves show that the energy separation, $\Delta E = E_2 - E_1$, changes by approximately 10 meV for a ±1 ML fluctuation from the design value of 22 ML.

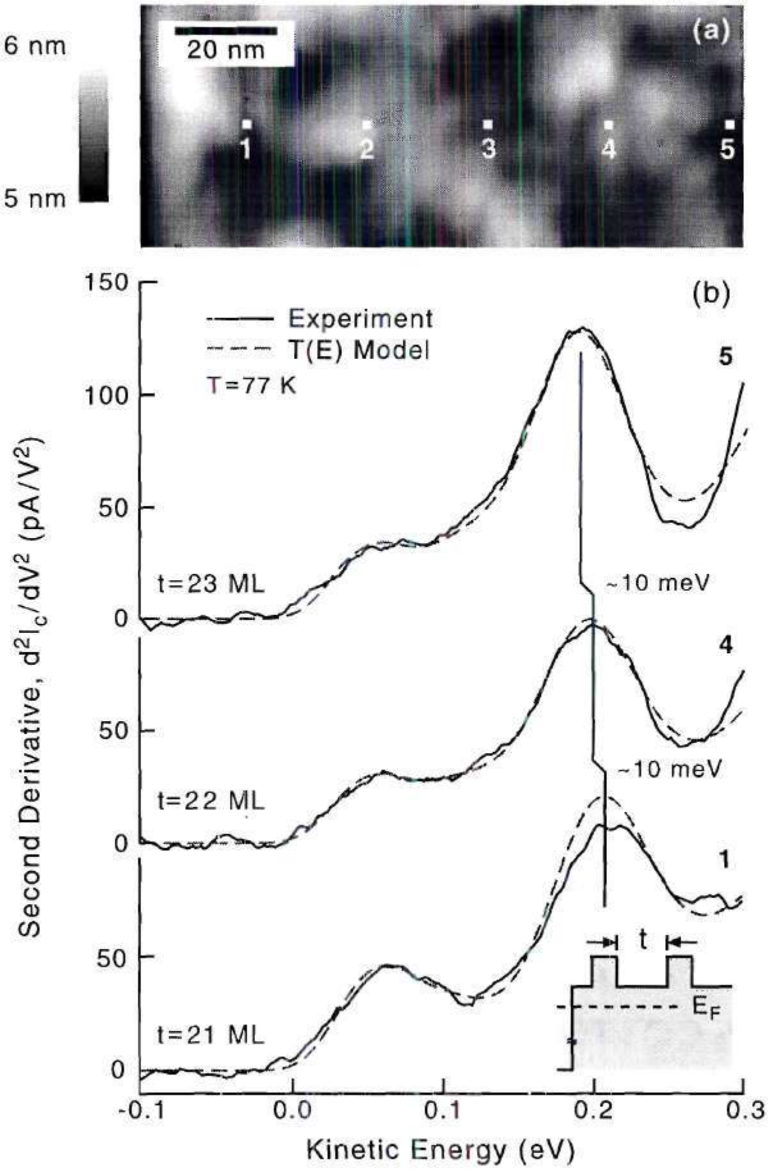

Figure 6.3: Effect of ±1 ML thickness fluctuation of buried GaAs quantum well on the experimental BEES second-derivative spectrum. (a) STM image of an area in which five BEES spectra were taken at 20 nm intervals during the image acquisition. The absence of spatial distortions in the image indicates that the STM tip did not drift in position during the acquisition of the spectra. (b) Second-derivatives of the experimental spectra and of the BEES $T(E)$ model spectra for data taken at locations 1, 4, and 5. To achieve an accurate fit, the thickness of the active layer $t$ has been optimized. The spectra reproduce the 10 meV shift predicted by the simulations and establish that BEES can resolve single monolayer changes in the sub-surface topography.

thickness fluctuations is better than 20 nm.

## 6.3 Discussion

In this chapter, high resolution BEES spectra have been used to detect fluctuations in the thickness of a buried GaAs quantum well. The quantum well measured forms the active layer of a half-electron-wavelength Fabry-Perot filter that has been designed to have two quasibound states. Simulations calculated under ideal circumstances predicted that $\pm 1$ ML variations in the thickness of the quantum well would produce $\mp 10$ meV variations in the energy separation between the two quasibound states. By performing BEES at several different spatial locations and by utilizing the relationship between the thickness of the active layer and the location (in energy) of the quasibound resonances, single monolayer variations in the thickness of the quantum well have been detected. Due to spatial variations in the SBH, it was found imperative that the energy separation $\Delta E$ be used as opposed to the absolute position of the energy peaks.

These results demonstrate a very practical application of the model and techniques developed in the previous chapters. These measurements show that the proportionality between the electron transmittance and the BEES second-derivative spectrum can be used to determine the local material properties and the quality of buried layers. The technique is unique due to its ability to probe sub-surface materials properties while simultaneously measuring the carrier transport properties. In addition, the information obtained provides information about local rather than average properties due to the nm-scale spatial resolution inherent to the technique. Measurements such as these can easily be extended to include systems other than ordinary semiconductor heterostructures. For example, spatially resolved information about carrier transport in self-assembled quantum dot's (SAD) could be investigated by obtaining BEES spectra at various locations on the buried structure. Regardless of the application, these measurements have shown the power and versatility of the technique for providing practical information about quantum devices. In some cases, as in this chapter and Chap. 5, the results could not have been obtained by any other measurement technique. They represent the ability to measure very fundamental quantities such as the normal-incidence transmittance, and demonstrate a way in which such fundamental quantities can be manipulated to provide useful information.

# Chapter 7

# Conclusions

## 7.1 Summary of Results

In this thesis, the power, versatility, and uniqueness of ballistic electron emission spectroscopy (BEES) as a tool for investigating ballistic carrier transport in quantum semiconductor devices have been explored and demonstrated. While obtaining these results, the fundamental limitations of the spectroscopic technique, which are imposed by thermal broadening, have been realized and demonstrated at 7 K, 77 K, and 300 K. The high-resolution measurements have achieved a signal-to-noise ratio that is superior to that of all other BEES systems described in the literature. With this capability, extensive use of the second-derivative spectra has been enabled for the first time. By utilizing the second-derivative spectrum, the electron transmittance function, a quantity fundamental to carrier transport in quantum devices, has been determined for two resonant devices under zero-bias. This represents the first direct measurement of $T(E)$ via a transport measurement. To demonstrate an application of these fundamental results, the sensitivity of the electron transmittance to changes in the underlying structure was used to detect single monolayer fluctuations in the thickness of a buried quantum well. Neither of these results would have been possible without the in-depth understanding gained by first investigating the simple single-interface and single-barrier structures.

The results of Chap. 2 and Chap. 3 for the single-interface measurements have been published in *Physical Review B* [71]. The detection of electron-wave interference effects in a single-barrier heterostructure presented in Chap. 4 and the measurements of the electron transmittance function of the quantum interference filters presented in Chap. 5 have been published in *Applied Physics Letters* [80,81]. The detection of single monolayer fluctuations in the buried quantum well discussed in Chap. 6 have been submitted to *Applied Physics Letters* for publication in early 1999. A summary of the main results for each chapter are as follows.

### 7.1.1 Semiclassical BEES Model

The semiclassical model commonly used to describe the BEES I–V spectrum was extended by incorporating two important dynamical effects: elastic scattering in metal base and at the M/S interface and the quantum transmittance arising from the impedance mismatch for electron-waves crossing the M/S interface. The elastic scattering was included via a scattering parameter $s$ which allows the momentum distribution incident on the M/S interface to be varied from planar tunneling distribution to a completely isotropic in angle. The quantum transmittance was calculated using wave mechanics and was included for all angles of incidence.

In addition to the extensions above, the model was enhanced by including all of the relevant band minima in the semiconductor collector. Previously, only the minima that project onto the Brillouin zone center of the interface plane were included in the model. The validity of using a simple single-band time-independent effective mass approach was discussed as well as its limitations. The validity of the approximations made and the regime where the model is expected to be accurate were assessed. The model developed is capable of providing a more complete description of the electron transport in BEES.

### 7.1.2 Single-Interface Measurements

High-resolution low-noise BEES measurements were taken at low-temperature on three different material systems: Au/Si(100), Au/Si(111), and Au/GaAs(100). These measurements were used to test and optimize the extended BEES model developed in Chap. 2. The measurements taken on the Au/Si(100) and Au/Si(111) structures were used primarily to determine the optimum value of the scattering parameter $s$ which serves as an indicator of the amount of elastic scattering the electrons experience before being collected by the semiconductor. The results of these studies showed that a nearly isotropic in angle momentum distribution is needed to accurately describe the shape and magnitude of the spectra. The main cause of the distribution broadening is believed to be multiple reflections of the electron-waves in the thin metal film. The measurements taken on the Au/GaAs(100) structure were used primarily to investigate whether or not the effect of the single-interface quantum transmittance could be detected by the BEES spectrum. By focusing on the near-threshold region, spectra taken at 7 K showed conclusively that the effect modifies the shape of the BEES spectrum. Similar results were found for spectra taken on the Au/Si structures at 77 K. All of the spectra were accurately described by the extended BEES model.

The range of validity for the various models commonly used to describe the carrier transport was assessed. Of the four models [$T(E)$, $T = 1$, $P = 2.0$, and $P = 5/2$], the model which includes the full quantum transmittance for all energies and angles, the $T(E)$ model, was found to provide the most accurate and stable description of the data. The other models described the data well just above threshold, but gradually became worse as the size of the fit range (amount of data used) was increased. The best description was achieved for the Au/GaAs interface system which has the simplest band structure of all the structures. The effect of including an energy-dependent effective mass for the Au/Si structures was found to produce insignificant changes in the ability of the model to describe the experimental data.

### 7.1.3 Multiple-Interface Measurements

High-resolution low-noise BEES measurements were taken at 7 K and 77 K on a $Ga_{0.8}Al_{0.2}As$ single-barrier structure. To prevent electrons with an energy less than the conduction band offset of $Ga_{0.8}Al_{0.2}As$ barrier from tunneling through, the thickness of the potential barrier was designed to be thick (20 nm). By comparing the SBH determined for this structure with the SBH determined from a separate GaAs sample, the conduction band offset of the $Ga_{0.8}Al_{0.2}As$ material was determined at both 7 K and 77 K and was found to be in good agreement with accepted values. By utilizing the second-derivative spectrum, the presence of weak quasibound resonances, caused by the small, finite thickness of the input region, were revealed. It is important to note that this structure was not designed nor optimized to show such effects. The measurements taken at 77 K showed heavily broadened features while the measurements taken at 7 K showed two relatively sharp features which correspond the the location of the quasibound states.

At both temperatures, in order to accurately describe the second-derivative spectra, a model which includes the transmission/reflection from all of the interfaces in the device was necessary. A more simple model which treats the structures as a single interface of $Au/Ga_{0.8}Al_{0.2}As$ was found to described only the average shape of the second-derivative spectrum and could not reproduce the distinct features caused by the electron-wave interference. For the complete model, the value of the input region (which can vary due to sample preparation) had to be optimized in order to achieve an accurate description of the data. Fluctuations in the value of this third fit parameter were found to be 2-3 monolayers.

### 7.1.4 Resonant Device Measurements

High-resolution low-noise BEES measurements were taken at 7 K, 77 K, and 300 K on two electron-wave quantum-interference filters to investigate experimentally the relationship between the electron transmittance function and the BEES second-derivative spectrum. The structures included both a half- and quarter-electron-wavelength (using optics terminology) Fabry-Perot type filter that have been designed specifically for BEES testing. In particular, the devices were designed to exhibit complementary behavior (constructive/destructive interference at the design energy) and, for clarity, were designed such that all of their quasibound energy states lie below the L-minima in GaAs.

Second-derivative spectra derived from current-versus-voltage measurements clearly show both tunneling and above-barrier quasibound energy states. Although significantly broadened, all resonant states were also evident in room temperature measurements, which implies an electron coherence length at 300 K much greater than the half-electron-wavelength device length. At 7 K, an almost exact reproduction of the the electron transmittance function for the quarter-electron-wavelength device was obtained. Spectra obtained at all temperatures on both types of devices were accurately described by the extended $T(E)$ model. The excellent agreement between the model and the data could only be achieved by optimizing the width of the input region as was discovered in the single-barrier structure. In the resonant structures, the existence of a finite input region lead to secondary features in the second-derivative spectrum that altered the shape of the designed resonances. By incorporating this effect into the model, all of the relevant features of the transmittance were reproduced by the model. In all cases, the spectra accurately reproduce the transmittance functions of the designed structures, attaining nearly the temperature-limited resolution at 7 K, 77 K, and 300 K. The results demonstrated the unique power of the technique for probing carrier transport in quantum devices and also conclusively determined experimentally the exact relationship between the transmittance function and the BEES second-derivative spectrum.

### 7.1.5 Application to Materials Diagnostics

High resolution BEES spectra from the half-electron-wavelength device were used to detect small fluctuations in the thickness of a buried GaAs quantum well. By performing BEES at several different spatial locations and by utilizing the relationship between the thickness of the active layer and the location (in energy) of the quasibound resonances, single monolayer variations in the thickness of the quantum well have been detected. Due to spatial variations in the SBH, it was imperative that the energy separation $\Delta E$ be used as opposed to the absolute position of the energy peaks. Using this approach, single monolayer fluctuations in the thickness of the buried layer have been detected. Clear spectral changes from location to location showed that the lateral spatial resolution of the thickness fluctuations is better than 20 nm. To achieve such resolution, all of the knowledge gained in the previous chapters on simpler structures was utilized. The measurements represent the culmination of the systematic approach used for investigating these structures. The results obtained show that BEES has the ability to measure very fundamental quantities such as the normal-incidence transmittance, and demonstrated a way in which such fundamental quantities can be manipulated to provide useful information.

## 7.2 Future Research

The research in this thesis has provided an in-depth investigation of a series of progressively more complex quantum semiconductor structures which could serve as the basis for a number of future projects. The most obvious extension would be to utilize the three terminal aspect to apply a series of biases across the buried heterostructure. As alluded to earlier, by measuring the transmittance as a function of both energy and device bias, a complete characterization of the device is possible. Accommodating the device bias in the model would involve replacing the exponentials (associated with constant potentials) with Airy functions (associated with linear potentials) in the chain matrix calculation of $T(E_x, E_t)$. Once biasing of a simple structure is well understood, measurements on much more complex structures such as the newly developed quantum cascade and intra-band lasers could be performed and compared with other types of measurements and with calculations. For example, by measuring the transmittance function at the appropriate bias, the location of the quasibound states that are responsible for lasing could be determined and compared with the corresponding emission spectra for the structure. It may also be possible to use the injected current as a source for generating light emission if the injected current can be made sufficiently large. Detecting very small light emission signals should be feasible since the system is already completely isolated from external light and operates at low-temperature where detector performance is optimum. In addition to the lasing structures, BEES could also be used to investigate the transport properties and quasibound states in quantum well infrared photodetectors (QWIP's). In these types of structures, BEES could provide invaluable information about the transport that cannot be obtained by any other means.

As mentioned in Chap. 6, BEES measurements could be used to investigate carrier transport in structures such as semiconductor self-assembled quantum dots (SAD) [44]. In SAD's, carriers are confined in all three dimensions leading to a quasi-zero-dimensional structure. The nature of this confinement, which varies laterally across the quantum dot, could be investigated by obtaining BEES spectra at various locations on and near the dot. SAD's such as InAs can be grown within a GaAs matrix leading to a base-line structure that has a well-understood and well-described BEES spectra as shown in Chap. 3. One structure in particular that would be very interesting to measure involves sandwiching the SAD's between two $\mathrm{Ga}_{1-x}\mathrm{Al}_x\mathrm{As}$ barriers (all grown in GaAs) to form a $\mathrm{GaAs}/\mathrm{Ga}_{1-x}\mathrm{Al}_x\mathrm{As}/\mathrm{SAD}/\mathrm{Ga}_{1-x}\mathrm{Al}_x\mathrm{As}/\mathrm{GaAs}$ type structure. BEES spectra taken at a location with no quantum dot present below the STM tip would behave similar to the single-barrier structure in Chap. 4. Spectra taken with the STM tip located above a dot would produce spectra similar to those measured on the DBRTD structure in Chap. 5. Measurements on similarly confined structures such as quantum wires and 2-D electron gasses could also be performed.

Although all of the structures in this work have utilized the injection of electrons into n-type material, BEES can also be used to perform ballistic hole spectroscopy on p-type materials and heterostructures. Preliminary simulations of the transmittance in p-type heterostructures similar to those measured in this work show that, due to the increased effective mass of the holes, even small fluctuations in the buried layers will produce remarkably large variations in the transmittance. This type of measurement would aid in the understanding of the complicated semiconductor valence band. Unfortunately, this area of the technique has remained largely unexplored because the measurements must be performed at low temperature due to small Schottky barrier heights associated with p-type semiconductors. Although the BEES current will be much larger in p-type devices due to the increased effective mass, the increased thermal noise and the reduction in the number of carriers at higher voltage due to the asymmetry of the vacuum barrier have kept measurements on this type of structure to a minimum.

In addition to measuring semiconductor heterostructures, BEES can also be used to probe carrier transport through their metallic counterpart, metal multilayers. These structures are fabricated by replacing the thin gold layer with multiple layers of differing metals. Currently, the most studied structures, known as magnetic multilayers, involve alternating layers of magnetic and non-magnetic materials. This type of structure is currently being developed for use in high-speed, ultra-large capacity hard disk read/write heads due to their ability to sense extremely small magnetic changes. In these structures, for particular thicknesses of the non-magnetic material, the magnetic layers will become coupled such that their magnetic spins point in opposite directions. By applying a small magnetic field, the spins can be aligned. Electrons traveling through the multilayer with anti-aligned spins experience a larger resistance than if the magnetic spins were aligned. By monitoring the BEES current as a function of applied magnetic field, the magneto-transport in these structures can be measured with very high spatial and energy resolution. By imaging the BEES current as a function of position, an image of the underlying magnetic structure may be possible. By depositing small islands of magnetic material within a gold film, it may be possible to investigate magnetism on the nm length-scale.

# Bibliography

[1] G. E. Moore, "Progress in digital integrated electronics," *IEEE IEDM Tech. Dig.*, pp. 11–13, 1975.

[2] F. Capasso, ed., *Physics of Quantum Electron Devices*, vol. 28 of *Series in Electronics and Photonics*. Berlin: Springer-Verlag, 1989.

[3] G. N. Henderson, T. K. Gaylord, and E. N. Glytsis, "Ballistic electron transport in semiconductor heterostructures and its analogies in electromagnetic propagation in general dielectrics," *Proc. IEEE*, vol. 79, pp. 1643–1659, Nov. 1991.

[4] R. Tsu and L. Esaki, "Tunneling in a finite superlattice," *Appl. Phys. Lett.*, vol. 22, pp. 562–564, June 1973.

[5] S. Sen, F. Capasso, A. C. Gossard, R. A. Spah, A. L. Hutchinson, and S. N. G. Chu, "Observation of resonant tunneling through a compositionally graded parabolic quantum well," *Appl. Phys. Lett.*, vol. 51, pp. 1428–1430, Nov. 1987.

[6] S. Y. Chou, J. S. Harris, and R. F. W. Pease, "Lateral resonant tunneling field-effect transistor," *Appl. Phys. Lett.*, vol. 52, pp. 1982–1984, June 1988.

[7] M. Heiblum, M. V. Fischetti, W. P. Dumke, D. J. Frank, I. M. Anderson, C. M. Knoedler, and L. Osterling, "Electron interference effects in quantum wells: observation of bound and resonant states," *Phys. Rev. Lett.*, vol. 58, pp. 816–19, Feb. 1987.

[8] R. C. Potter and A. A. Lakhani, "Combining resonant tunneling diodes for signal processing and multilevel logic," *Appl. Phys. Lett.*, vol. 52, pp. 1684–1685, May 1988.

[9] J. R. Hayes, P. England, and J. P. Harbison, "Quantum interference effects in GaAs/GaAlAs bulk potential barriers," *Appl. Phys. Lett.*, vol. 52, pp. 1578–1580, May 1988.

[10] F. Beltram, F. Capasso, A. L. Hutchinson, and R. J. Malik, "Injection in a continuum miniband: Observation of negative transconductance in a superlattice-base transistor," *Appl. Phys. Lett.*, vol. 55, pp. 1534–1536, Oct. 1989.

[11] G. N. Henderson, T. K. Gaylord, E. N. Glytsis, P. N. First, and W. J. Kaiser, "Ballistic electron emission testing of semiconductor heterostructures," *Solid State Comm.*, vol. 80, pp. 591–596, Nov. 1991.

[12] W. J. Kaiser and L. D. Bell, "Direct investigation of subsurface interface electronic structure by ballistic-electron-emission microscopy," *Phys. Rev. Lett.*, vol. 60, pp. 1406–1409, Apr. 1988.

[13] L. D. Bell and W. J. Kaiser, "Ballistic-electron-emission microscopy: A nanometer-scale probe of interfaces and carrier transport," *Annu. Rev. Mater. Sci.*, vol. 26, pp. 189–222, 1996.

[14] L. D. Bell and W. J. Kaiser, "Observation of interface band structure by ballistic-electron-emission microscopy," *Phys. Rev. Lett.*, vol. 61, pp. 2368–2371, Nov. 1988.

[15] H. Rohrer and G. Binnig, "Surface studies by scanning tunneling microscopy," *Physical Review Letters*, vol. 49, pp. 57–60, 1982.

[16] A. E. Fowell, R. H. Williams, B. E. Richardson, A. A. Cafolla, D. I. Westwood, and Woolf, "Ballistic electron emission microscopy studies of Au-CdTe and Au-GaAs interfaces and band structure," *J. Vac. Sci. Tech. B*, vol. 9, pp. 581–584, Mar.-Apr. 1991.

[17] H. Palm, M. Arbes, and M. Schulz, "Fluctuations of the Au-Si(100) Schottky barrier height," *Phys. Rev. Lett.*, vol. 71, pp. 2224–2227, Oct. 1993.

[18] A. A. Talin, R. S. Williams, B. A. Morgan, K. M. Ring, and K. L. Kavanagh, "Nanometer-resolved spatial variations in the Schottky barrier height of a Au/n-type GaAs diode," *Phys. Rev. B*, vol. 49, pp. 16474–16479, June 1994.

[19] B. A. Morgan, K. M. Ring, K. L. Kavanagh, A. A. Talin, R. S. Williams, T. Yasuda, T. Yasui, and Y. Segawa, "Au/ZnSe contacts characterized by ballistic electron emission microscopy," *J. Appl. Phys.*, vol. 79, pp. 1532–1535, Feb. 1996.

[20] B. A. Morgan, K. M. Ring, K. L. Kavanagh, A. A. Talin, R. S. Williams, T. Yasuda, T. Yasui, and Y. Segawa, "Role of interface microstructure in rectifying metal/semiconductor contacts: Ballistic electron emission observations correlated to microstructure," *J. Vac. Sci. Tech. B*, vol. 14, pp. 1238–1242, Mar.-Apr. 1996.

[21] M. H. Hecht, L. D. Bell, W. J. Kaiser, and L. C. Davis, "Ballistic-hole spectroscopy of interfaces," *Phys. Rev. B*, vol. 42, pp. 7663–7666, Oct. 1990.

[22] J. J. O'Shea, E. G. Brazel, S. Bhargava, M. A. Chin, and V. Narayanamurti, "Ballistic-electron emission spectroscopy of $\mathrm{Al}_x\mathrm{Ga}_{1-x}\mathrm{As}$/GaAs heterostructures: conduction-band offsets, transport mechanisms, and band-structure effects," *Phys. Rev. B*, vol. 656, pp. 2026–2035, July 1997.

[23] R. Ludeke, M. Prietsch, and A. Samsavar, "Ballistic electron emission spectroscopy of metals on GaP(110)," *J. Vac. Sci. Tech. B*, vol. 9, pp. 2342–2348, July-Aug. 1991.

[24] R. Ludeke and M. Prietsch, "Ballistic electron emission spectroscopy of noble metal-GaP(110) interfaces," *J. Vac. Sci. Tech. A*, vol. 9, pp. 885–890, May-June 1991.

[25] R. Ludeke and A. Bauer, "Hot electron scattering processes in metal films and at metal-semiconductor interfaces," *Phys. Rev. Lett.*, vol. 71, pp. 1760–1763, Sept. 1993.

[26] R. Ludeke, "Density of states and hot electron effects in ballistic electron emission spectroscopy," *J. Vac. Sci. Tech. A*, vol. 11, pp. 786–791, July-Aug. 1993.

[27] R. Ludeke and A. Bauer, "Electrical transport properties of hot electrons at metal and insulator and semiconductor interfaces," *J. Vac. Sci. Tech. A*, vol. 13, pp. 614–622, May-June 1995.

[28] H. J. Wen, R. Ludeke, D. M. Newns, S. H. Lo, and E. Cartier, "Atomic-scale studies of electron transport through MOS structures," *Appl. Surf. Sci.*, vol. 123-1, pp. 418–428, Jan. 1998.

[29] H. J. Wen and R. Ludeke, "Localized degradation studies of ultrathin gate oxides," *J. of Vac. Sci. Tech. A*, vol. 16, pp. 1735–1740, May-June 1998.

[30] P. Niedermann, L. Quattropani, K. Solt, A. D. Kent, and O. Fischer, "Ballistic electron emission microscopy study of PtSi-n-Si(100) Schottky diodes," *J. Vac. Sci. Tech. B*, vol. 10, pp. 580–585, Mar.-Apr. 1992.

[31] P. Niedermann, L. Quattropani, K. Solt, I. Maggio-Aprile, and O. Fischer, "Hot-carrier scattering in a metal: A ballistic-electron-emission microscopy investigation on PtSi," *Phys. Rev. B*, vol. 48, pp. 8833–8839, Sept. 1993.

[32] L. Tsau, T. C. Kuo, and K. L. Wang, "Ballistic-electron-emission microscopy of (100)CoGa/n-type GaAs interfaces grown by molecular beam epitaxy," *Appl. Phys. Lett.*, vol. 63, pp. 1062–1064, Aug. 1993.

[33] R. Coratger, F. Ajustron, J. Beauvillain, I. M. Dharmadasa, C. J. Blomfield, K. A. Prior, J. Simpson, and B. C. Cavenett, "Au/n-ZnSe contacts studied with use of ballistic-electron-emission microscopy," *Phys. Rev. B*, vol. 51, pp. 2357–2362, Jan. 1995.

[34] M. Ke, C. C. Matthai, A. Pavlov, and R. Laiho, "Schottky barrier height at the Au/porous silicon interface," *Appl. Surf. Sci.*, vol. 123-1, pp. 454–457, Jan. 1998.

[35] R. M. Mehra, V. Agarwal, and P. C. Mathur, "Development and characterization of porous silicon (a review)," *Diff. Defects Data B*, vol. 55, pp. 71–76, 1997.

[36] A. Davies and H. G. Craighead, "Ballistic-electron-emission microscopy characteristics of reverse-biased Schottky diodes," *Appl. Phys. Lett.*, vol. 64, pp. 2833–2835, May 1994.

[37] S. M. Sze, *Physics of Semiconductor Devices*. New York: John Wiley and Sons, 1981.

[38] S. Adachi, "GaAs, AlAs, and $Al_xGa_{1-x}As$: Materials parameters for use in research and device applications," *J. Appl. Phys.*, vol. 58, pp. R1–R29, Aug. 1985.

[39] L. D. Bell, R. P. Smith, B. T. McDermott, E. R. Gertner, R. Pittman, R. L. Pierson, and G. J. Sullivan, "Ballistic-electron-emission microscopy and spectroscopy of metal/GaN interfaces," *Appl. Phys. Lett.*, vol. 72, pp. 1590–1592, Mar. 1998.

[40] H. J. Im, B. Kaczer, J. P. Pelz, and W. J. Choyke, "Ballistic electron emission microscopy study of Schottky contacts on 6H- and 4H-SiC," *Appl. Phys. Lett.*, vol. 72, pp. 839–841, Feb. 1998.

[41] D. L. Smith and S. M. Kogan, "Theory of ballistic-electron-emission microscopy of buried semiconductor heterostructures," *Phys. Rev. B*, vol. 54, pp. 10354–10357, Oct. 1996.

[42] S. Bhargava, H. R. Blank, V. Narayanamurti, and H. Kroemer, "Fermi-level pinning position at the Au-InAs interface determined using ballistic electron emission microscopy," *Appl. Phys. Lett.*, vol. 70, pp. 759–761, Feb. 1997.

[43] J. J. O'Shea, C. M. Reaves, S. P. DenBaars, M. A. Chin, and V. Narayanamurti, "Conduction band offsets in ordered-GaInP/GaAs heterostructures studied by ballistic-electron-emission microscopy," *Appl. Phys. Lett.*, vol. 69, pp. 3022–3024, Nov. 1996.

[44] M. E. Rubin, G. Medeiros-Ribeiro, J. J. O'Shea, M. A. Chin, E. Y. Lee, P. M. Petroff, and V. Narayanamurti, "Imaging and spectroscopy of single InAs self-assembled quantum dots using ballistic electron emission microscopy," *Phys. Rev. Lett.*, vol. 77, pp. 5268–5271, Dec. 1996.

[45] M. E. Rubin, H. R. Blank, M. A. Chin, H. Kroemer, and V. Narayanamurti, "Local conduction band offset of GaSb self assembled quantum dots on GaAs," *Appl. Phys. Lett.*, vol. 70, pp. 1590–1592, Mar. 1997.

[46] M. Ke and D. I. Westwood, "BEEM study of electron tunnelling across single AlAs barriers," *Appl. Surf. Sci.*, vol. 123-1, pp. 255–260, Jan. 1998.

[47] D. I. Westwood, M. L. Ke, F. Lelarge, F. Laruelle, and B. Etienne, "Characterisation of buried lateral period superlattices by ballistic electron emission microscopy," *Surface Sci.*, vol. 352-3, pp. 802–806, May 1996.

[48] C. Eder, A. J. Smoliner, G. Strasser, and E. Gornik, "Ballistic electron emission microscopy in liquid helium using low dimensional collector electrodes," *Appl. Phys. Lett.*, vol. 69, pp. 1725–1727, Sept. 1996.

[49] C. Eder, J. Smoliner, G. Strasser, and E. Gornik, "BEEM studies on GaAsAl$_x$Ga$_{1-x}$As quantum wire structures," *Superlattices Microstructures*, vol. 20, pp. 357–361, 1996.

[50] T. Sajoto, J. J. O'Shea, S. Bhargava, D. Leonard, M. A. Chin, and V. Narayanamurti, "Direct observation of quasi-bound states and band-structure effects in a double barrier resonant tunneling structure using ballistic electron emission," *Phys. Rev. Lett.*, vol. 74, pp. 3427–3430, Apr. 1995.

[51] J. G. Simmons, "Generalized formula for the electric tunnel effect between similar electrodes separated by a thin insulating film," *J. Appl. Phys*, vol. 34, pp. 1793–1803, June 1963.

[52] M. Prietsch, *Ballistic-electron emission microscopy (BEEM) applied to the electronic structure of metal/semiconductor interfaces.* Habilitationsschrift, Institut fur Experimentalphysik, Freie Universitat Berlin, 1992.

[53] M. Prietsch and R. Ludeke, "Ballistic-electron-emission microscopy and spectroscopy of GaP(110)-metal interfaces," *Phys. Rev. Lett.*, vol. 66, pp. 2511–2514, May 1991.

[54] E. Y. Lee and L. J. Schowalter, "Phonon scattering and quantum mechanical reflection at the Schottky barrier," *J. Appl. Phys.*, vol. 70, pp. 2156–2162, Aug. 1991.

[55] F. J. Garcia-Vidal, P. L. de Andres, and F. Flores, "Elastic scattering and the lateral resolution of ballistic electron emission microscopy: Focusing effects on the Au/Si interface," *Phys. Rev. Lett.*, vol. 76, pp. 807–810, Jan. 1996.

[56] R. M. Kolbas, Y. C. Lo, and J. H. Lee, "Laser properties and carrier collection in ultrathin quantum-well heterostructures," *IEEE J. Quan. Elec.*, vol. 26, pp. 25–31, Jan. 1990.

[57] A. Fernandez, H. D. Hallen, T. Huang, R. A. Buhrman, and J. Silcox, "Elastic scattering in ballistic-electron-emission-microscopy studies of the epitaxial $\mathrm{NiSi_2}$/Si(111) interface," *Phys. Rev. B*, vol. 44, pp. 3428–3431, Aug. 1991.

[58] L. J. Schowalter and E. Y. Lee, "Role of elastic scattering in ballistic-electron-emission microscopy of Au/Si(001) and Au/Si(111) interfaces," *Phys. Rev. B*, vol. 43, pp. 9308–9311, Apr. 1991.

[59] M. Altarelli, "Band structure, impurities and excitons in superlattices," in *Heterojunctions and semiconductor superlattices* (G. Allan, G. Bastard, N. Boccara, M. Lannoo, and M. Voos, eds.), (Berlin), pp. 12–37, Proc. of the Winter School, Springer-Verlag, Mar. 1985.

[60] J. M. Luttinger and W. Kohn, "Motion of electrons and holes in perturbed periodic fields," *Phys. Rev. B*, vol. 97, pp. 869–883, Feb. 1955.

[61] S.-L. Chuang, "Theory of hole refractions from heterojunctions," *Phys. Rev. B*, vol. 40, pp. 10379–10390, Nov. 1989.

[62] P. L. D. Andres, K. Reuter, F. J. Garcia-Vidal, D. Sestovic, and F. Flores, "A theoretical analysis of ballistic electron emission microscopy: K-space distributions and spectroscopy," *Appl. Surf. Sci.*, vol. 123-1, pp. 199–206, Jan. 1998.

[63] P. N. First, J. A. Bonetti, D. K. Guthrie, L. E. Harrell, and S. S. P. Parkin, "Ballistic electron emission spectroscopy of magnetic multilayers," *J. Appl. Phys.*, vol. 81, p. 5533, Apr. 1997.

[64] P. Armour, T. H. Shen, M. L. Ke, and R. Grey, "Hot-electron transmission through metal-metal interfaces: A study of Au/Fe/Au trilayers on gaas substrates," *Appl. Surf. Sci.*, vol. 123-1, pp. 412–417, Jan. 1998.

[65] T. Kinno, K. Tanaka, and K. Mizushima, "Ballistic-electron-emission spectroscopy on an Fe/Au/Fe multilayer," *Phys. Rev. B*, vol. 56, pp. R4391–R4393, Aug. 1997.

[66] G. N. Henderson, P. N. First, T. K. Gaylord, E. N. Glytsis, B. J. Rice, P. L. Dantzscher, D. K. Guthrie, L. E. Harrell, and J. S. Cave, "Low-temperature scanning tunneling microscope for ballistic electron emission microscopy and spectroscopy," *Rev. Sci. Instrum.*, vol. 66, pp. 91–96, Jan. 1995.

[67] A. A. Talin, R. S. Williams, K. L. Kavanagh, C. W. Tu, D. C. Houghton, and R. T. Tung, "BEEM investigation of oxide and sulfide passivated GaAs," in *Semiconductor Heterostructures for Photonic and Electronic Applications Symposium*, pp. 653–658, 1993.

[68] G. N. Henderson, P. N. First, T. K. Gaylord, and E. N. Glytsis, "Quantum transmittance from low-temperature ballistic electron emission spectroscopy of Au/Si(100) Schottky interfaces," *Phys. Rev. Lett.*, vol. 71, pp. 2999–3002, Nov. 1993.

[69] E. Y. Lee, B. R. Turner, L. J. Schowalter, and J. R. Jimenez, "Diffusive and inelastic scattering in ballistic-electron-emission spectroscopy and ballistic-electron-emission microscopy," *J. Vac. Sci. Tech. B*, vol. 11, pp. 1579–1583, July-Aug. 1993.

[70] L. D. Bell, "Evidence of momentum conservation at a nonepitaxial metal/semiconductor interface using ballistic electron emission microscopy," *Phys. Rev. Lett.*, vol. 77, pp. 3893–3896, Oct. 1996.

[71] D. K. Guthrie, L. E. Harrell, G. N. Henderson, P. N. First, T. K. Gaylord, E. N. Glytsis, and R. E. Leibenguth, "Ballistic electron emission spectroscopy of Au/Si and Au/GaAs interfaces: low-temperature measurements and ballistic models," *Phys. Rev. B*, vol. 54, pp. 16972–16982, Dec. 1996.

[72] J. Singh, *Physics of semiconductors and their heterostructures.* McGraw-Hill series on electrical and computer engineering, New York: McGraw-Hill, 1993.

[73] J. J. O'Shea, T. Sajoto, S. Bhargava, D. Leonard, M. A. Chin, and V. Narayanamurti, "Measurement of heterojunction band offsets using ballistic electron emission," *J. Vac. Sci. Tech. B*, vol. 12, pp. 2625–2628, July-Aug. 1994.

[74] A. A. Talin, D. A. A. Ohlberg, R. S. Williams, P. Sullivan, I. Koutselas, B. Williams, and K. L. Kavanagh, "Time dependent ballistic electron emission microscopy studies of a Au/(100) GaAs interface with a native oxide diffusion barrier," *Appl. Phys. Lett.*, vol. 62, pp. 2965–2967, June 1993.

[75] W. H. Press, S. A. Teukolsky, W. T. Betterling, and B. P. Flannery, *Numerical Recipes in Fortran.* Mass.: Cambridge University Press, 2nd ed., 1992.

[76] B. F. Levine, "Quantum-well infrared photodetectors," *J. Appl. Phys.*, vol. 74, pp. R1–R76, Oct. 1993.

[77] L. Esaki and R. Tsu, "Superlattice and negative differential conductivity in semiconductors," *IBM J. Res. Develop.*, vol. 14, pp. 61–65, Jan. 1970.

[78] R. F. Kazarinov and R. A. Suris, "Possibility of the amplification of electromagnetic waves in a semiconductor with a superlattice," *Soviet Physics - Semicon.*, vol. 5, pp. 707–709, Oct. 1971.

[79] F. Capasso, J. Faist, D. L. Sivco, C. Sirtori, A. L. Hutchinson, and S. N. G. Chu, "Quantum cascade laser: A unipolar intersubband semiconductor laser," in *14th IEEE International Semiconductor Laser Conference*, pp. 71–72, 1994.

[80] D. K. Guthrie, P. N. First, T. K. Gaylord, E. N. Glytsis, and R. E. Leibenguth, "Electron-wave interference effects in a $Ga_{1-x}Al_xAs$ single-barrier structure measured by ballistic electron emission spectroscopy," *Appl. Phys. Lett.*, vol. 71, pp. 2292–2294, Oct. 1997.

[81] D. K. Guthrie, P. N. First, T. K. Gaylord, E. N. Glytsis, and R. E. Leibenguth, "Measurement of the zero-bias electron transmittance as a function of energy for half- and quarter-electron-wavelength semiconductor quantum-interference filters," *Appl. Phys. Lett.*, vol. 72, pp. 374–376, Jan. 1998.

# Vita

Dan Guthrie was born on January 20, 1971 in Kettering, Ohio to Jim and Phyllis Guthrie. After completing high school as salutatorian, he enrolled at the Georgia Institute of Technology in the fall of 1989, where he earned the Bachelor of Science in Electrical Engineering with highest honor. For his graduate work, he remained at Georgia Tech and received the Master of Science in 1998. Mr. Guthrie is a member of the Eta Kappa Nu, Sigma Xi, American Physical Society.

Permanent Address: 2984 Maple Walk Ct
Lawrenceville, GA 30044

This thesis was typeset with LaTeX $2_\varepsilon$[1] by the author.

---

[1] LaTeX $2_\varepsilon$ is an extension of LaTeX. LaTeX is a collection of macros for TeX. TeX is a trademark of the American Mathematical Society. The macros used in formatting this thesis were written by Dinesh Das, Department of Computer Sciences, The University of Texas at Austin.